Die approbierte Originalversion dieser Diplom-/Masterarbeit ist in der Hauptbibliothek der Technischen Universität Wien aufgestellt und zugänglich.
http://www.ub.tuwien.ac.at

The approved original version of this diploma or master thesis is available at the main library of the Vienna University of Technology.
http://www.ub.tuwien.ac.at/eng

DIPLOMARBEIT

Evaluating a Novel Approach for Fiber Analysis in Forensic Applications

ausgeführt am

Institut für Chemische Technologien und Analytik
der Technischen Universität Wien

Institute of Chemical Technologies and Analytics
Vienna University of Technology

unter der Anleitung von
Ao.Univ.Prof. Mag.rer.nat. Dr.rer.nat. Johann Lohninger
durch

Elisabeth Wetzer
Hütteldorferstraße 163/30
A-1140 Wien

am
23. Jänner 2017

Unterschrift des Betreuers

Unterschrift der Diplomandin

Abstract

Das Ziel dieser Studie besteht darin, die Realisierbarkeit eines neuen Ansatzes zur automatisierten Fasernanalyse mittels Raman-Spektroskopie zu evaluieren. Um eine automatisch gesteuerte Kollektion von Raman-Spektren zu ermöglichen, beschäftigt sich der erste Teil dieser Arbeit mit Bildverarbeitung. Das Ziel hierbei ist es, durch geschickte Anwendung von morphologischen Operationen in verschiedenen Farbräumen mikroskopische Bilder zu segmentieren und Fasern zu erkennen. Somit soll das Mikroskop derart gesteuert werden können, dass Spektraldaten ausschließlich an lokalisierten Fasern mit dem Raman-Mikroskop erhoben werden.

Im zweiten Teil der Studie wurden Raman-Spektren für mehrere Fasern verschiedener Herkunft und unterschiedlicher Farben gemessen. Die Versuchsanordnung hierbei entsprach einer realitätsnahen Situation, wie sie in der forensischen Beweisanalyse angetroffen wird. Die empirische Datenerhebung erfolgte in Zusammenarbeit mit der Universität für Bodenkultur Wien und dem Büro für Kriminaltechnik des Bundeskriminaltamtes.

Die Ergebnisse dieser Studie lassen den Schluss zu, dass die Implementierung des untersuchten Algorithmus zur Erkennung relevanter Fasern und zur Identifikation von Fasern bestimmter Farbe sinnvoll ist, um die momentan stattfindende manuelle Bearbeitung großer Mengen von Beweismitteln auf ein Minimum zu reduzieren. Die Untersuchung der Fasern mittels Raman-Spektroskopie in den vorgegebenen Rahmenbedingungen führte allerdings zu einer Reihe von Problemen, welche zum größten Teil auf die thermische Zersetzung der Fasern zurückzuführen sind.

Schlagwörter: Bildbearbeitung, Bildsegmentierung, Objekterkennung, Raman-Spektroskopie, Hyperspektrale Bildgebung, Fasernanalyse, Forensik

Abstract

This study is an initial attempt to investigate the feasibility of automating fiber analysis in forensic science using Raman spectroscopy. To enable self-directed collection of spectral data a sequence of image processing steps is presented in the first part of this thesis. Its purpose is to allow for image segmentation and separation of fibers from the background to reduce the amount of measuring locations.
Raman measurements have been conducted for various fibers of different fabrics and different dyes in an experimental setting which mimics real crime scenes rather than conventional sample preparation in spectroscopy. The empirical part of this study was conducted in cooperation with the University of Natural Resources and Life Sciences, Vienna and the Criminal Investigation Service Austria.

The results support the implementation of the algorithm presented to recognize fibers and search for fibers of a specific color to reduce the time consuming manual examination of a large set of evidence tapes. However the outcome of spectral examinations outlines several obstacles in using automated Raman spectroscopy, the majority of which are a direct result of thermal decomposition.

Keywords: Image Processing, Image Segmentation, Texture Analysis, Raman Imaging, Hyperspectral Imaging, Fiber Analysis, Forensic Analysis

Acknowledgements

First and foremost I would like to thank my thesis advisor Prof. Hans Lohninger for his exceptional support and guidance as a supervisor. He introduced me to the field of chemometrics and statistical learning which I came to enjoy a lot as a result of our meetings on classifiers. He helped me with great patience whenever I needed a push into the right direction.

I would also like to thank Prof. Notburga Gierlinger of the University of Natural Resources and Life Sciences, Vienna, for spending her precious time on helping me with the empirical acquisition of spectral data to conduct this study and passing on her valuable knowledge on spectroscopy.

Furthermore I want to express my gratitude to Dr. Robert Hirz of the Criminal Investigation Service Austria. Without Dr. Hirz' contribution and ideas to reshape the prevailing investigation methods in forensic science, this study could not have been conducted. Special thanks goes to forensic specialist Petra Rieck who patiently taught me the various aspects of collecting fibers as evidence.

In addition my appreciation goes to Dr. Johannes Ofner and Dipl.-Ing. Karin Wieland for their input on the interpretation of spectral data and to Dipl.-Ing. Elisabeth Renner for our invaluable conversations on classifiers.

Finally, I must express my endless gratitude to my mother Ingrid and to my partner Thomas for their constant support and continuous encouragement throughout my studies. Without their reassurance and care this thesis could not have been possible.

Contents

1 Introduction **1**
1.1 Background . . . 1
1.2 Statistics in Forensics . . . 3
1.3 Fibers . . . 4
1.4 Conviction Statistics . . . 4
1.5 Prevailing Method in Fiber Analysis . . . 6
1.5.1 Acquisition of Evidence . . . 6
1.5.2 First Fiber Selection . . . 7
1.5.3 Fiber Preparation . . . 8
1.5.4 Disadvantages of the Prevailing Method . . . 9
1.6 Proposal of a Novel Approach . . . 10
1.6.1 Novel Approach: Acquisition of Evidence . . . 12

2 Part I: Image Processing **13**
2.1 Image Acquisition . . . 13
2.1.1 Hyperspectral Images . . . 13
2.2 Color Spaces . . . 15
2.2.1 RGB Space . . . 15
2.2.2 HSV Space . . . 16
2.2.3 YCbCr Space . . . 17
2.2.4 L*a*b Space . . . 17
2.3 Binary Images and Logical Operations . . . 19
2.4 Spatial Operations . . . 19
2.4.1 Histogram . . . 20
2.5 Morphological Operations . . . 23
2.5.1 Structuring Elements . . . 23
2.5.2 Erosion and Dilation . . . 24
2.5.3 Opening and Closing . . . 25
2.5.4 Image Segmentation . . . 26
2.5.5 Global vs. Adaptive Thresholding . . . 26
2.5.6 Edge Detection . . . 29

2.6 Remarks and Limitations on the method 34

3 Fiber Detection Algorithm 36

3.1 Combining all color channels 43

3.2 Specific Fiber Search: Example Green Fiber 44

3.3 Dark Background 46

4 Part II: Raman Measurements 49

4.1 Confocal Properties 49

4.2 Image Formation 51

4.3 Frequency Dependence 53

4.4 Experimental Setting 55

4.5 Raman Mapping 57

4.6 Advantages of Raman Spectroscopy 57

4.7 Stokes Shift 58

4.8 Problems provoked by Fluorescence 59

4.8.1 WITec Raman Microscope 61

5 Data Analysis 62

5.1 Imagelab 62

5.2 Generation of Classifiers 62

5.2.1 Baseline Correction 62

5.2.2 Curse of Dimensionality 63

5.2.3 Spectral Descriptors 64

5.3 Definition of Training and Test Datasets 65

5.4 Random Forests 65

6 Results 67

6.1 Image Processing Results 67

6.2 Raman Spectral Results 67

6.2.1 Fluorescence 67

6.2.2 Indigo Dyed Fibers 70

6.2.3 Ocher Colored Polyester Fibers 72

6.2.4 White Cotton Fibers 75

7 Conclusions **77**
7.1 Feasibility of the Method 77
7.1.1 Complications during Experiments 77
7.1.2 Fluorescence 78
7.1.3 Focal Plane 78
7.1.4 Image Processing 79

Appendix A Algorithm Image Processing **80**
A.1 Main Routine 80
A.2 Considering all Color Channels 84
A.3 Color Thresholder App 86

Appendix B Spectral Results **91**
B.1 Experiments at 532nm 91
B.1.1 Sample B1 92
B.1.2 Sample G1 95
B.1.3 Sample O1 96
B.1.4 Sample O2 98
B.1.5 Sample R1 102
B.1.6 Sample S1 103
B.1.7 Sample W1 106
B.1.8 Sample W2 110

1 Introduction

1.1 Background

In criminal investigation fiber evidence can be an important aspect to link a suspect to a scene of crime or victim by finding similar textile fibers on the victim's and suspect's clothing. The decision if two fibers are similar enough to provide a link between two objects or individuals cannot be done by simple optical investigation. Two fibers may appear very similar in color and structure for the human eye, but can originate from different fabric. In many cases this confirmation is obtained by near-infrared spectroscopy (NIR). For multiple reasons, including the redundancy of sample preparation and sensitivity to detect low concentrations of present substances, many studies have shown promising results using Raman spectroscopy to identify fibers in forensic science ([1], [2], [3] [4]).

Examination of collected fiber evidence can be a highly time consuming manual labor. The idea of this thesis is to investigate an approach to automatically collect Raman data of all the fibers which are to be examined to allow straight-forward analysis of possible matches to a reference fiber. Fibers are collected by sticking a special adhesive tape onto a fabric in order to capture loose fibers by double folding the tape after pulling it off the sample fabric. The most straight-forward approach to simply scan the entire tape is unfeasible. Assume a tape of the size 100mm $\times$ 40mm. For a resolution of 1μm this gives 100.000 $\times$ 40.000 pixels. Sampling 1000 intensity values by Raman spectroscopy for every pixel, each consisting of at least 4 bytes this leads to $100.000 \times 40.000 \times 1000 \times 4 = 1.6 \times 10^{13}$ bytes. This yields in 16TB of data for each adhesive tape of the size of 100mm $\times$ 40mm. However it is possible that as many as 60 or 80 of these tapes are collected at a single crime scene. Therefore it is impractical to collect this much data, let alone the time it takes to conduct the measurements. Since it is impossible in regards of storage space and computational effort, the idea is to use image processing

techniques to control the sample at the stage of the microscope in such a way that spectral measurements are only taken at locations where a fiber is present. This reduces the number of measurements dramatically, since the majority of these tapes consists of glue rather than captured fibers.

The goal of this thesis is to evaluate the feasibility of automating fiber examination by Raman spectroscopy. The following questions were dealt with in the course of this study:

- Is it possible to automatically detect fibers in images of adhesive tapes by the means of image processing?
- Can the process of collecting Raman spectra of the fibers be automated in such a way that no manual sample preparation is needed?
- Do the Raman spectra obtained this way suffice to classify the origin of a fiber?

The idea of the automated process is as follows:

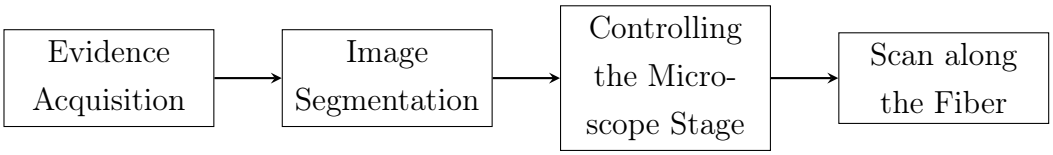

Part I of this thesis will deal with the necessary image processing steps to separate the fibers from the background on microscopic images. Part II will present empirical Raman data collected in a setup practicable in applied forensics, i.e. spectra obtained of fibers not prepared in an artificial environment as presented in other studies which try to analyze the general capabilities of Raman spectroscopy in uncovering the chemical composition of specific fibers.

1.2 Statistics in Forensics

Statistics is a fundamental tool in forensic science. There are various instances in which making up for uncertainty in evidence collection and assessment comes into play. It is used to link many different evidential types, such as ear prints, fingerprints, hair, paint, handwriting and documents with samples taken from suspects. Each problem is attended by posing a series of questions which need to be considered. Let us consider propositions of interest as pointed out in [5] regarding fiber analysis. Fibers might be transferred to a crime scene or space connected to the victim by the suspect or by chance. To decide whether, for example, the suspect sat on the driver's seat of a stolen car, or if the suspect never sat there, or perhaps the suspect sat on the mentioned seat a week earlier for legitimate reasons must be decided by the means of probability which takes into account information such as the number of fibers recovered, the materials involved and the intensity of actions considered. This thesis will not deal with questions of interpreting evidence and drawing conclusions such as if enough fibers are present to confirm one of the mentioned hypotheses connecting a suspect to the stolen car ([5]), but rather on the methods to decide if two fibers are drawn from the same source.

1.3 Fibers

In [6] fibers are characterized as linear elements made of fabric which appear longer than wide and to which dye was applied. Similarly [7] refers to a fiber as »*the smallest unit of a textile material that has a length many times greater than its diameter.*«
They can be categorized in three ways: natural fibers, made from animals or plants, such as wool, cotton or silk; synthetic fibers which are entirely man-made, e.g. polyester or nylon and manufactured fibers which are semi-synthetic as for example rayon (viscose).

Fibers proved themselves as a valuable kind of evidence because their origin can be determined relatively faultlessly. However, fibers are easily transportable, become airborne or get brushed off. This is why quick collection at the crime scene is crucial. The more time passes, the more likely it becomes that means of evidence are lost or material is cross-contaminated.

1.4 Conviction Statistics

Although fibers are easily collected for evidence in large quantities, they can be very time consuming to analyze and this approach might not be a reasonable way to proceed. In fact, in a majority of murder cases it is no suitable method at all. Table 1 shows the statistics of murder convictions in Austria in the years of 2007 to 2010[1]. Of course these numbers vary greatly from other countries and most likely also over the years, but it shows that most of the murders and murder attempts, which are the target application for fiber analysis, happen among acquaintances of some degree. Adding the cases which happened in families and among acquaintances, the numbers in table 2 are obtained. As a consequence fiber analysis is only applicable in roughly a quarter of all murder cases, because matching a suspect to a victim by the

[1] High-Risk Victims: Tötungsdelikte in Beziehungen, Verurteilungen 2008-2010, Bundeskanzleramt Österreich

means of fibers will not hold in court if the two were in contact for legitimate reasons.

Murder/Murder Attempts	2007	2008	2009	2010
Family relationship (shared living)	25	27	37	37
Family relationship (separate living)	13	16	23	17
Acquaintanceship	37	33	36	57
Chance acquaintanceship	5	10	14	12
No relationship	25	19	21	33
Relationship status unknown	2	0	7	1
Total	107	105	138	157

Table 1: Murder/murder attempts in families and the circle of acquaintances

Murder/Murder Attempts	2007	2008	2009	2010
Fiber analysis constructive	27 25.23 %	19 18.10 %	28 20.29 %	34 21.66 %
Fiber analysis obsolete	80 74.77%	86 81.90%	110 79.71%	123 78.34%

Table 2: Murder/murder attempts in which fibers could be used as means of evidence

1.5 Prevailing Method in Fiber Analysis

As of now the standard operating procedure to use fibers as forensic evidence involves multiple steps which will be explained in this section.

1.5.1 Acquisition of Evidence

At the scene of crime samples of fibers are collected by sticking and detaching an adhesive tape, thereby drawing off the fibers. The tape, as seen in figure 1 is subsequently two-folded and conglutinated to prevent any kind of further contamination of the fibers. The samples are taken to the Criminal Investigation Service Austria for subsequent examination. Since the majority of criminal cases reported in Austria turn out to be caused by personal problems following a certain degree of familiarity, a lot of samples will be collected during the first inspection of the crime scene, but not further considered.

Figure 1: Adhesive tape used to gather fibers at the scene of crime

The samples taken this way can look very differently depending on the situation in which they were acquired. Figure 2 shows two sample tapes taken from the same fabric, but the tape cut-out in figure 2(a) has been peeled off the original fabric multiple times, thereby increasing the number of fibers on the sample dramatically.
Similarly the outcome of the sample highly depends on the fabric of which it is extracted from, some are immensely fuzzy so that many fibers stick to the adhesive tape while others are smooth and only lose a small number of own fibers next to foreign ones.

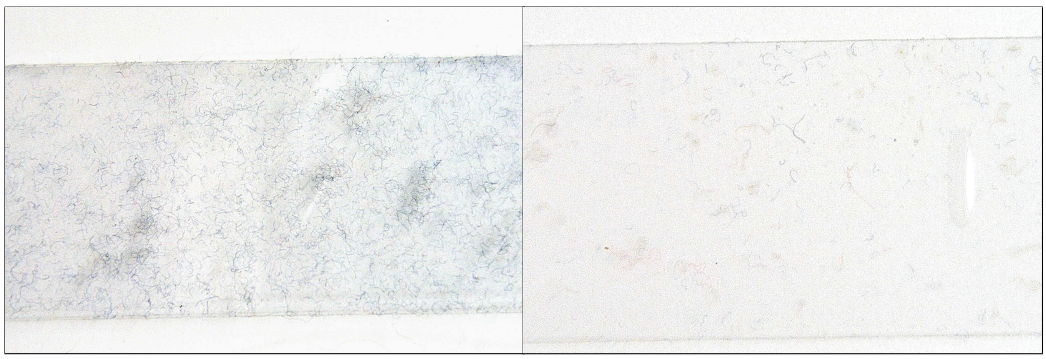

(a) High density of fibers on tape (b) Low density of fibers on tape

Figure 2: Example of a tape sample containing a high density of fibers

In instances which include blood at the crime scene or cases in which the samples have to be taken outdoors, the tapes can be very contaminated with blood and dirt. This is problematic insofar as that they occlude the fibers and in some severe cases restrain the adhesivity of the tape's glue.

1.5.2 First Fiber Selection

Once fibers of interest, for example, those found on the victim or on the suspect have been identified, they need to be matched to the suspect or scene of crime respectively. To do so, the first step is to take a close look of the samples in an optical microscope. One such section is shown in figure 3. It shows a collection of different fibers which have been collected from a desk chair. Suitable fibers have to be chosen manually by their size, color, curliness or the way they unravel. This step can be extremely time consuming.

Figure 3: Example of sample as seen through an optical microscope

Although the examination using an optical microscope reveals a lot of information about a fiber in terms of shape, color and thereby their origin to some degree, it is not possible to draw conclusions about the conformance of two fibers. To overcome this issue it is essential to study the underlying features using spectroscopy.

1.5.3 Fiber Preparation

Once the responsible forensic scientist has found fibers which potentially carry essential information about the case, it is necessary to take the fiber out of the tape. In order to do so, a small cut is made into the tape and the specific fiber is dissected. Using tweezers it is subsequently cleansed with ethanol to remove any residue of glue and arranged to be examined in an infrared microscope. The spatial resolution of IR microscopes is limited by diffraction, hence is related to the wavelength. In general the resolution can be assumed to 1-3$\times$ the wavelength depending on the particular instruments in use. In [8] the standards for forensic examination of fibers using IR spectroscopy are described to guide forensic research labs through the analysis of single fibers. The setup requires an IR spectrophotometer coupled with an IR microscope. Identification of the fiber's composition is made by comparison with reference spectra taken from one of the numerous databases. IR spectrometers are most often based on Fourier transform infrared (FT-IR)

in a laboratory setup.

The success of the method highly depends on the experience of the forensic scientist and the availability of exemplar and sample data. Often it is advisable to consider additional other examinations, e.g. fluorescence microscopy, polarized light microscopy and others. In special cases in which polymer identification is intricate despite the spectral measurements, it can be considered to carry out additional microchemical tests, determine the melting point, or apply pyrolysis methods. However these tests are highly destructive and require a large sample size to provide the possibility of repeatability and are to be avoided for forensic applications if possible.

1.5.4 Disadvantages of the Prevailing Method

There are multiple unwanted aspects about the technique in use thus far:

- Going through all samples collected at the crime scene manually by a trained forensic scientist is highly time consuming and expensive in terms of hourly wage.
- The tape requires dissection to prepare the fiber for IR analysis. This is in any case troublesome when dealing with evidence. It would be desirable to avoid any cuts into the sample to eliminate any chance of contamination in the lab or any time later than during the collection at the crime scene itself.
- Although the fiber is cleansed with ethanol after its excerption of the tape, in case of it being soaked in blood, it is practically impossible to remove all of the clotted blood from the fiber, which effects the absorption behavior of the fiber during the infrared inspection.
- The individual fiber dissected from the sample is relatively easily lost, damaged or might not hold in court, because the same one cannot be retained from the sample again by an independent lab, which poses a problem in case of a very low number of similar fibers present.

1.6 Proposal of a Novel Approach

The arguments produced in 1.5.4 led to the proposal to evaluate a new approach to tackle the problem of fiber analysis.
Raman Spectroscopy proved itself as an extraordinarily useful technique in determining the compounds of many different chemical samples. One of the strongest arguments in favor of Raman spectroscopy certainly is, that unlike IR which cannot pass through the glue on the adhesive tape far enough to reach the fibers and hence requires dissection, Raman spectroscopy shows no problems doing so.
Furthermore the time consuming task of checking all samples manually using a light microscope could be well enhanced by the employment of image processing techniques.

In the case of a successful application of Raman spectroscopy, the method should be very little destructive and the sample could stay intact, which allows measurements on the very same fiber multiple times. This would pose a major advantage if only few fibers are available.

The following page presents flowcharts which oppose the newly proposed method to the prevailing (old) method.

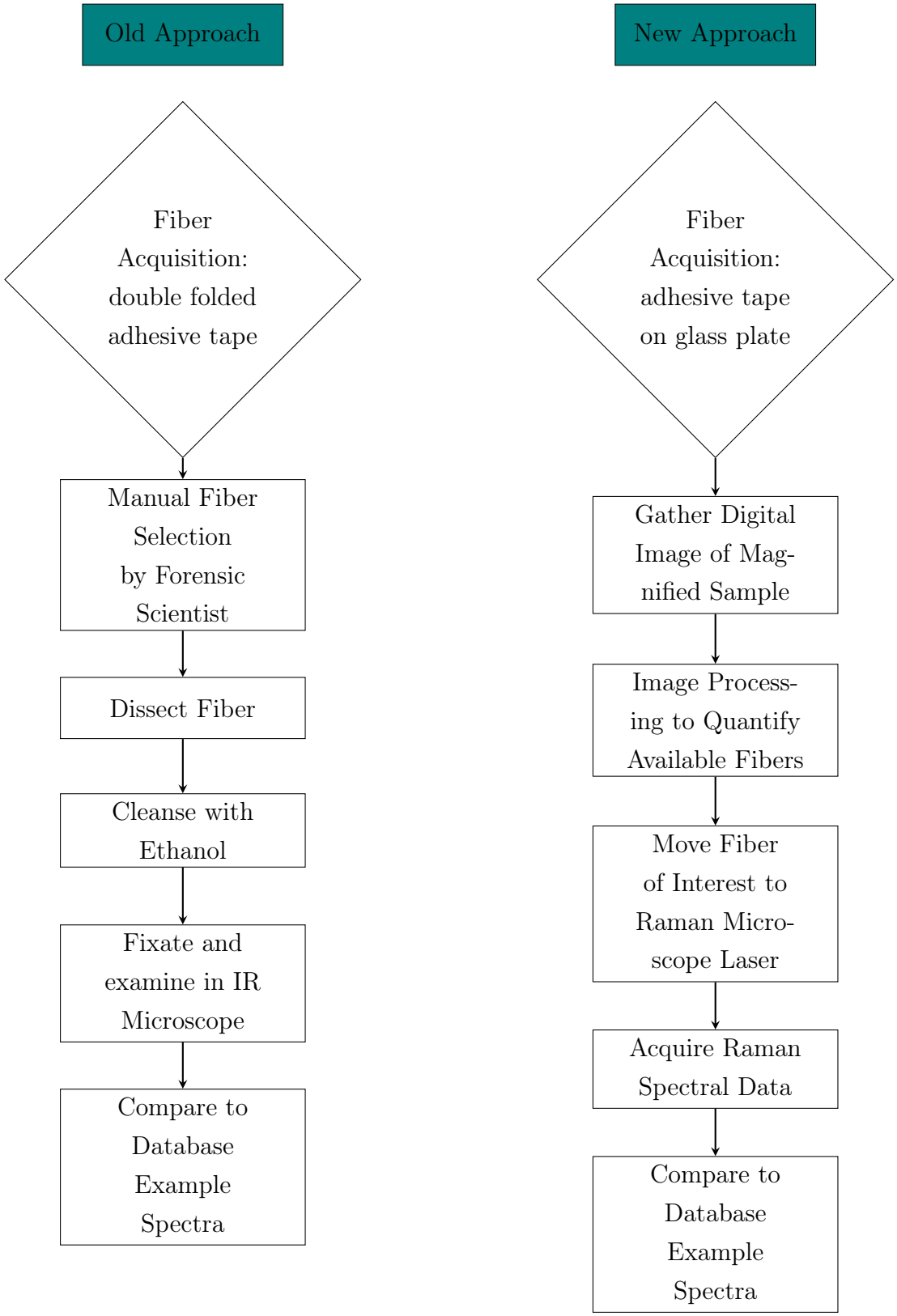
Old Approach
Fiber Acquisition: double folded adhesive tape
Manual Fiber Selection by Forensic Scientist
Dissect Fiber
Cleanse with Ethanol
Fixate and examine in IR Microscope
Compare to Database Example Spectra
New Approach
Fiber Acquisition: adhesive tape on glass plate
Gather Digital Image of Magnified Sample
Image Processing to Quantify Available Fibers
Move Fiber of Interest to Raman Microscope Laser
Acquire Raman Spectral Data
Compare to Database Example Spectra

1.6.1 Novel Approach: Acquisition of Evidence

To enhance the outcome of the trials using Raman microscopy to detect fibers, modifications in handling the adhesive tape have been made. Unlike double folding it after taking a sample of fibers, the adhesive tape has been stuck on a 0,17mm thick microscope slide. This provides the benefit that the sample is even and doesn't need fixation, but most of all it ensures that there are less layers of fibers and glue since the sample is only half as thick so that it is easier to locate fibers and scan along their surface. Glass has a weak Raman spectrum, hence it will not interfere with the signal coming from the fiber. Not allowing two sheets of glue and tape gives less freedom to the fibers to not lay planar and reduces the interference of glue signal with the actual signal resulting from the fiber.

Handling the glass slides at the crime scene can be understood as a complication of the procedure compared to the conventional method of double folding the tape. The glass has to be handled with additional care and material costs are higher, but the method promises reduced subsequent labor effort as well as non-destructive chemical measures.

2 Part I: Image Processing

In this part of the thesis the technical basis will be introduced to configure a machinery which automatically detects fibers and could be used to locate specific areas with the Raman microscopy setup to take measurements. The following chapter follows the theory provided in [9].

2.1 Image Acquisition

Acquisition of an image can be done in multiple ways, usually by registering electromagnetic radiation of some kind, which is then passed on in form of continuous waveforms which need to be digitized by sampling and quantization to turn the coordinate and amplitude values respectively into digital signals. This function $f(x, y)$ is stored as an array containing M rows and N columns, where the coordinates x and y commonly are represented as integers and span the *spatial domain.* It can be understood as follows:

$$f(x,y) = \begin{pmatrix} f(0,0) & f(0,1) & \cdots & f(0,N-1) \\ f(1,0) & f(1,1) & \cdots & f(1,N-1) \\ \vdots & \vdots & \ddots & \vdots \\ f(M-1,0) & f(M-1,1) & \cdots & f(M-1,N-1) \end{pmatrix}$$

2.1.1 Hyperspectral Images

While regular color images consist of three layers, namely, a red, green and blue band, it is possible that an image is formed by more than just three layers. For example, take wavelength bands which are 20nm wide between 400nm and 800nm as suggested in [10]. This results in every pixel having a spectrum of 21 wavelength bands, resulting in a *multivariate image.* It is

impossible to represent these images as color images because the human eye can only process three bands at a time, but they can be artificially colored by combining any three layers of the image. The color resulting from this procedure is referred to as pseudocolor.
Goetz et al. define the term *hyperspectral imaging* as synonymous with imaging spectrometry which refers to the acquisition of hundreds of spectral bands, see [11].

In this case the value for n is 100 or higher in the following definition:

Definition 2.1. *A digital image is a function* $f : \Omega \in \mathbb{Z}^2 \to \mathbb{Z}^n$ *or* $\mathbb{R}^n$*, where* $f(x, y, i)$ *is the amplitude or intensity for the i-th layer,* $i \in \{1, 2, \cdots n\}$ *corresponding to the contributions of the individual bandwidths.*

Hyperspectral images are characterized by many imaging layers corresponding to many wavelengths or bands to allow spectral interpretation and analysis. General multivariate images can be mixed mode, for example $f(x, y, 1)$ can be taken for an UV wavelength, $f(x, y, 2)$ a polarization image in white light and $f(x, y, 3)$ may correspond to a measurement taken at near infrared. Further information can be found in [10] or [12].

2.2 Color Spaces

Color spaces or color models serve the purpose for transforming one space to another in which certain computations can be executed more conveniently. A detailed introduction to color science can be found in [13].

2.2.1 RGB Space

The RGB, short for *red, green, blue*, color space corresponds to the human color receptors.
Adapting the definition 2.1 this means that $f : \Omega \in \mathbb{Z}^2 \rightarrow [0, 255]^3$ with $f(x, y, i)$ corresponding to the intensity of the i-th layer, precisely the red, green and blue contributions of the additive color model. It is based on a Cartesian coordinate system, forming a cube such as in figure 4.

Figure 4: RGB Cube in Cartesian coordinates: R, G, $B \in \left[0, 255\right]$. Source: [9]

Here the image is an array the size of $M \times N \times 3$. Each of the color planes can be treated individually and can be seen as a monochromatic image. Often it is sufficient to work with an *intensity image*, or otherwise known as a

grayscale image, combining the three channels into one monochromatic channel.

A common transformation of RGB images to grayscale images is by forming a weighted sum of the R, G, and B components:

$$I(x, y) = 0.2989 \times f(x, y, 1) + 0.5870 \times f(x, y, 2) + 0.1140 \times f(x, y, 3)$$

2.2.2 HSV Space

While the RGB color model is very suitable for hardware implementations such as television screens, its use is limited for describing color. HSV, short for *Hue, Saturation, Value*, often corresponds more accurately to how humans experience color than the RGB color space and hence is a favorable option for selecting colors. HSV is often referred to as HSB (Hue, Saturation, Brightness) and is similar but yet not to be confused with the HSL (Hue, Saturation, Luminosity/Lightness) color space. Hue is the dominant color perceived by a human and described as the dominant wavelength in a mixture of wavelengths in [9]. The purity or degree of mixture between white light and a hue is characterized by saturation. [14] describes saturation as a measure of how much white is in the color, or as it is put in [9], how diluted a color is. This means that pure red can be understood as more saturated than rose which appears as red containing more white.
[9] claims that »*brightness is a subjective descriptor that is practically impossible to measure*«.

The hue may vary from 0 to 1. The arrangement of corresponding colors in the cone shown in 5 which visualizes this color space, is as follows: red, yellow, cyan, blue, magenta, and back to red.

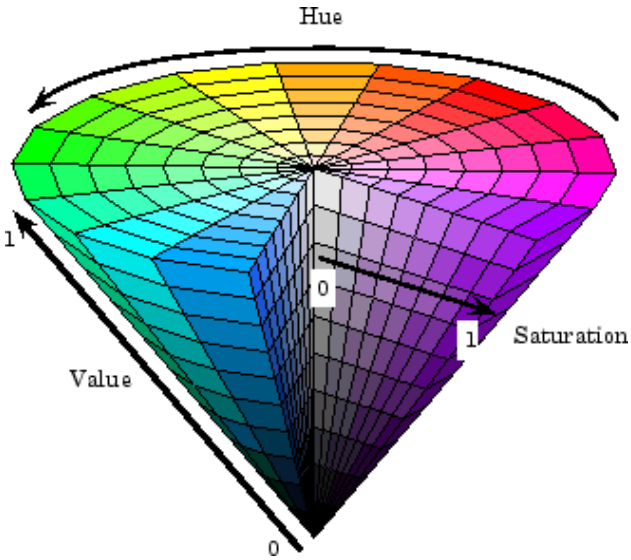

Figure 5: HSV Cone : V $\in [0,1]$, S $\in [0,1]$, H $\in [0,360]$. Source: [15]

2.2.3 YCbCr Space

The YCbCr color space is often used in digital video applications. Luminance, hence brightness or intensity, is carried in the component Y. Chrominance is responsible for the color information and is stored in two color-difference channels in Cb and Cr, see [15]. Cb gives the difference from the blue component to a reference value and so does Cr for the red component and a reference. All three parameters, Y, Cb and Cr range from 0 to 255.

2.2.4 L*a*b Space

L*a*b space was introduced by the *Commission Internationale de l'Éclairage* to find standard terms for describing color independent of the device in use, see [15]. It too is a three dimensional space with dimensions L, a^* and b^* referring to lightness and two color dimensions.

According to [9] the L*a*b* space is colorimetric, which means that colors which are perceived as identical are also encoded that way, as well as per-

ceptually uniform, meaning that deviating colors among different hues are perceived uniformly. The color space includes all colors of the visible spectrum, but also colors outside of human perception. Due to these properties it is the most exact way of representing color, but requires conversion to another, less accurate color space to be displayed. Similarly to the HSI and HSV system it decouples intensity from colors. The parameter a^* is given by red minus green and b^* by green minus blue, according to [9]. A visualization is shown in figure 6.

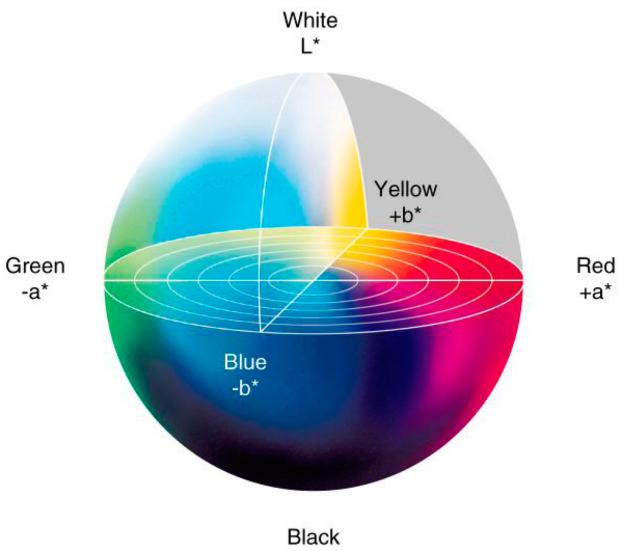

Figure 6: La*b* Color Space : L, a^*, $b^* \in \left[0, 100\right]$. Source: [16]

2.3 Binary Images and Logical Operations

Binary images are characterized by the fact that their pixels take values only in $\{0, 1\}$. Hereby the value 1 corresponds to white and 0 to black respectively. Since these kind of images are binary sets, one can apply logical set operators on them. Consider an object A_i as a connected set of pixels with value 1, and the total set of pixels as the full set Ω, the following operators hold for two objects A_i, $A_j \in \Omega$: $A_i \cup A_j$, $A_i \cap A_j$, $A_i \setminus A_j$, A_i^{C} and $A_i \triangle A_j$.

2.4 Spatial Operations

In [9] three kinds of pixel operations are presented: single-pixel operations, geometric spatial transformations and neighborhood operations. Intuitively single-pixel operations affect individual pixels regardless of the properties of their neighbors. The second category targets a set of pixels which are first transformed under a spatial transformation applied to the coordinates of the image and subsequently an interpolation of the intensity values for the new coordinates. These two steps are applied for example in rotation, translation, shearing or scaling transformations.

Neighborhood operations transform one pixel based on the information provided in this particular pixel's neighborhood. The size of the neighborhood may vary, but is chosen to be odd-sized, such as 3×3 or 5×5. A common application of neighborhood operators are averaging filters which calculate the average of all pixel values in the chosen neighborhood of pixel x_i and assign it to x_i itself.

Considering the smallest possible neighborhood, which is a 1×1 neighborhood, hence the current pixel itself, the neighborhood operator coincides with an intensity transformation function. Such a function may brighten up or darken pixels, thereby stretching the contrast. This function does not need to be linear throughout the entire set of pixels.

Let T be such an operator and k be a fixed value of intensity, then T can be used to segment an image by putting all pixel values to zero which originally have a value smaller than k, or to one if higher than the threshold.

This technique is called *thresholding* and can be written in the following way:

$$T\big[f(x,y)\big] = \begin{cases} 0 & \text{if } f(x,y) \leq k \\ 1 & else. \end{cases}$$

Since for many methods in image processing binary images are needed, thresholding is a simple but common technique encountered on many occasions.

2.4.1 Histogram

Figure 7 shows the conversion of an RGB image to a grayscale image by the means described in section 2.1. The image is a typical image which will be dealt with in this thesis, showing multiple fibers on a sample strip.

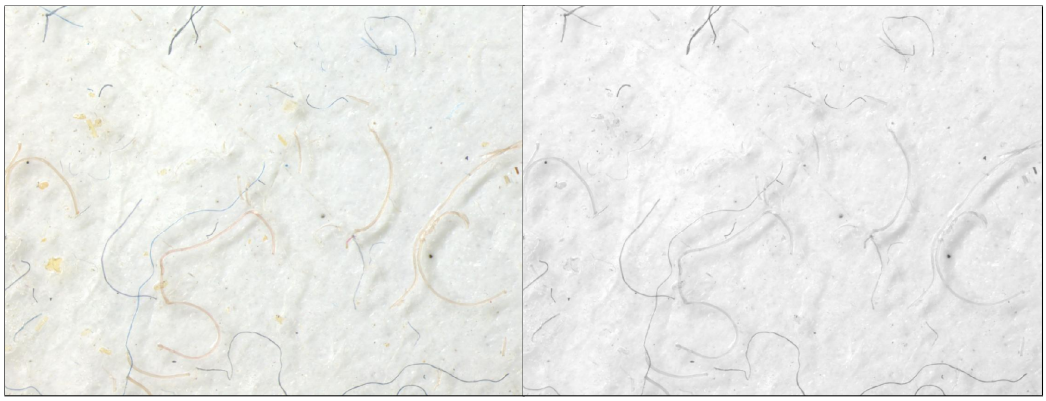

(a) Original RGB image (b) Intensity image of original

Figure 7: Comparison of the RGB image of fibers fixed between a glass platelet and forensic tape with its conversion to an intensity image

Of course it is essential to find a suitable threshold k which gives the optimal solution in terms or recognizing objects of interests and label them by putting their pixel values to one. Often a look at the histogram of the image pro-

vides insight on this issue. The histogram is a discrete function $h(r_j) = n_j$, where r_j is the j-th intensity value and n_j the according number of its appearance among the pixels. The histogram of the intensity image in figure 7 can be seen in figure 8. The number of pixels carrying information about the present fibers is relatively low compared to the number of background pixels and cannot be seen in the regular histogram shown in 8a. However by transforming the y-axis of the histogram plot to a logarithmic scale, as is done in figure 8b, the signal resulting from the fiber contribution can be clearly seen. This is the reason why Otsu's method introduced in section 2.5.5 fails to successfully segment the image. A non-linear transformation to enhance the signal of the pixels contributing to the fibers is presented in [17] and will be elaborated further in 2.5.5.

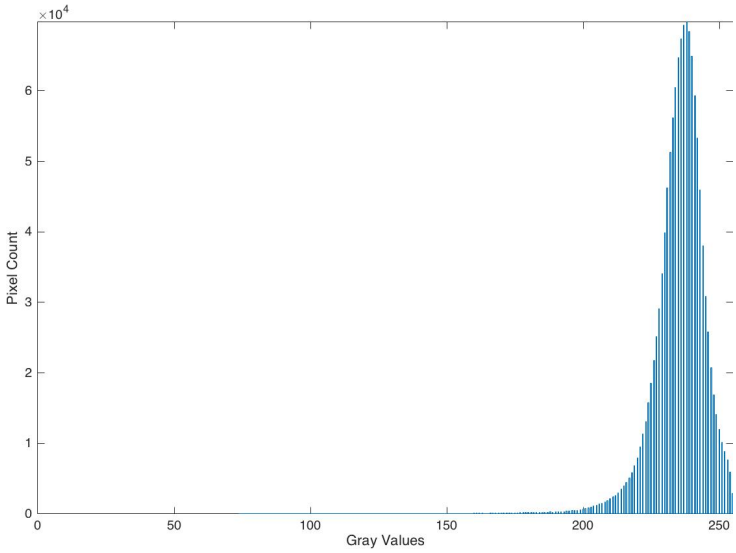

(a) Histogram of image from figure 7b

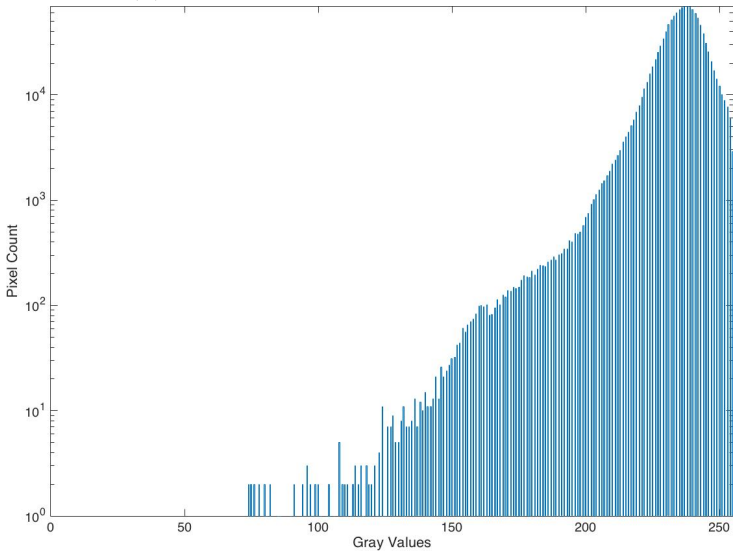

(b) Logarithmically scaled histogram

Figure 8: Histogram of intensity image shown in figure 7b in regular scale (a) and logarithmic scale in (b)

2.5 Morphological Operations

Morphological operators are defined on binary images, although there are analogous definitions for grayscale images for some operations. These methods require structuring elements which will be applied to the objects in the image. This means they are added or subtracted to objects in the binary image following rules defined by the specific morphological operation.

2.5.1 Structuring Elements

Structuring elements are small (sub-) sets of the image or independently defined structures. There are no restrictions on their shape or size. Some examples are:

$$SE_1 = \begin{pmatrix} 0 & 1 & 0 \\ 1 & 1 & 1 \\ 0 & 1 & 0 \end{pmatrix}, \quad SE_2 = \begin{pmatrix} 1 & 0 & 1 \\ 0 & 1 & 0 \\ 1 & 0 & 1 \end{pmatrix}, \quad SE_3 = \begin{pmatrix} 0 & 0 & 0 & 1 & 0 & 0 & 0 \\ 0 & 0 & 1 & 1 & 1 & 0 & 0 \\ 0 & 1 & 1 & 1 & 1 & 1 & 0 \\ 1 & 1 & 1 & 1 & 1 & 1 & 1 \\ 0 & 1 & 1 & 1 & 1 & 1 & 0 \\ 0 & 0 & 1 & 1 & 1 & 0 & 0 \\ 0 & 0 & 0 & 1 & 0 & 0 & 0 \end{pmatrix},$$

To understand their purpose, figure 9 shows the padding of an object A by the structuring element SE_1. The object A is scanned pixel by pixel. To each pixel of A the structuring element is (in this example) added by projecting the center of the SE onto A's pixel.

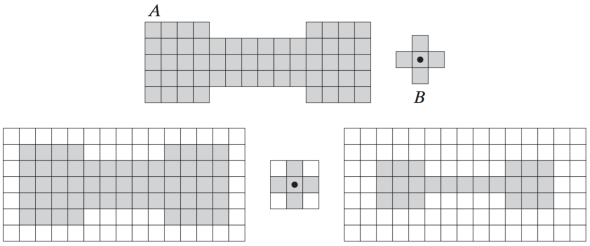

Figure 9: Structuring Element B padding object A. Both objects A and B are embed into rectangular pixel sets for computational reasons by adding background pixels. The black dot in B marks the center of the SE. Source: [9]

2.5.2 Erosion and Dilation

Erosion and dilation are frequently used morphological operations. They pose a duality to each other and in case of binary images, dilation is a Minkowski summation and defined as

$$A + B := \{a + b : \ a \in A, \ b \in B\}$$

The extension for grayscale images gives:

$$(A \oplus X)(x, y) = \max\{A(x + s, y + t) + X(s, t) : (s, t) \in D_X\}$$

where D_X corresponds to the domain of the mask. The white object in the image becomes enlarged by dilating, or adding, the structuring element onto each pixel belonging to the object.

Erosion is denoted by $A \ominus B$ and equals the application of dilation to the complementary image. For grayscale images it is defined by

$$(A \ominus X)(x, y) = \min\{A(x + s, y + t) - X(s, t) : (s, t) \in D_X\}$$

2.5.3 Opening and Closing

Opening and Closing are two operations which are composites of dilation and erosion. The opening of an image A by the structure element B is given by

$$A \circ B = (A \ominus B) \oplus B$$

while the closing can be expressed by

$$A \bullet B = (A \oplus B) \ominus B$$

The opening can be used to suppress noise, while the closing cannot remove any pixels, but might add new ones to the object. The composition of the dilation followed by the erosion closes all empty areas in which the structuring element doesn't fit. Thereby fully closed holes will not be re-transformed to the original by the following erosion.

In the case of binary images, the power set of all pixels can be defined as a lattice with associative and commutative operations on this set which fulfill $u \ominus (u \oplus v) = u$ and $u \oplus (u \ominus v) = u$. This lattice is complete and opening and closing as described above are two suitable operations. It can be shown that the opening is an anti-extensive operator, which can be interpreted as an operator whose image is smaller than the original, hence it is removing pixels, not adding any, because if an image x contains a subset y, the opening of x must contain the opening of y, but not necessarily a real subset, which leads to the reasoning, that the opening operator is not reversible in general, but discards information. Again, closing is an operator dual to opening and can be defined analogously to the complementary image.

2.5.4 Image Segmentation

A very important step in the process of object registration is *image segmentation*. Ideally every object of interest is defined as a distinct set of pixels, which can further be analyzed.

Following [9], image segmentation is defined as follows:

Definition 2.2 (Image Segmentation)**.** *For the spatial plane R of a digital image I, image segmentation finds a partition $\{R_i\}_{i=1,2,\ldots,n}$ such that:*

- $\bigcup_{i=1}^{n} R_i = R$,
- R_i *is a connected set* $\forall i \in \{1, 2, \ldots, n\}$,
- $R_i \cap R_j = \emptyset, \quad \forall i \neq j$,
- $Q(R_i) = 1, \quad \forall i \in \{1, 2, \ldots, n\}$,
- $Q(R_i \cup R_j) = 0$ *if* $R_i \cup R_j$ *gives a connected set.*

where the function Q is an indicator function for a specific intensity or fixed number of pixels. The last two items ensure that two adjacent sets are separable at all times.
Morphological operations as described in 2.5.2 and 2.5.3 might be needed to eventually separate merged objects.

2.5.5 Global vs. Adaptive Thresholding

A very effective, simple, and often applied method for segmentation is thresholding as introduced in chapter 2.4. Sometimes problems are encountered when one single threshold is chosen for the entire image, due to illumination changes throughout the spatial plane. [18] introduces multiple approaches of finding optimal thresholding solutions.
The most common implementation to evaluate a suitable threshold k is given by *Otsu's method*, see [19]. In a first step two clusters of pixels are presumed. Next the inter-class variance of these two classes is maximized. Thereby the

intra-class-variance is minimized and the optimal threshold to separate the two classes is found. Obviously, this approach can be extended from two to multiple classes.
Non-uniform illumination or reflectance effects can be tackled by image partitioning, where a different threshold is chosen for each partition of the image. This can be tuned as finely as necessary.

(a) Original RGB (b) Segmentation by Otsu's method

Figure 10

Segmentation using Otsu's method to the grayscale transformed original image is shown in 10. Since the fibers consist of only a small number of pixels, the outcome is rather poor. A non-linear transformation of the pixels described in [17] enhances the outcome significantly. Let I_o be the original image array, L_h a chosen threshold and I_t the transformed outcome:

$$I_t(i,j) = \begin{cases} \frac{L_h}{\sqrt{L_h - I_o(i,j)}+1} - \frac{L_h}{\sqrt{L_h}+1}, & I_o(i,j)) \leq L_h \\ I_o(i,h), & \text{otherwise} \end{cases}$$

If $L_h = 210$ is chosen for the image in 10a, the segmentation by Otsu gives the result shown in figure 11b.

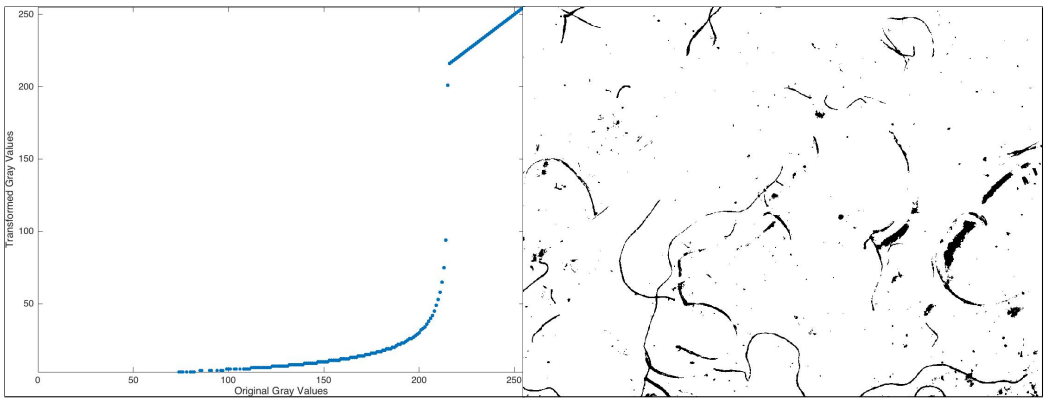

(a) (b)

Figure 11: (a) shows the non-linear transformation of gray values proposed in [17]. (b) shows the thresholded image using Otsu's method after the transformation.

The transformation enhances the signal contributed by the fibers. It enables Otsu's method to locate the centers of the two clusters of pixels in the histogram closer to their real position - namely the set of background pixels and fiber pixels.

2.5.6 Edge Detection

Most edge detectors operate contrarily to averaging filter, which smooths an image due to their integration-like behavior. Edge detection is based on the idea to take derivatives of an image pixel-wise. By computing the gradient between two pixels, in other words the difference in intensity values of the two, the changes will be perceived as edges, but will be close to zero if the pixel values are alike. There are multiple edge detectors described in [9] and applications described in [20], the most popular being *Canny edge detector*, *Laplacian of Gaussian*, *Prewitt*, *Roberts* or *Sobel*.

Canny edge detector, as presented in [21], uses the derivative of a Gaussian filter to calculate the gradient of the image and subsequently looks for the local maxima of the gradient. It distinguishes between strong and weak edges by using two different thresholds. The latter are included in its detection whenever they are connected to strong edges, which gives the detector a more favorable behavior in the case of noise. The Laplacian of Gaussian (LoG) detector, perceives the change of sign, usually referred to as zero-crossing, of the derivative after applying a LoG filter to the image.
In principle the other detectors compute the gradient as well, but all in a slightly different way, thereby providing different output. Roberts, Sobel or Prewitt use filters, similar to structuring elements which they convolute with the image to consequently calculate the derivative. Roberts edge detector uses a structuring element SE_R:

$$SE_R = \begin{pmatrix} -1 & 0 \\ 0 & 1 \end{pmatrix}$$

while Sobel uses the following masks:

$$SE_{Sx} = \begin{pmatrix} 1 & 0 & -1 \\ 2 & 0 & -2 \\ 1 & 0 & -1 \end{pmatrix}, \quad SE_{Sy} = \begin{pmatrix} -1 & -2 & -1 \\ 0 & 0 & 0 \\ 1 & 2 & 1 \end{pmatrix}$$

The Sobel operator uses two structuring elements for the two dimensions of the image, often referred to as kernels. Both are convoluted with the image I by $F_x = I * SE_{Sx}$ and $F_y = I * SE_{Sy}$, where the convolution is defined as a two step process explained by the following example:

Let I be an intensity image in the form of:

$$I = \begin{pmatrix} 2 & 3 & 1 \\ 0 & 4 & 2 \\ 1 & 1 & 3 \end{pmatrix}$$

and let B be the structuring element or convolution mask with which I will be convoluted:

$$B = \begin{pmatrix} 0.5 & 1 & 0.5 \\ 0.25 & 1 & 0.5 \\ 2 & 1 & 2 \end{pmatrix}$$

First it is necessary to pad I with zeros for computational reasons:

$$I \text{ padded} = \begin{pmatrix} 0 & 0 & 0 & 0 & 0 & 0 & 0 \\ 0 & 0 & 0 & 0 & 0 & 0 & 0 \\ 0 & 0 & 2 & 3 & 1 & 0 & 0 \\ 0 & 0 & 0 & 4 & 2 & 0 & 0 \\ 0 & 0 & 2 & 1 & 2 & 0 & 0 \\ 0 & 0 & 0 & 0 & 0 & 0 & 0 \\ 0 & 0 & 0 & 0 & 0 & 0 & 0 \end{pmatrix}$$

Additionally the kernel B must be rotated by 180 degrees, otherwise a closely related concept, *spatial correlation*, is performed. Hence B is rotated and becomes:

$$B^r = \begin{pmatrix} 2 & 1 & 2 \\ 0.5 & 1 & 0.25 \\ 0.5 & 1 & 0.5 \end{pmatrix}$$

Next the mask is overlaid on the image and the Frobenius inner product of the subimage with which the mask coincides and the mask itself, is performed. Thereby the pixels of the mask are multiplied with the corresponding pixels in image I and the results are summed up.

For example let the mask be laid over the subimage I^r in I marked as red:

$$I \text{ padded} = \begin{pmatrix} 0 & 0 & 0 & 0 & 0 & 0 & 0 \\ 0 & 0 & 0 & 0 & 0 & 0 & 0 \\ 0 & 0 & 2 & 3 & 1 & 0 & 0 \\ 0 & 0 & 0 & 4 & 2 & 0 & 0 \\ 0 & 0 & 2 & 1 & 2 & 0 & 0 \\ 0 & 0 & 0 & 0 & 0 & 0 & 0 \\ 0 & 0 & 0 & 0 & 0 & 0 & 0 \end{pmatrix}$$

Precisely the Frobenius inner product of I^r and I^b is defined as follows:

$$\begin{aligned} \langle I^r, B^r \rangle = \sum_{i,j} \overline{A_{ij}} B_{ij} = & \overline{A_{11}} B_{11} + \overline{A_{12}} B_{12} + \cdots + \overline{A_{1m}} B_{1m} \\ & + \overline{A_{21}} B_{21} + \overline{A_{22}} B_{22} + \cdots + \overline{A_{2m}} B_{2m} \\ & \vdots \\ & + \overline{A_{n1}} B_{n1} + \overline{A_{n1}} B_{n2} + \cdots + \overline{A_{nm}} B_{nm} \end{aligned}$$

Executing the calculation of the inner product of the subimage in red and the kernel, we obtain:
$2 \times 0 + 1 \times 0 + 2 \times 0 + 0.5 \times 0 + 1 \times 0 + 0.25 \times 0 + 0.5 \times 0 + 1 \times 0 + 0.5 \times 2$ equal to 1. The mask is now moved from pixel to pixel and the calculation of

the inner product is done for each constellation which replaces the original subimage's center pixel.
In the last step the remaining zero padding is removed and we obtain:

$$I * B = \begin{pmatrix} 1 & 3.5 & 4.5 & 2.5 & 0.5 \\ 0.5 & 4.75 & 9.25 & 6.5 & 1.5 \\ 4.5 & 10.5 & 16.5 & 14.5 & 4.5 \\ 0.25 & 9.25 & 10.25 & 13.5 & 5.5 \\ 2.0 & 3.0 & 9.0 & 5.0 & 6.0 \end{pmatrix}$$

Finally, using Sobel filters on an image usually requires the convolution with both its structuring elements. Often the magnitude of the resulting gradients is of interest which can be obtained by $F = \sqrt{F_x^2 + F_y^2}$.

These methods are well described in [22] and [23].

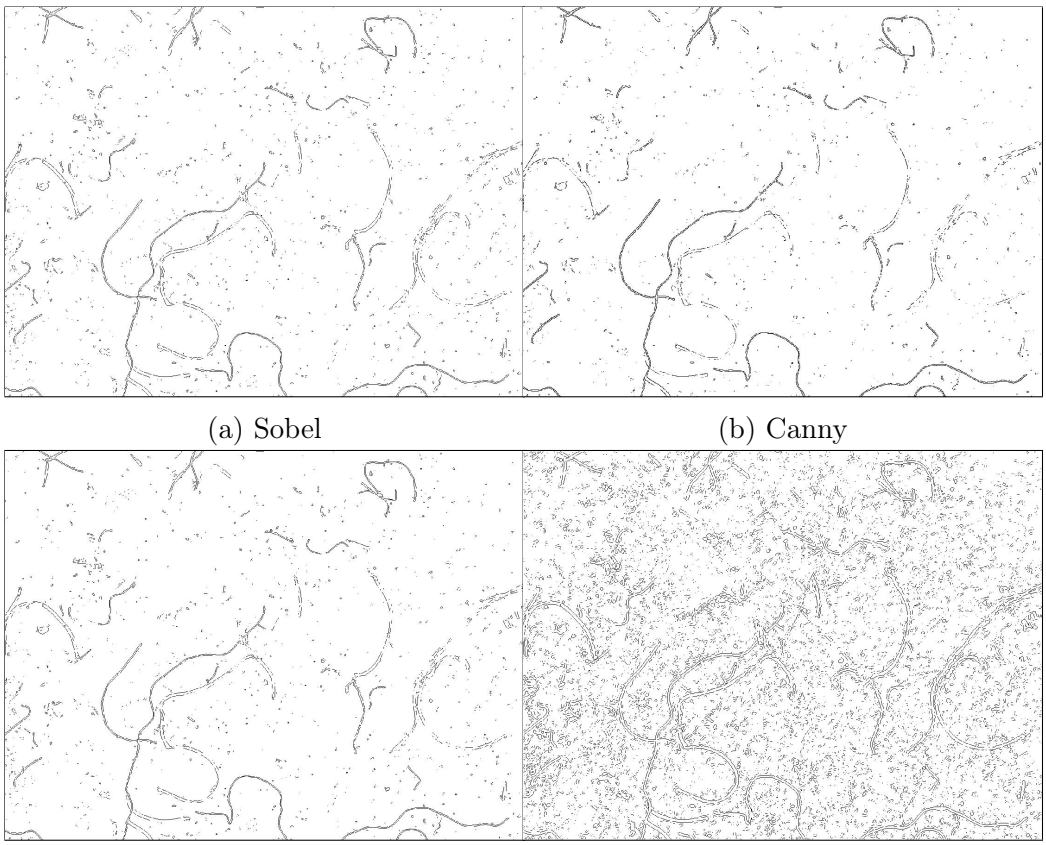

(a) Sobel (b) Canny

(c) LoG (d) Prewitt

Figure 12: Application of different edge detection methods

Figure 12 shows the application of different edge detectors to the image of figure 7. They show differences in the way they perceive edges, although it must be noted that in this figure they were applied on the grayscale image of the original image without any fine tuning of the parameters. Still it can be seen that the Canny edge detector suppresses more noise than the others while Prewitt gives the worst result of the four.

2.6 Remarks and Limitations on the method

There are instances in which the samples are highly contaminated with blood, dust, hair or tissue. It is possible that in those cases the algorithm fails due to the inconsistent background which makes segmentation very hard and will require manual examination by a human analyst as before.
Additionally the images taken must be in a raw format such `.nef` or `.tiff` format, which take up a large amount of storage. Because the main characteristic of the fibers is their color, it is impossible to use formats, such as `.jpeg` due to their lossy compression. JPEG compression is based on a discrete cosine transform which transforms the image from its spatial domain to its frequency domain. In the frequency domain it is quantized, thereby reducing the size of information carried by the image. In this process especially the high frequency components of the image are lost which correspond to the edges in the image. Hence the lossy JPEG algorithm proved itself useful to compress data with smooth changes in color, but not when sharp contrasts are important or the original data has to be reproduced such as in scientific imaging. The data format `png` on the other hand uses lossless data compression which avoids color bleeding as encountered when using `jpeg`, but will not reduce the file size significantly. In figure 13 the comparison of the two formats is shown for a blue fiber. As can be seen, the `jpeg` version provides less and different color features. It does not disturb the human eye to recognize the object and overall color, but impedes the classification of fibers by color and morphology dramatically.

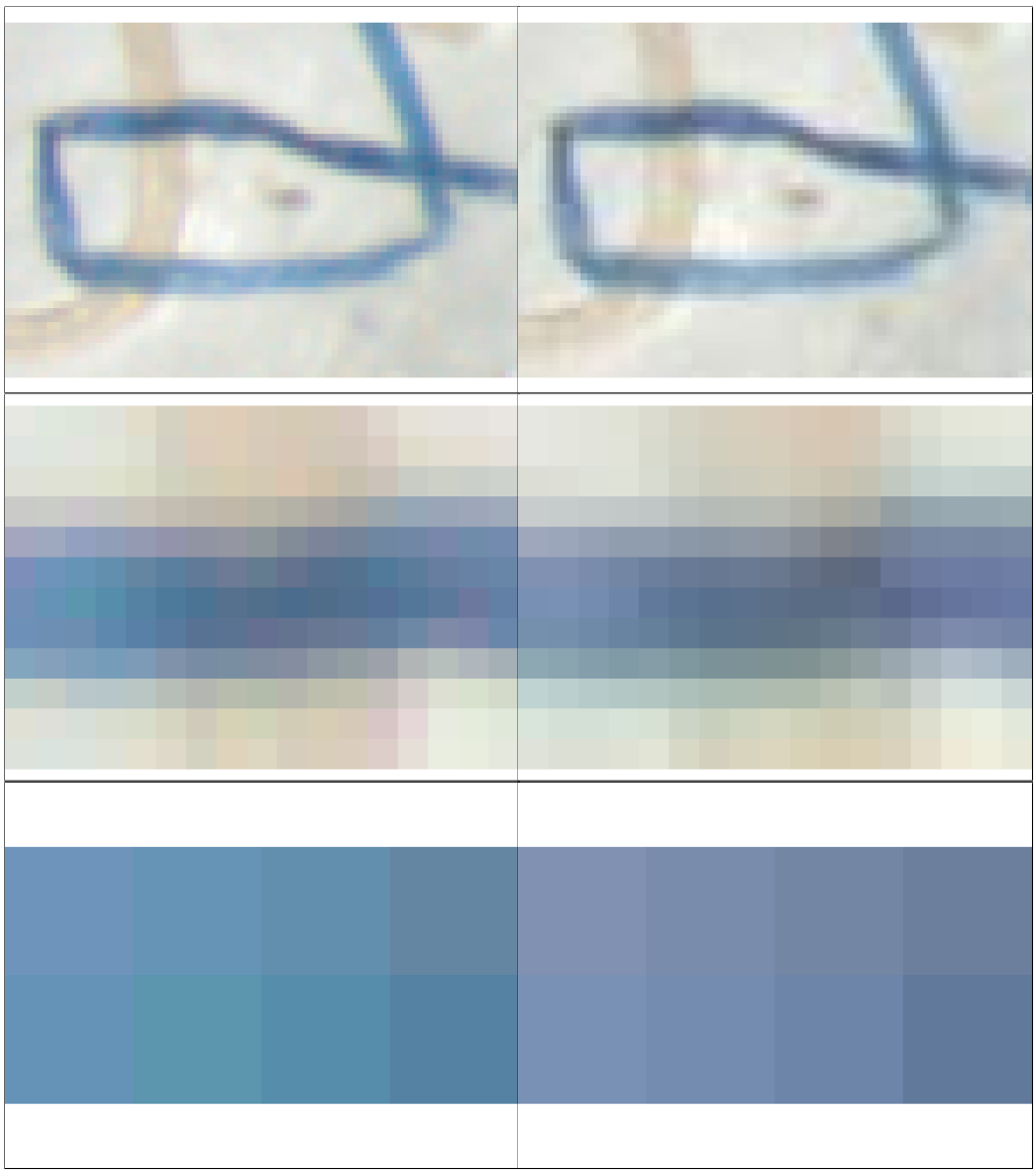

(a) Tiff (b) Jpeg

Figure 13: (a) shows a section of an uncompressed image in different zoom levels (b) shows the same sections after lossy compression using JPEG compression.

3 Fiber Detection Algorithm

In this section the code presented in appendix A will be explained. The purpose of the algorithm is to segment images as in figure 14(a) in such a way that the fibers form a binary mask. Ultimately this could be introduced to automatically steer the sample slides to favorable locations along these fibers in order to take spectral measurements.

Figure 14 shows the original image, which will be used in this chapter to visualize the individual steps of the algorithm. Furthermore it shows the red, green and blue component channels, as described in section 2.1.

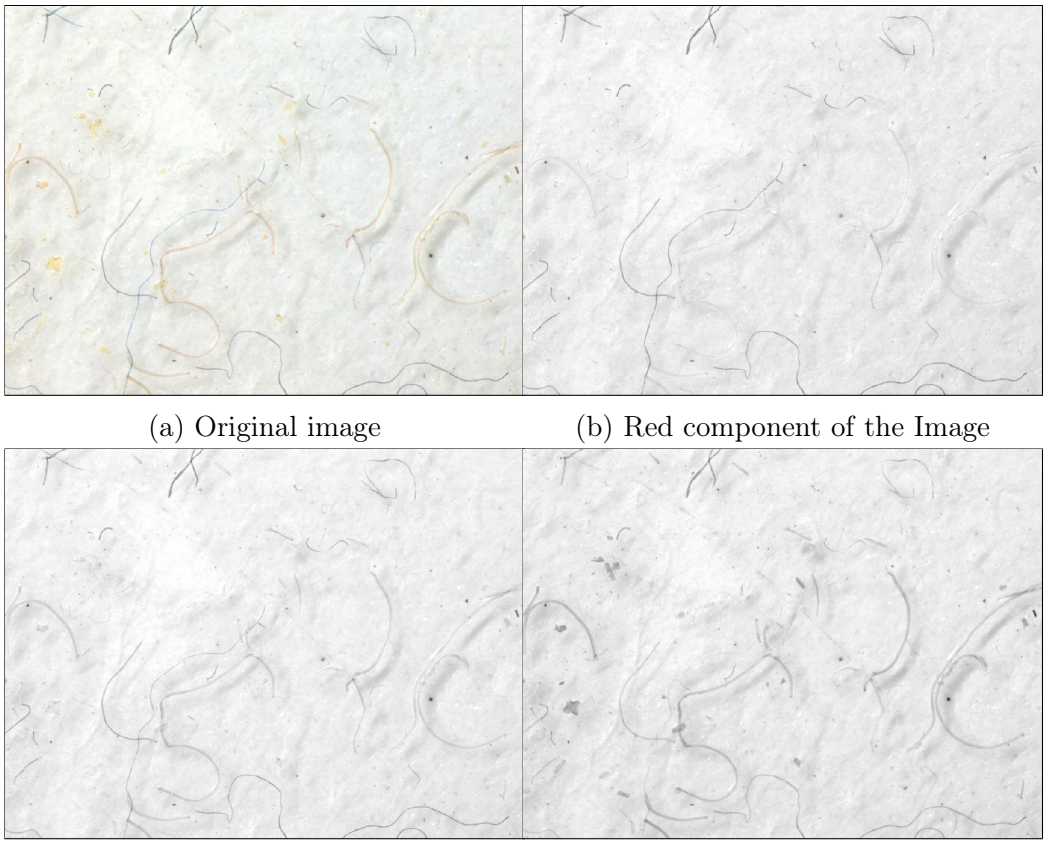

(a) Original image (b) Red component of the Image

(c) Green component of the Image (d) Blue Component of the Image

Figure 14: Original image and its red, green and blue color components

First the image is decomposed into its three color channels. The next step consists of subtracting one channel from another. The algorithm takes the chosen two channels as input. Figure 15 (a) shows the result of subtracting the blue channel from the red channel. 15 (b) shows its conversion to a binary image by using Otsu's method as introduced in 2.5.5.
(c) shows the application of a 2D median filter to reduce noise. After the filter's application each output pixel contains the median value of a 3×3 neighborhood of the corresponding pixel in the input image, which in turn is equivalent to a smoothing of the image. In (d) all objects smaller than 13 pixels are removed to further reduce the number of artifacts in the image.

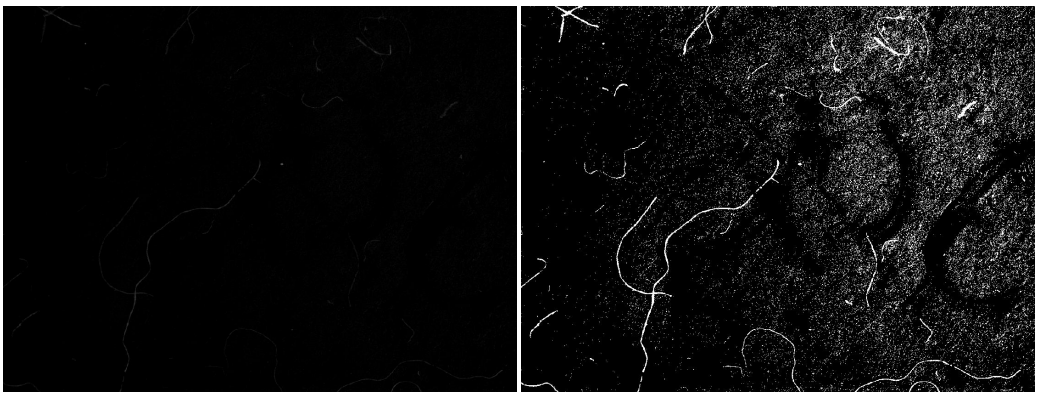

(a) Blue component subtracted from red (b) Segmentation of (a) by Otsu's method

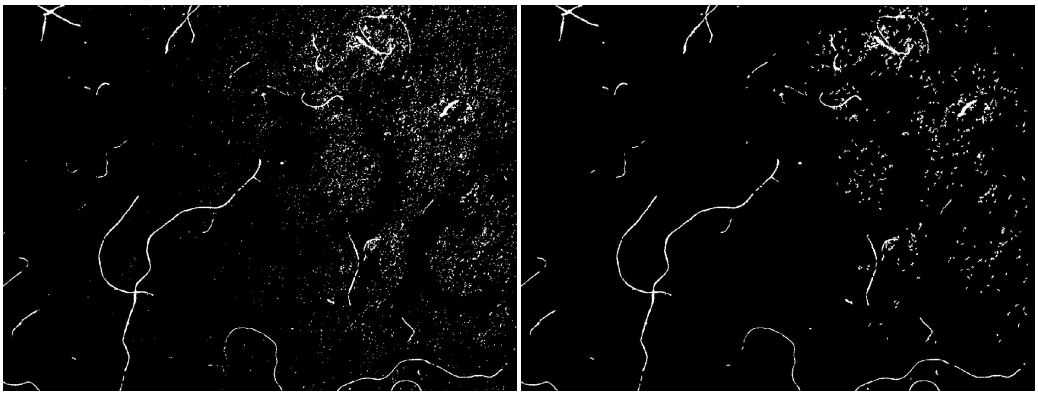

(c) Median Filter to remove noise (d) Removal of objects smaller than 13px

Figure 15: First processing steps

Next the skeletons of all objects are formed. This is done by removing pixels from the object's boundary without breaking it apart. The pixels remaining make up the image skeleton. This option preserves the Euler number of the image, which is the total number of objects minus the total number of holes in the image.
To remove still remaining artifacts in the image the endpoints of the skeleton, as well as the branchpoints are removed.
Endpoints are the extreme points of the skeleton, for example for a 4 pixel long skeleton of an object, such as:

$$\begin{pmatrix} \textcircled{\mathbf{1}} & 0 & 0 & 0 \\ 0 & 1 & 0 & 0 \\ 0 & 0 & 1 & \textcircled{\mathbf{1}} \end{pmatrix},$$

the endpoints are marked by the circled ones. A branchpoint on the other hand is defined in the following way:

$$\begin{pmatrix} 1 & 0 & 0 & 0 \\ 0 & 1 & 0 & 1 \\ 0 & 0 & \textcircled{\mathbf{1}} & 0 \\ 0 & 0 & 1 & 0 \\ 0 & 0 & 1 & 1 \end{pmatrix}$$

In figure 16(b) both the branch- and endpoints have been removed to split the small artifacts which can be seen in the right part of the image in (a). It does split up the longer objects as well, but this can be taken care of in a later step. Removing all objects smaller than 13 pixels after the subtraction of branch- and endpoints cleans the image of a majority of noisy objects. To reconnect the remaining objects a modified closing operator, as introduced in section 2.5.3 is applied to the image. It is not the conventional closing operator since the structuring elements of the dilation and erosion differ from each other. For the dilation an SE in form of $(a_{ij}) \in \mathbb{R}^{7\times 7},\ a_{ij} = 1,\ \forall i,j \in \{1,2,\ldots,7\}$ and for the erosion $(a_{ij}) \in \mathbb{R}^{3\times 3},\ a_{ij} = 1,\ \forall i,j \in \{1,2,3\}$ has been used, the

effects shown in figure 16 (c) and (d).

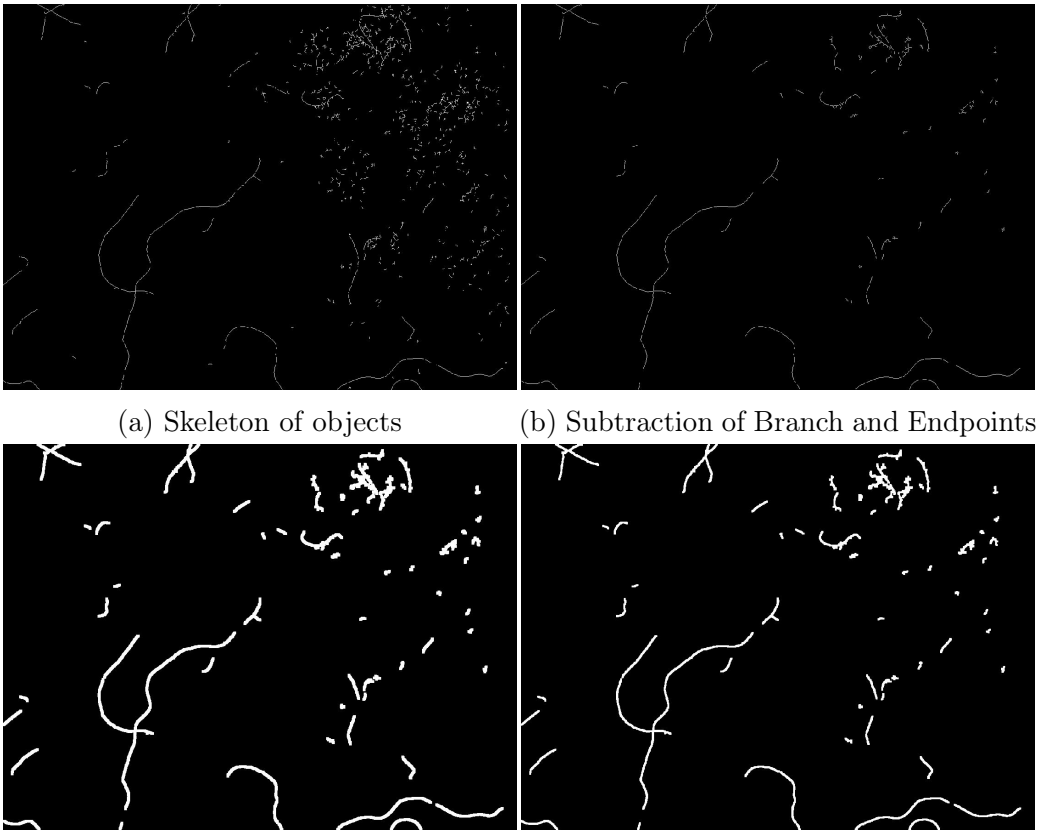

(a) Skeleton of objects (b) Subtraction of Branch and Endpoints

(c) Dilation by SE of size 7 (d) Erosion by SE of size 3

Figure 16: Further processing steps. In (b) objects smaller than 13 pixels were removed after the subtraction of end- and branchpoints.

The modified closing operator reconnects the split sections of the fibers which originated by the removal of branchpoints in a previous step.
There are still small objects present that are not of interest. To remove even more of them, the morphological operation to obtain the skeleton is again applied, this time evoking a lot less branches on the main fibers. The small objects that shall be eliminated show a very different structure than the linear, long and narrow shape that characterizes fibers. They are more compact and in case they have multiple branches it is not clear which of them is supposed to be the main branch. The newly calculated skeleton is shown in figure 17 (a). In (b) all present branchpoints are visualized by red

circles. It can be seen that the small objects which correspond to noise in the segmentation agglomerate lot more of them than the long, true fibers. Regarding all connected components in the image, the centroids of objects, visualized as blue stars in (c), can be understood as centers of mass of their pixels.

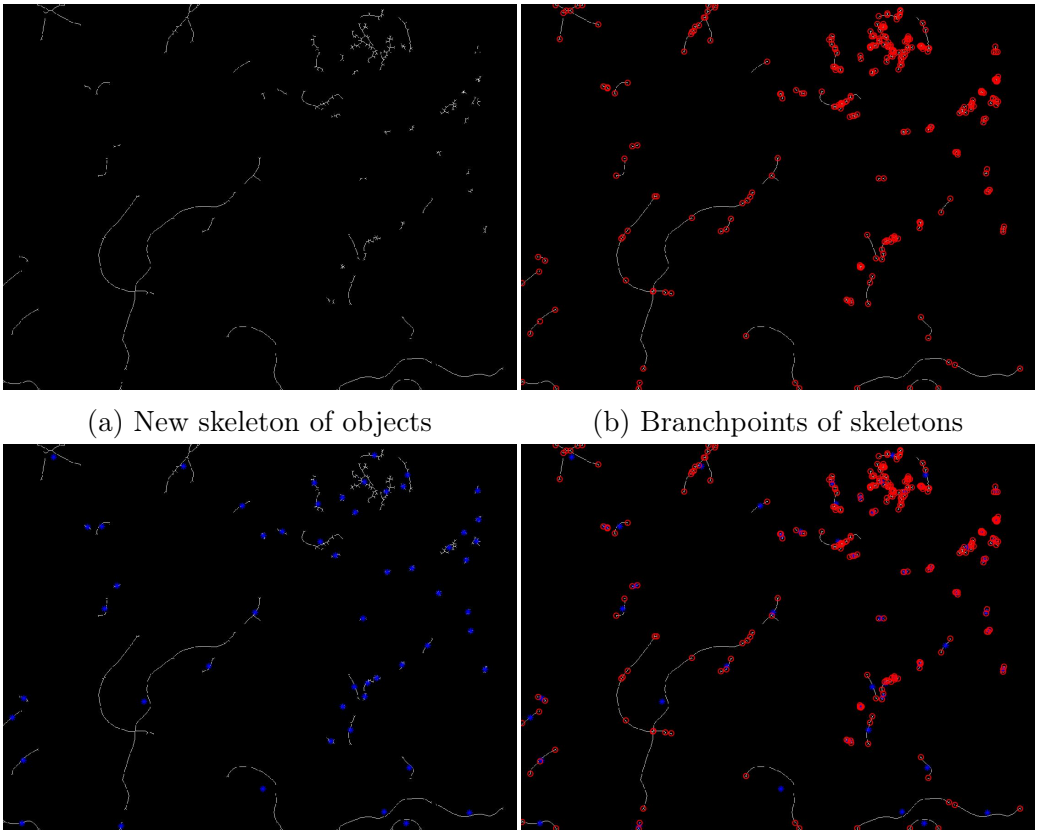

(a) New skeleton of objects (b) Branchpoints of skeletons

(c) Centroids of connected components (d) Branchpoints and centroids

Figure 17: (d) shows centroids of connected components in blue and branchpoints of skeletons in red

Figure 18 shows a typical artifact structure in (b). It shows a total of four branchpoints which belong to one object, or one centroid respectively. In the next step all objects that have multiple branchpoints close to the centroid are marked in figure 18 (a). These are removed from the image to clear the picture.

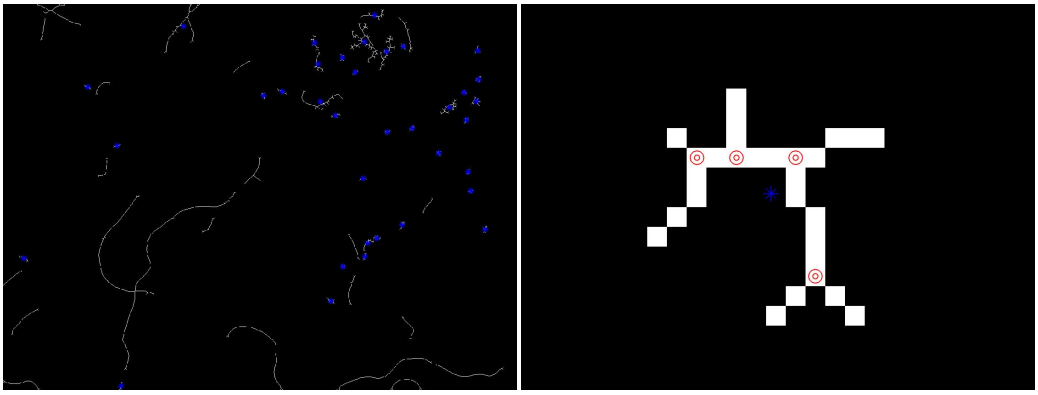

(a) Centroids which are to be removed (b) Branchpoints and centroids zoomed

Figure 18: Objects which show multiple branchpoints in a close distance to the centroid of the object are to be removed because they do not follow the typical linear shape of fibers

Each object can now be regarded separately. One such an example is illustrated in 19.

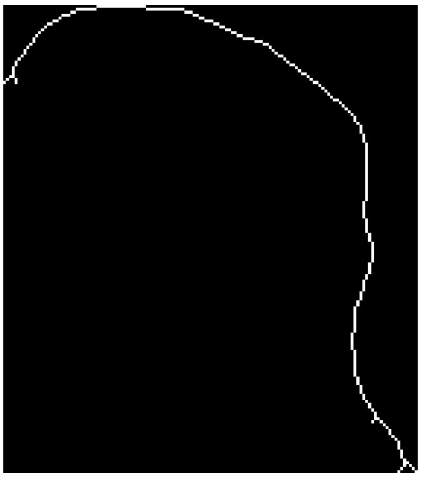

Figure 19: Example of fiber skeleton

By examining the skeleton of the fiber, only the very center part of the fiber is reviewed. The fiber itself has a bigger diameter. However, since the ultimate goal of the image processing step is to program a microscope scanning function to target a fiber by itself and scan at the chosen area, it

is reasonable to consider the skeleton of the fiber since this assures that the fiber is hit by the laser of the microscope.

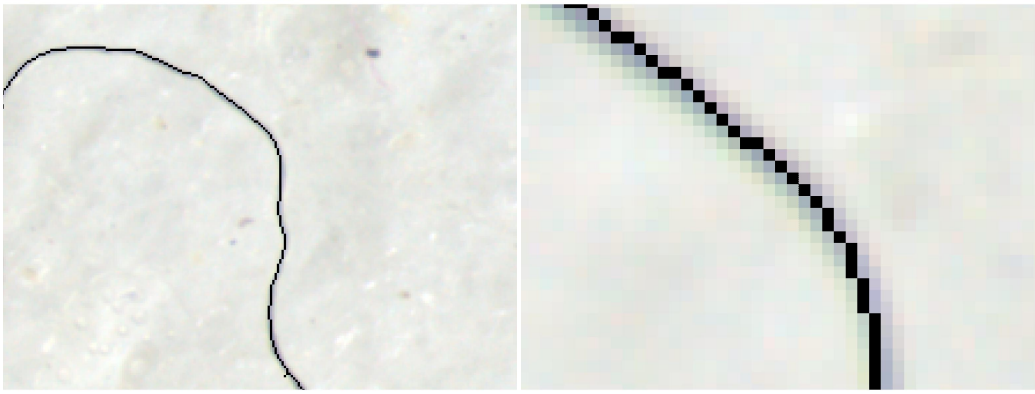

(a) Projection of the skeleton (b) Detail of the projected skeleton

Figure 20: The skeleton obtained by the image processing steps is projected onto the original image, here showing an excerpt of a blue fiber for two different zoom factors.

3.1 Combining all color channels

In the previous section the idea of the algorithm was explained by subtracting the blue channel from the red one. Of course not all fibers are detected by this method. The procedure is repeated for all combinations of channels, as presented in the code in appendix A.2. For each combination the routine provides a binary mask as output which will be added to each other. The code also cleans the image from skeletons including many branches. An example of a binary mask made up by all combinations of color channels is shown in figure 21.

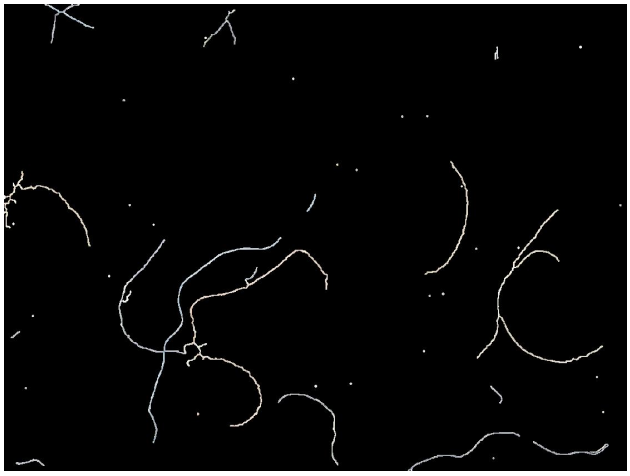

Figure 21: Combination of binary masks

3.2 Specific Fiber Search: Example Green Fiber

Consider the instance that a specific fiber has been found on a victim and samples are taken from multiple suspects. Using the color specifications of this fiber, it is possible to search through the set of images of the tape samples, and mark possible candidates. The code provided in A.3 informs the user if such an object is found in an image. This can be implemented to automatically target the laser onto specific locations of the sample.

As an example a green fiber was chosen in one of the sample images for the simple reason that it did not appear as frequently as the blue or ocher colored fibers, so that it was possible to verify manually if any fibers were missed by the algorithm. The procedure requires the user to mark fibers of interest in Matlab's `Color Thresholder App` and save the masks of the YbCR, HSV and L*a*b color spaces, then run the code in A.3, where the details of how to choose a representative fiber, are explained.
Table 3 shows parameters chosen to segment the image in the various color spaces. C_i denotes the i-th parameter channel in the corresponding color space, the corresponding code is given in A.3.

Table 3: Parameters chosen to detect green fibers

Color Space	C1 Min	C1 Max	C2 Min	C2 Max	C3 Min	C3 Max
HSV	0.278	0.533	0.102	0.252	0.906	0.992
L*a*b	77.764	100.000	-19.090	-7.541	-3.336	2.089
YCbCr	205.000	238.000	127.000	132.000	100.000	121.000

The results are shown in figure 22 and 23 and are encouraging. Every green fiber in a set of images was detected and confirmed by a human analyst. As can be seen the illumination in the images varies, as well as the focus plane and the degree of contamination by dirt and enclosed air. Nonetheless the algorithm detected major parts of the fibers based on a sample taken such as in A.3.

Figure 22: The images to the left show the image sections detected by the algorithm with their corresponding binary masks of the sought fibers.

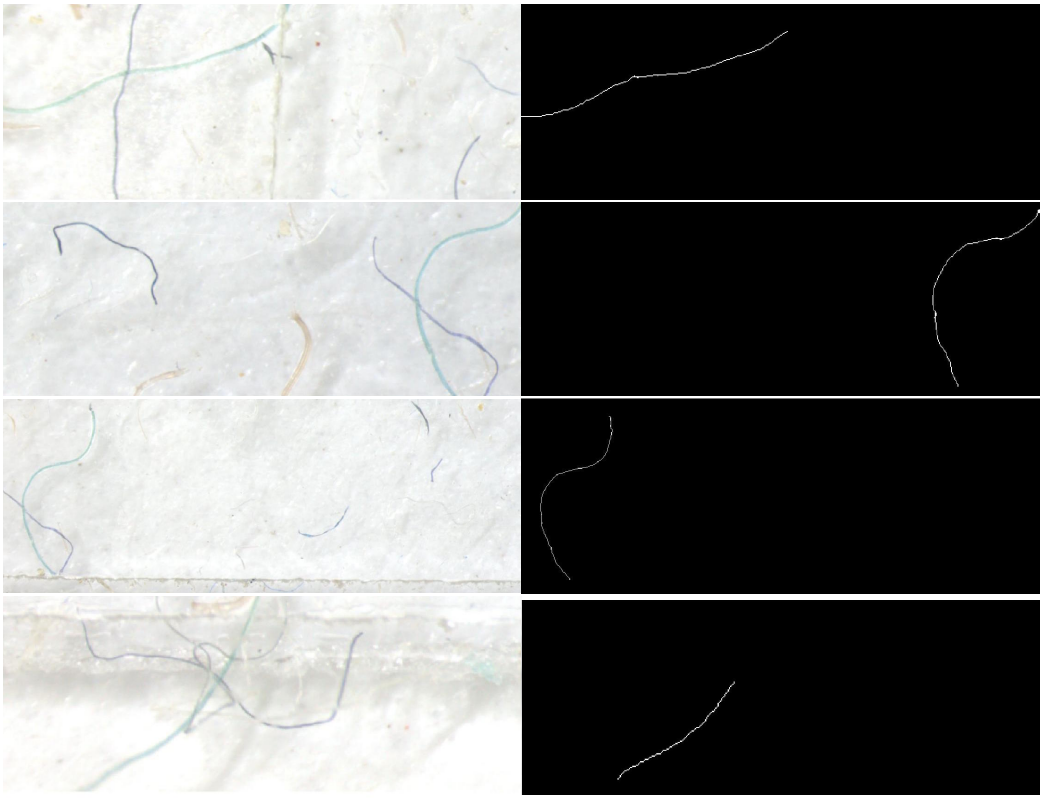

Figure 23: The images to the left show the image sections detected by the algorithm with their corresponding binary masks of the sought fibers.

3.3 Dark Background

One major issue not yet entirely resolved is that using a white background to scan the sample tapes conceals white or very light colored fibers. In figure 24 two images are shown which correspond to an overlapping section of the full tape sample. For orientation purposes the green arrows mark two ocher fibers which can be found on both images. The red arrow marks the position of a white fiber visible in the image using a dark background which is not possible to detect in the image using a white background. This poses a big issue because it is obviously not reasonable to ignore light colored fibers. However the image using a dark background is so noisy by dirt as well as air bubbles in the glue, that the image processing steps as described so far are

not applicable.

Figure 24: Both images show a corresponding sections of the same adhesive tape. The green arrows mark two distinct fibers present on both images for orientation, while the red arrow marks a fiber which is visible on a black background but not on the image using a white background

This seems to be a big drawback on the first glance, because by using a regular optical microscope and the image processing methods explored it will be impossible to find all important fiber types.
However, when using WITec's Alpha300 R series Raman microscope for Raman imaging, as presented in chapter 4, the user has the possibility to exploit an internal optical microscope to chose an area for further scanning. The images obtained by this function show all visible fibers in the pictures with both backgrounds.
A comparison is illustrated in figure 25. The red arrow marks the position of a white fiber visible with the dark background and the image acquired by the Raman setup, but not in the regular optical microscope using a light background.

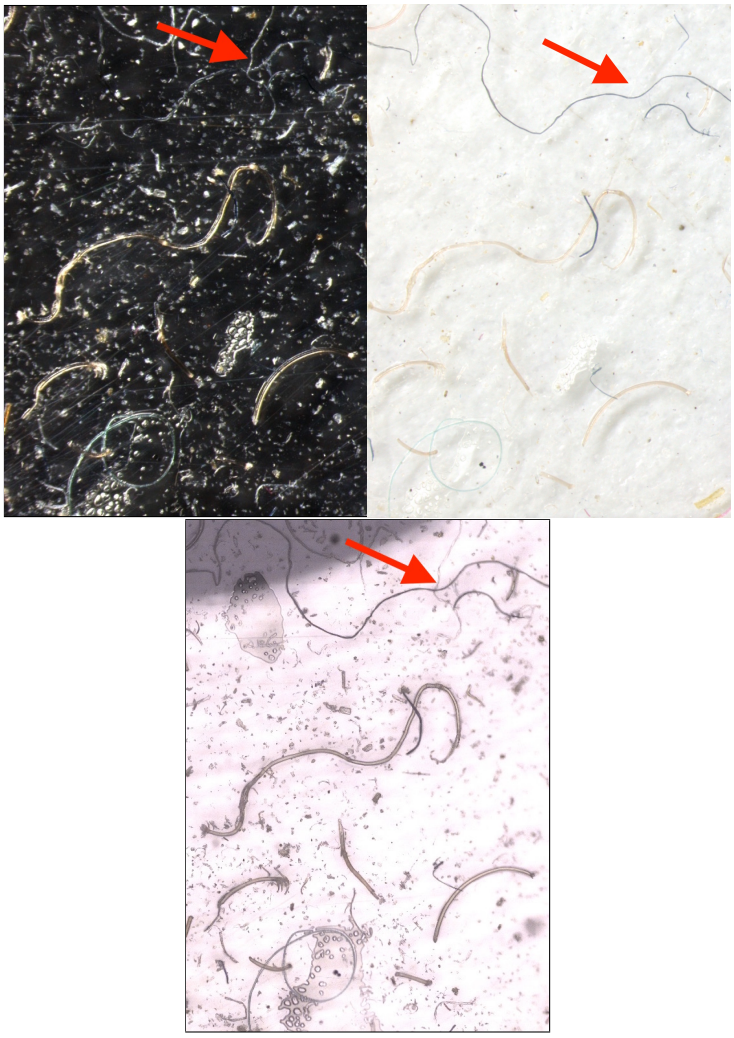

Figure 25: All three images show the same section of a sample adhesive tape. The third image was sampled by WITec's Alpha300 R Raman microscope used for choosing scanning locations. The red arrow marks a white fiber visible in the image with dark background, but not in the image obtained by the same microscope with a light background. It is also present in the image acquired by WITec's optical shot.

On the downside the functioning of the Raman microscope does not allow colored representation of the image as of now, so it is difficult to search an area for a specifically colored fiber. However combined with images from a regular optical microscope as used in the preceding chapters, it could be possible in the future to locate all fibers according to their color.

4 Part II: Raman Measurements

Raman spectroscopy is a popular scattering technique whose range of applications stretches from identifying minerals to analyzing historic paintings and drug components.
Raman scattering refers to inelastic scattering of photons by atoms or molecules. Due to the inelastic interaction energy is transferred and the emitted scattered light has a higher or lower frequency than the incoming light source. This is characteristic for the specific scattering atom or molecule. However the cross section of the frequency-shifted light is lower than the light resulting from the elastic scattering, called *Rayleigh scattering*, by a factor of 10^3 or 10^4. In the scattering process the exciting photons interact with the molecules in a non-resonant way. Only less than one in a million exciting photons induce one Raman photon, even less in case of confocal Raman spectroscopy. It is possible to analyze individual particles or layers with dimensions down to 1 μm and below.
The specifics and perks of the technique are described in detail in [24], in this thesis only a short recapitulation of the principles is given.

4.1 Confocal Properties

Raman spectroscopy operates on the principles of confocal microscopy, which uses a point-like light source, such as a laser, which is focused onto the sample. The corresponding image is collected through a pinhole in front of the detector located in the image plane of the microscope, thereby being confocal with the illuminating spot. Scattered light from above and below the focal point is prevented from being added to the image because the detected light is restricted to a small area around it. The wavelength λ determines the spatial extension of the focus as well as the image quality. The lateral solution could be increased (up to a factor of $\sqrt{2}$) but the increase claims the loss of 95% of the light due to the miniaturization of the pinhole. However, confocal microscopy became a favorable option in the course of the last century due to

its depth resolution and suppression of stray light. By using this technique rays from a different plane than the focal plane are prohibited to enter the pinhole which increases the image contrast significantly.

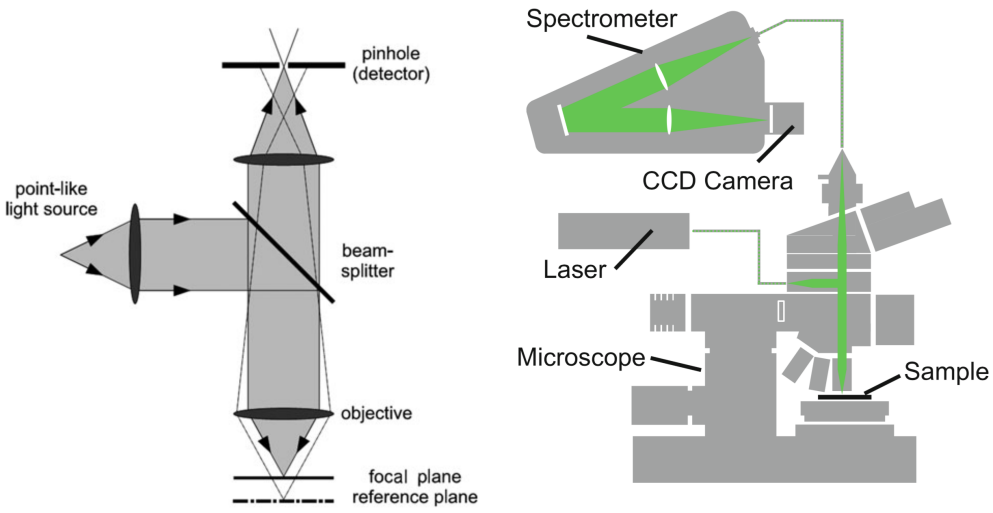

(a) Confocal Setup

(b) Raman microscope

Figure 26: Typical setup of a confocal system and a Raman microscope using a fiber-coupled laser source and a spectrometer. Source: [24]

Figure 26 shows the principles of confocal microscopy and a typical setup of a Raman microscope. It consists of an excitation laser, a microscope and a spectrometer with a CCD (charge-coupled detector). A piezo-scanner is responsible for the fast and accurate scanning-movement of the sample.

4.2 Image Formation

Following the calculations in [24], electromagnetic scattering in optical systems can be described by electrical and magnetic fields of the following form:

$$
\begin{aligned}
e_x(u,v) &= -iA(I_0 + I_2\cos(2\phi_P)) \\
e_y(u,v) &= -iAI_2\sin(2\phi_P) \\
e_z(u,v) &= -2AI_1\cos(\phi_P) \\
\\
h_x(u,v) &= -iAI_2\sin(2\phi_P) \\
h_y(u,v) &= -iA(I_0 - I_2\cos(2\phi_P)) \\
h_z(u,v) &= -2AI_1\sin(\phi_P)
\end{aligned}
$$

ϕ_P is an angle resulting from the coordinate transformation from the original coordinate system to the so-called optical coordinates u and v. Parameter A is a constant which puts the amplitude of the incoming light into relation with the focal length. I_0, I_1 and I_2 are integrals defined over the approximation for the solution of the electrical field in the plane of the aperture. However, when dealing with small aperture angles, I_1 and I_2 can be assumed as zero and the equations simplify to:

$$
\begin{aligned}
e_x = h_y &= -iAI_0 \\
e_y = e_z = h_x = h_z &= 0
\end{aligned}
$$

Now I_0 can be written as $I_0(u,v) = \alpha^2 \exp\left(\frac{iu}{\alpha^2}\right) h(u,v)$ with
$h(u,v) = 2\int_0^1 \rho J_0(\rho v) \exp(\frac{1}{2} iu\rho^2) d\rho$, where α is the aperture angle and J_0 is the Bessel function of order zero.
$h(u,v)$ is a three dimensional point spread function, short PSF, which corresponds to an image of an infinitely small point. The PSF is determined by the objective used in the microscope setup, but since the theory is derived for infinitely small points, the actual behavior of the function differs for larger aperture angles. Now let h_1 be the excitation PSF and h_2 the detection PSF, then the intensity distribution of the resulting image in a confocal Raman microscope can be written as:

$$I = \left| h_1(u,v) h_2\left(\frac{u}{\beta}, \frac{v}{\beta}\right) \right|^2 \otimes f(x,y,z)$$

where $\beta = \frac{\lambda_1}{\lambda_2}$, referring to the excitation wavelength λ_1 and the Raman wavelength λ_2 and f to the Raman generation. Note that the Raman wavelength in general does not refer to a single wavelength, but rather a distribution of wavelength around one certain wavelength, which yields in additional inaccuracy if neglected.

The Raman emission wavelength is shifted by a factor depending on the excitation wavelengths, which is described by the parameter β as the ratio of the wavelengths. Increase of this shift ($\beta > 1$) decreases the resolution. For an excitation wavelength of 532nm, β is supposed to be between 1 and 1.25, while for $\lambda = 785$nm, β can be up to 1.4. The pinhole is usually about 10-100μm in size and its lateral position must be adjusted. The lateral image size is $\Delta B = \Delta G \cdot M$ where ΔG is the object size and M the magnification of the objective.
The following inequality needs to hold during experiments:

$$\frac{M}{NA} \geq \frac{\pi d_0}{vp_{max}\lambda}$$

Here M again stands for the magnification, d_0 for the diameter of the pinhole, NA for the numerical aperture of the objective and vp_{max} is the maximum

size of the pinhole in optical coordinates (specifically $vp_{max} = 2.5$). Based thereon the following tables from [24] are calculated:

Table 4: M/NA for different objectives

Objective	10/0.25	20/0.4	40/0.6	60/0.8	100/0.9	100/1.25	100/1.4
M/NA	53	50	67	75	111	80	71

Table 5: $\frac{\pi d_0}{2.5\lambda}$ for typical wavelengths and pinhole sizes

Wavelength [nm]	440	448	532	633	785
$d_0 = 10\mu$m	29	26	24	20	16
$d_0 = 25\mu$m	71	64	59	50	40
$d_0 = 50\mu$m	142	129	118	99	80
$d_0 = 100\mu$m	286	258	236	199	160
$d_0 = 200\mu$m	571	515	472	397	320

Following these tables, experiments have to be designed in a way to provide a reasonable trade-off between resolution and efficiency.

4.3 Frequency Dependence

Light scattering is a result of an oscillating electromagnetic field interacting with a molecular system. By disturbing the electronic charge distribution in the molecule, a dipole moment is induced. All induced dipole moments summed up give rise to a secondary electric field representing the scattered light. The molecular dipole induced by an external electric field E is given by $\mu = \alpha E$, where α corresponds to the polarizability.

After Taylor expansion and harmonic approximation μ can be derived by:

$$\mu(t) = \alpha_0 \cdot E_0 \cdot \cos(\omega_0 t) + \frac{1}{2}\left(\frac{\partial \alpha}{\partial q}\right)_{q_0} \cdot q_0 \cdot E_0 \cdot \cos\left[(\omega_0 - \omega_q)t\right] + \frac{1}{2}\left(\frac{\partial \alpha}{\partial q}\right)_{q_0} \cdot q_0 \cdot E_0 \cdot \cos\left[(\omega_0 + \omega_q)t\right]$$

E_0 is the amplitude of the external electrical field, ω_0 is its oscillation frequency, α is the molecular polarizability which is a factor putting the external field in relation to the induced dipole moment. Oscillations with characteristic frequencies ω_q along each normal coordinate q can be excited and described by $q = q_0 \cdot \cos(\omega_q t)$. This time-dependent induced dipole moment acts as a secondary source of radiation, hence the light scattering, and consists of three specific terms of frequency:

- $\alpha_0 \cdot E_0 \cdot \cos(\omega_0 t)$ is called elastic Rayleigh scattering and oscillates at the same frequency as the incident radiation, thus corresponds to the light scattered at this frequency and does not carry information about the nuclear molecular degrees of freedom.
- $\frac{1}{2}\left(\frac{\partial\alpha}{\partial q}\right)_{q_0} \cdot q_0 \cdot E_0 \cdot \cos\left[(\omega_0 - \omega_q)t\right]$ is the source of the Stokes scattering that is presented as the Raman spectrum and oscillates at the frequency which is the difference between the laser and the normal mode.
- $\frac{1}{2}\left(\frac{\partial\alpha}{\partial q}\right)_{q_0} \cdot q_0 \cdot E_0 \cdot \cos\left[(\omega_0 + \omega_q)t\right]$ describes anti-Stokes scattering, which is the same as the Stokes spectrum, but with strongly reduced intensity. It is blue shifted with respect to the laser frequency, while the radiation emitted by the second term is red shifted with respect to the excitation frequency.

As described in [24], the gradient of the polarizability $\left(\frac{\partial\alpha}{\partial q}\right)_{q_0}$ corresponds to the Raman scattering intensity.
The parameters $\left(\frac{\partial\alpha}{\partial q}\right)_{q_0}$ and ω_q are thereby carrying molecular information about the system and ω_0 and E_0 refer to experimental parameters. Further enhancement of Raman scattering is based on the instance that the inelastically scattered intensity is proportional to the overall power emitted by the induced dipole moment, as elaborated in depth in [24]:

$$I_{Stokes} \propto \left(\frac{\partial\alpha}{\partial q}\right)^2_{q_0} \cdot (\omega_0 - \omega_q)^4 \cdot E_0^2$$

The square of the polarizability accounts for the resonance Raman (RR) scattering and the square of the electrical field for the surface enhanced Raman

scattering. Raman Scattering involves an excited electronic state which gives information about the molecular structure and by examining the intensity of resonantly enhanced modes in dependence of the excitation wavelength, it is possible to gain insight on the strength of the interactions between the excited electronic state and the vibrational modes, thereby revealing the change in bond length and angles during the transition from ground to excited state.

4.4 Experimental Setting

The intensity of the Raman scattering is proportional to the fourth power of the frequency of the exciting laser radiation. Hence the Raman signal is 16 times higher at an excitation at 400nm instead of 800nm. However the effects of fluorescence have to be considered which often appear when the sample is excited in the UV region and are less likely to be encountered in the near-infrared regions of the spectrum. The lateral resolution is given by the shortest distance between two separately distinguishable points which is calculated by $0.61 \cdot \frac{\lambda}{NA}$, NA being the numerical aperture. Hence the shorter the excitation wavelength is, the higher is the resolution. It is important to choose an appropriate laser wavelength for a particular experiment. Raman scattering is high for UV wavelengths below 350nm, but there are not many objectives available and their NA is very small. Using higher wavelengths reduces the lateral resolution, as well as the Raman efficiency, but on the positive side, the fluorescence drops.
Obviously the choice of wavelength needs to be adapted for the particular application, but what can generally be said, is the laser beam has to have Gaussian shape and should be linearly polarized. Furthermore its bandwidth should be less than 1cm^{-1} and it is required to be very stable in frequency and intensity. As previously mentioned the Raman signal and the excitation power are in a proportional relationship, however the laser power should be chosen low enough to prevent absorption that leads to thermal decomposition of the sample. Depending on the wavelength and the sample properties, it

may vary in a range of microwatts to hundreds of milliwatts. To optimize the collection efficiency as well as the spatial resolution possible for the particular sample the objective providing the highest possible numerical aperture should be chosen, while considering the transmission characteristics of the objective at the chosen wavelength. The transmission may vary greatly at different wavelengths due to the fact that anti-reflection coatings have less than 0.5% reflectivity in the visible range while being far more reflective in the IR range. Since the NA is to be chosen as high as possible, the height of the sample needs to be considered, because a high NA corresponds to a good depth resolution, thereby targeting a very small height in Z direction only.

Just as important as the influencing factors mentioned so far is the throughput of the microscope itself. The losses are squared since the light needs to pass through the setup twice. This includes the choice of the beam splitter (dichroic or holographical) which at best has a reflectivity close to 100%.
Also the coupling between microscope and spectrometer and the pinhole size needs to be considered. The optimal pinhole size depends on the PSF and its diameter on the image side of the objective. E.g. choosing an objective of 100× magnification and a numerical aperture of 0.9 at the excitation wavelength of 633nm, the diffraction-limited airy disc in the image plane will be 43μm, hence a pinhole diameter of 50μm will be suitable, see tables 4 and 5 or [24] for more detail.
Another important component in the Raman microscope setup is the choice of the detector. There are many options available in choosing a charge-coupled detector (CCD). It is composed of a set of light sensitive photodiodes made of silicon which are connected to a capacitor. Every registered photon causes an electron to be stored in the capacitor. The percentage of detected photons in relation to the total incoming photons can be described by the so-called quantum efficiency and may be enhanced by using back-illuminated detectors.

4.5 Raman Mapping

It is possible to use a stepper motor to move the sample and raster scan it by taking a measurement at each position and thereby collecting multiple spectra. This technique is often called 'Raman mapping' and can produce chemical distribution maps with a lateral resolution of a few micrometers. However depending on the signal-to-noise ratio (SNR) and the scattering efficiency of the sample this can take a very long time. Due to the weak Raman signal the acquisition of the spectrum can take several seconds integration time. Even if only 1 second integration time is used on a sample of 60×60 pixels the experiment will take one hour for integration.

4.6 Advantages of Raman Spectroscopy

Confocal Raman imaging has applications in a broad range of scientific fields due to its ability to fully characterize a material's composition. Concentrations as low as 10^{-3} to 10^{-5}M of substances can be detected by electronic resonance enhancement and thereby increase of the intensity of the scattered light by a factor of 10^6 which improves the SNR. There are extensive databases available for fast identification of unknown materials. The confocality reduces the influence of unwanted fluorescence and the technique is subtle to chemical effects, such as crystallinity, polymorphism, phase, intrinsic stress/strain, protein folding and hydrogen bonding. Furthermore it is very popular due to its molecular sensitivity and is still a suitable option in presence of water, see [24].
Another advantage is that the sample needs no further preparation, thereby making it a suitable technique to analyze historic pigments or forensic evidence. A confocal Raman microscope may provide full 3D spatial solution which in turn permits the study of discrete volume in a transparent sample. This is of use in the analysis of polymer laminates, inclusions in glass and minerals or materials in glass or plastic containers.

4.7 Stokes Shift

Since the total energy of a system needs to remain the same, the inelastically scattered photon is shifted to a lower frequency in case of the vibrational state of a molecule being more energetic than its initial state. Commonly this frequency shift is referred to as a Stokes shift. Of course the photon needs to be shifted to a higher frequency if the vibrational state is less energetic than the initial one. That case is addressed as an anti-Stokes shift. While Rayleigh scattering is an elastic kind, Raman scattering can be described as inelastic scattering, because the energy differs between the initial and scattered photons after the interaction. Infrared absorption on the other hand operates in a way that the energy of a single absorbed photon makes up the difference in energy between those two states.

These shifts are usually given in wavenumbers, which are units corresponding to the inverse of length given by cm^{-1}, and are directly related to energy. In order to convert between spectral wavelength and wavenumbers of shift in the Raman spectrum, the following formula can be used:

$$\Delta w = (\frac{1}{\lambda_0} - \frac{1}{\lambda_1})$$

where Δw is the Raman shift expressed in wavenumber, λ_0 is the excitation wavelength, and λ_1 is the Raman spectrum wavelength. Often the unit of preference is nanometers, hence be expressed in the following way:

$$\Delta w(\mathrm{cm}^{-1}) = \left(\frac{1}{\lambda_0(\mathrm{nm})} - \frac{1}{\lambda_1(\mathrm{nm})}\right) . \frac{(10^7\mathrm{nm})}{(\mathrm{cm})}$$

Raman scattering should not be confused with fluorescence emission, where a molecule in an excited electronic state emits a photon before returning to the initial state. The Raman spectra yields as the Raman scattering intensity as a function of the Stokes and anti-Stokes frequency shifts.

4.8 Problems provoked by Fluorescence

The greatest problem with Raman spectroscopy is fluorescence, due to its resonant interaction of light with the electronic samples states. Background fluorescence is encountered very often when analyzing organic molecules. In resonance Raman scattering fluorescence and luminescence are observed, but the cross-section for fluorescence is about six orders of magnitude larger than that of the RR. Therefore the presence of fluorescence impedes the observation of Stokes scattering light.
When using excitation wavelengths in the deep UV, which corresponds to wavelengths < 250nm, fluorescence is energetically far enough away from scattered light to not interfere with the Raman signal. However, if the resonance Raman spectroscopy coincides with the origin of the fluorescence emission, the featureless fluorescence spectra occlude the Raman signals. In fact the intensity of fluorescence is so high that no Raman signal can be detected.
This is the case when the Stokes shift, hence the difference in energy between the absorption and fluorescence maximum, is small. Additionally the strong absorption of the excitation light poses a problem in experimental setup because it causes thermal decomposition and unwanted photoreactions of the sample. Figure 27 illustrates this issue.

It is inevitable to reduce the fluorescence background as much as possible, which sometimes can be achieved by using an appropriate excitation wavelength at which the sample does not show the effects of fluorescence as intensively. The use of confocal Raman instruments reduces the fluorescence to the photons emitted from the focal plane of the sample only, which is acceptable in many cases to obtain a reasonable image. Especially if the fluorescence is caused by impurities, it will be bleached in the focal plane by the high intensity of the excitation.

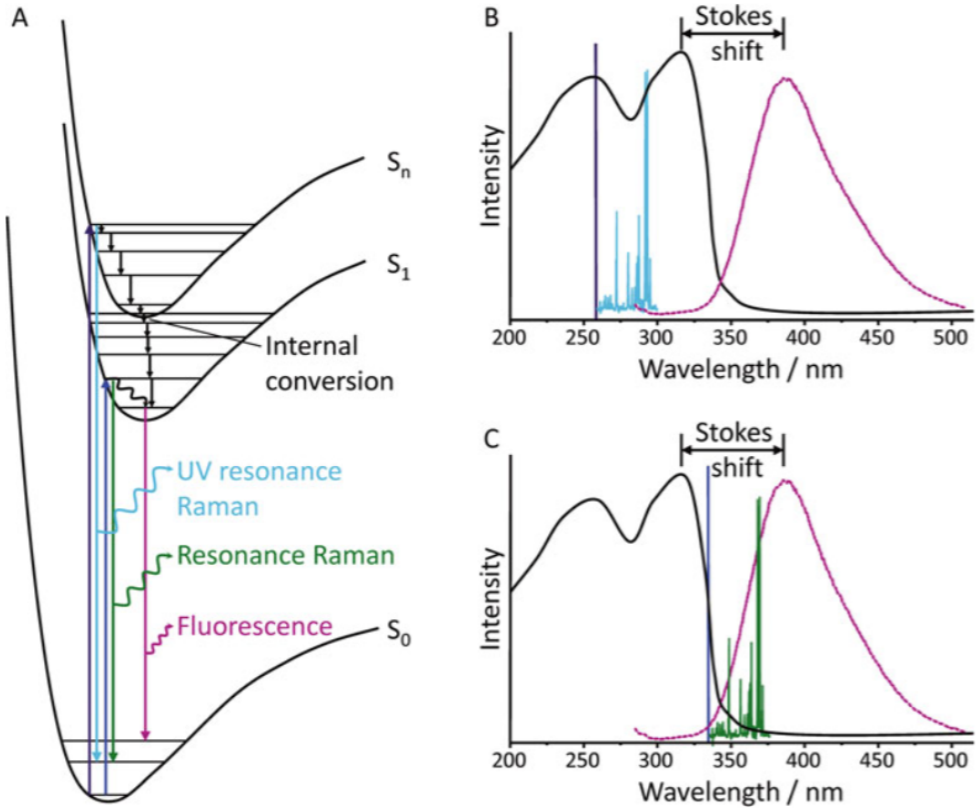

Figure 27: A.) Energy level diagram showing the excitation in dark blue, the Raman scattering in light blue and green and the fluorescence in pink. B.) Excitation to higher electronic states which causes no interference between Fluorescence and Raman signals. C.) Excitation at the high-wavelength edge of the absorption band which causes the two signals to overlap. Source: [24]

In recent studies such as [25], 1064nm systems have been evaluated and compared to the common 785nm. Background fluorescence excited by 1064nm was about 500 times weaker than when excited at 785nm. Furthermore, the background was more stable in 1064nm such that background reduction with photobleaching was minimal, thereby showing promising results in dealing with the background fluorescence, but as described already the high wavelength also comes with a price.

4.8.1 WITec Raman Microscope

For the following experiments a confocal Raman microscope from WITec's[2] ALPHA300 R series was used. It allows hyperspectral image generation by Raman mapping with the information of a complete Raman spectrum at each pixel. The diffraction limited lateral resolution lies at about 200-300nm and is usable for 3D image generation. Optionally integration time may be lowered to 0.76 milliseconds per spectrum and does not require sample preparation.

[2]WITec Wissenschaftliche Instrumente und Technologie GmbH, Lise-Meitner-Str. 6, D-89081 Ulm, Germany

5 Data Analysis

5.1 Imagelab

For the analysis of the Raman data *ImageLab*[3] was used. It is a Microsoft Windows based multisensor imaging tool which can be used for hyperspectral image analysis and processing. It features a graphical user interface to allow straightforward and intuitive handling of imaging techniques applicable for UV/Vis, infrared, Raman, THz, optical emission/absorption, and mass spectrometry. It provides the possibility to merge hyperspectral images of chemical signals as well as high resolution photos. Furthermore it enables the user to perform multivariate statistics on the imported data, such as multilinear regression, principal component analysis, hierarchical cluster analysis, partial least squares analysis and random forests. For further information check the software's website or [26].

5.2 Generation of Classifiers

5.2.1 Baseline Correction

In many cases it is necessary to perform a baseline correction to find an appropriate representation of the characteristic peaks in the signal. If the baseline shift is independent of the wavenumber it can simply be subtracted from all intensity values. However it often shows complex universal patterns which are not intrinsic to the signal itself, requiring improved spectral background subtraction.
In most baseline problems a smooth baseline is subtracted from the signal carrying the actual information about the examined sample, as described in [27].
Common possibilities to tackle the issue are to either subtract a fitted polynomial or spline curve, or to use digital filters, Fourier transform techniques,

[3] http://www.imagelab.at accessed on 09-01-2017

peak clipping algorithms or wavelet transforms, see [28]. In [27] an alternative approach is presented which provides a successful baseline estimation for the general approach, called the *Eiler algorithm*. It is based on asymmetric least squares which weighs positive deviations with respect to the baseline less than negative ones. Additionally it uses a Whittaker smoother, explained in [29]. For baseline corrections shown in section B.1 the Eiler algorithm was used with a smoothness factor of 10000 and an assymmetry parameter of 0.001 with little variation depending on the individual signal.

5.2.2 Curse of Dimensionality

The curse of dimensionality refers to phenomena in classification which appear in high dimensional spaces. Due to the increase in dimensionality the volume of space increases at such a high rate that the data becomes sparsely distributed and local classifiers such as K-nearest neighbors become computationally too expensive.
Assuming a p dimensional unit sphere and n data points uniformly distributed around its origin, then the points are moved closer to the edges of the sphere the larger p becomes.
Figure 28 is extracted from [30], where the issue is discussed in detail. It shows a unit cube with a subcube inside. This subcube can formally be described by taking a hypercubical neighborhood of a fixed point. This neighborhood captures a fraction r of all observations. This correlates with a fraction r of the total volume of the unit cube. Since the expected length of the edge needed for this subcube is $e_p(r) = r^{\frac{1}{p}}$, we get an edge length of $e_p(r) = 0.79$ for $p = 10$ and $r = 0.1$. This means that almost 80% of all variables must be covered to explain only 10% of the total data.
The right part of figure 28 shows the necessary side length of such a neighborhood in dependence of the fraction of volume it is supposed to capture.

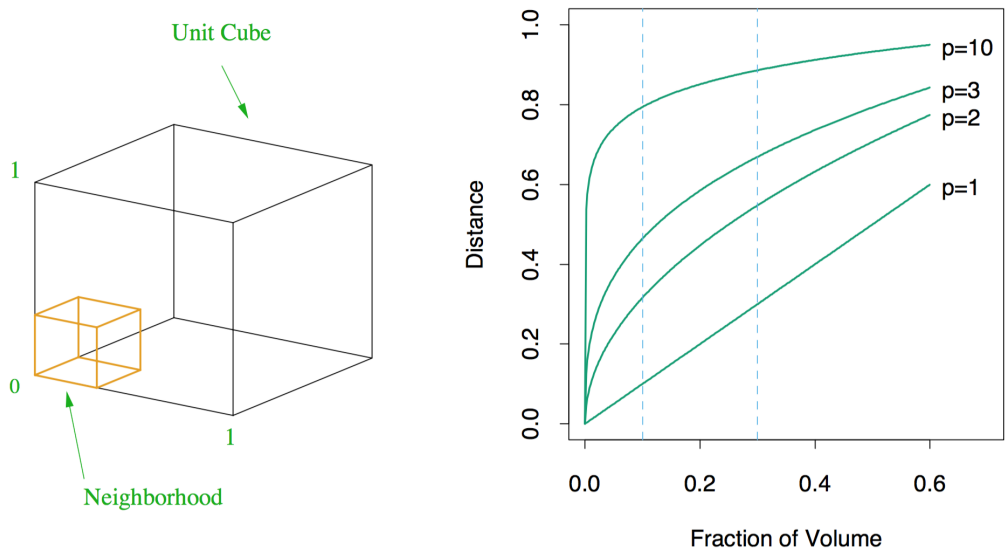

Figure 28: . Source: [30]

This phenomenon leads to a sparse feature space. In [26] it is explained that the acquisition of spectra with 300 intensities at a specific wavelength, the feature space contains 10^{600} cells if the intensity is measured in a 1% resolution. For a 200×200px sized image we obtain 40000 samples which is not nearly enough to describe a reasonable fraction of the feature space considering figure 28. Consequently it is essential to reduce the feature space to a smaller number of descriptors carrying relevant information about the data. This can be done by transforming the feature space, e.g. by performing a principal component analysis, or in case of spectral data by introducing spectral descriptors such as in [26].

5.2.3 Spectral Descriptors

ImageLab uses a variety of spectral descriptors to extract information from the data. They can describe raw data intensities, or can refer to the sum of intensities in a certain bandwidth, or consist of the evaluation of mathematical functions using spectral data . The full list of available predefined spectral descriptors is available on *Imagelab*'s website `http://www.imagelab.`

at/help/spectral_descriptors.htm.

The biggest advantage of using spectral descriptors rather than raw intensities lies in the better performance of classifiers in high dimensional space, but also in the improvement of the information structure of the data, see [26]. Thereby the use of spectral descriptors helps to avoid the curse of dimensionality which is a constant threat in hyperspectral imaging due to the large feature set resulting of the high spectral resolution of the image.

5.3 Definition of Training and Test Datasets

Prior to formulating a model describing the relationships of data points, one must define a training and a test set. The training set is used to extract classifiers out of the data, while the test set is used to assess the quality of the prediction. As a common rule the training set should be a random subsample of the full data set, about 50 % of its size. Importantly the test set must not contain any data points present in the training set.

5.4 Random Forests

The list of possible classification algorithms is long. Random forests are ensemble methods that have proven themselves as highly valuable and successful in the recent past. There is a large amount of implemented software, e.g. packages implemented in R at CRAN's website[4] or see [31] . Many studies and books, such as [30] and [32] report on the practical traits of the method. They require very little tuning and are easy to interpret.
The principle of their functionality is as follows: Multiple decision trees, each using a random subset of all features are trained during the training period. For a new data set not belonging to the training set, the mode of all classification results from these decision trees is calculated and used as an overall classification result. Single decision trees tend to overfit, but by averaging

[4]https://cran.r-project.org/web/packages/randomForest/index.html, Accessed:26-12-2016

over a large number of trees this behavior can be erased. Choosing a random subset of features for each decision tree prohibits the trees from becoming correlated. This is the case in other bagging algorithms: often a small subset of features turns out to predict the target valuable very well, so the trees tend to choose these features more often and thereby become correlated to each other.

The principle of random forests is visualized in figure 29. Part A in the figure shows the training process of the classification. Multiple subsamples of the training set containing a ground truth are randomly chosen. For each subset a decision tree is trained.
Part B shows the prediction step: a new sample data is classified by the total set of decision trees trained previously and their majority vote is taken as the classification result of the total random forest.

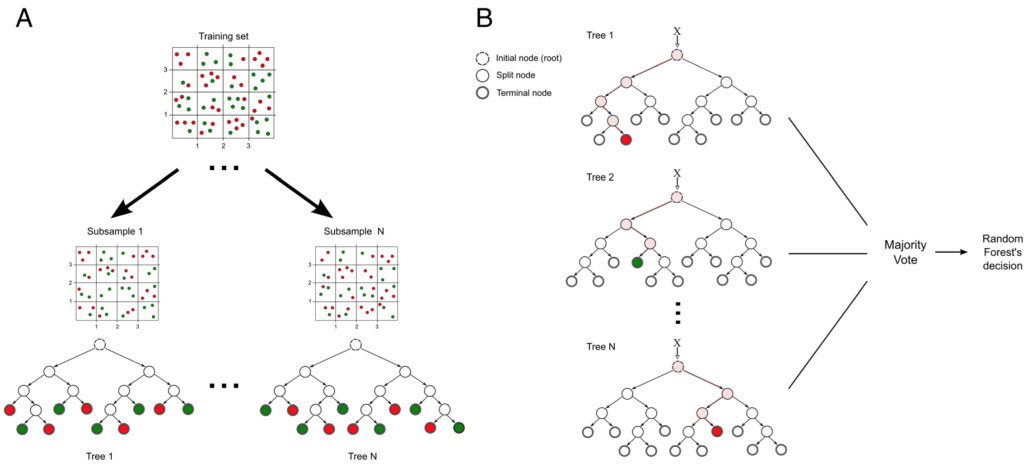

Figure 29: A.) Each decision tree selects a random sample with replacement of the training set as well as a random subset of features to fit the tree. The original training set provides labels as a ground truth to the data, here marked in red and green. B.) For a new data point each tree comes to a decision based on its previous training. The majority of outcomes will decide the overall classification of this new data point. Source: [33]

6 Results

6.1 Image Processing Results

The algorithm presented is able to fulfill two tasks: on the one hand it can segment a microscopic image successfully and return a binary mask showing all available fibers. This can be used in the future to move the sample in such a way that measurements are taken of all fibers collected during evidence acquisition. The practicability of this procedure is limited only by the amount of available digital storage, because acquiring hundreds or thousands of spectra belonging to fibers results in a huge amount of data.
On the other hand the algorithm uses the transformation in three different color spaces L*a*b, YCbCr and HSV to enable the user to choose suitable thresholds for the color specifications of a specific fiber. The algorithm returns all instances in a set of images that show similar characteristics. This can be used to automatically take measurements of all fibers that show desired color features such as the color of a reference fiber. In section 3.2 the algorithm's ability to detect green fibers is demonstrated.

6.2 Raman Spectral Results

The full list of spectral data collected from different fibers is given in appendix B.1. A part of them were able to be linked with reference spectra taken from literature. However in a significant number of experiments problems were encountered, either the sample was bleached or destroyed, or the signals showed fluorescence only and it was not possible to evaluate the origin of the fiber.

6.2.1 Fluorescence

Figure 30 shows the Raman spectra of two fibers examined during the studies. Both these spectra are raw data and have not been manipulated in any way.

The spectrum in 30a originates from a white cotton fiber and shows a nearly perfectly clear signal. The peak at the left results from the laser excitation and is commonly removed during baseline correction. Figure 30b on the other hand shows the spectrum of an ocher colored fiber. The very same peak caused by the laser is present in this spectrum too, but is so tiny compared to the rest of the signal, that it is barely visible without further processing. The intensities of this spectrum are more than one magnitude higher than in the spectrum of the white cotton fiber. Seeing how both these samples are obtained at the same laser power, the same excitation wavelength and for the same integration time, they are a good example to see the presence of fluorescence on the first glance. Considering how little the characteristic peaks in the white cotton spectrum are, namely less than 1000 counts, it becomes clear how difficult it is to find such a characteristic signal and entangle it from the signal resulting from fluorescence.

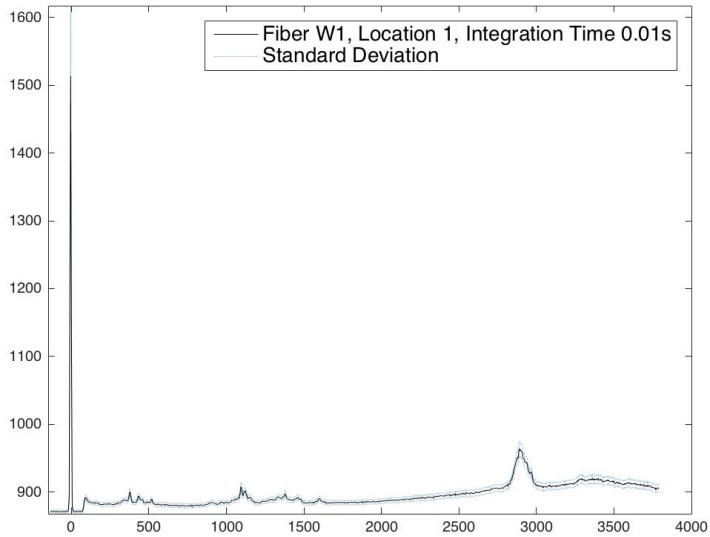

(a) Spectrum for W1 at location 1 obtained at 45mW and 0.084s.

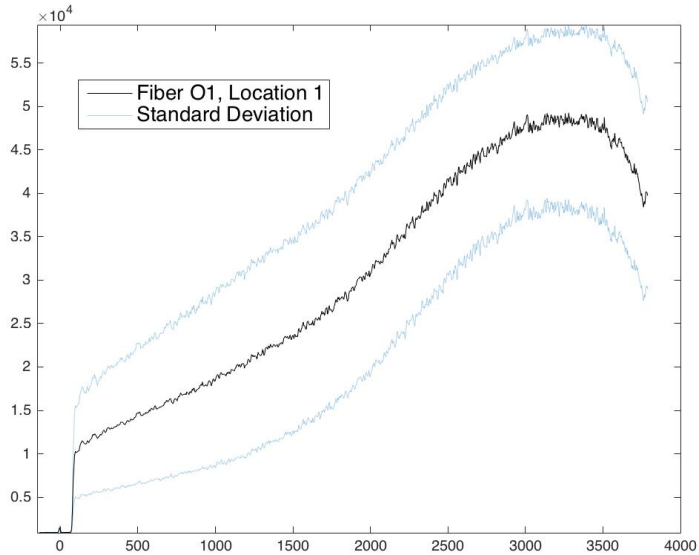

(b) Spectrum of O1 at location 1 obtained at 45mW, 0.084s

Figure 30

6.2.2 Indigo Dyed Fibers

Taking a closer look at the averaged and filtered spectra of the samples originating from fiber B1 one can find a significant peak at wavenumber 1587 present in all measurements taken along these fibers. This peak appears to be present in many spectra of fabrics dyed with indigo which is the reason for comparing the obtained spectra with references taken from [3]. The spectra have been digitized using *Datalab*[5] to allow comparison. Figure 34 shows averaged and filtered spectra of samples B1 at different locations and three different Jeans samples provided by [3]. All the spectra have clear peaks at around 1584-1587cm^{-1}, as well as 1700cm^{-1}. Also the peak at 1365cm^{-1} is present in the samples of B1. Furthermore B1 at location 1 shows a similar peak at around 750-760cm^{-1} as do the Jeans samples. Although the spectra of B1 differ from the indigo dyed cotton fibers, it does have a higher resemblance to the cotton than to the dyed polyester. Possibly the discrepancy between the cotton in the reference data and the spectra of B1 can be explained by the bleaching which occurred during the experiment.

Figure 32 compares an indigo solution dyed polyester fiber as well as an indigo dyed cotton fiber from [3] with the samples from B1. According to [3] indigo is applied as a vat dye on cotton. It is taken into the cellulose chains after the dye is soluble in water as a result of the dye's reduction. It forms large agglomerates of pigments subsequent to re-oxidation. The indigo dyed polyester fibers featured in figure 31 and 32 were solution dyed, which can result in a different degree of dispersion of the indigo dye.

[5] http://datalab.epina.at accessed on 10-01-2017

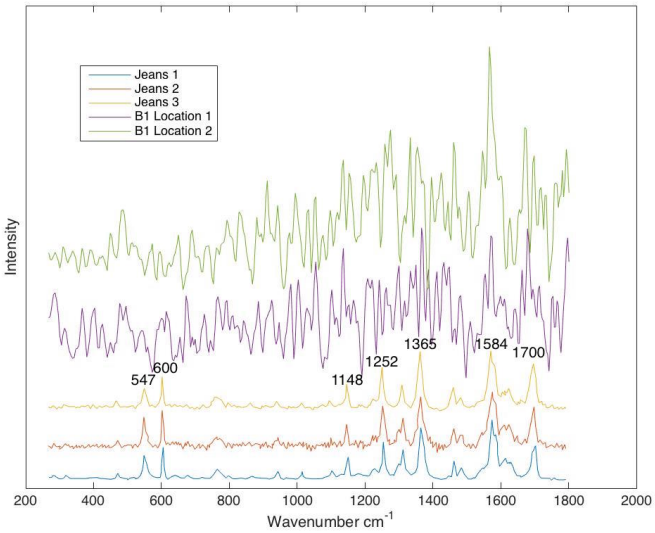

Figure 31: Raman spectra of the blue fiber B1 at two different locations as well as different cotton fibers from multiple blue jeans. Source for reference spectrum: [3]

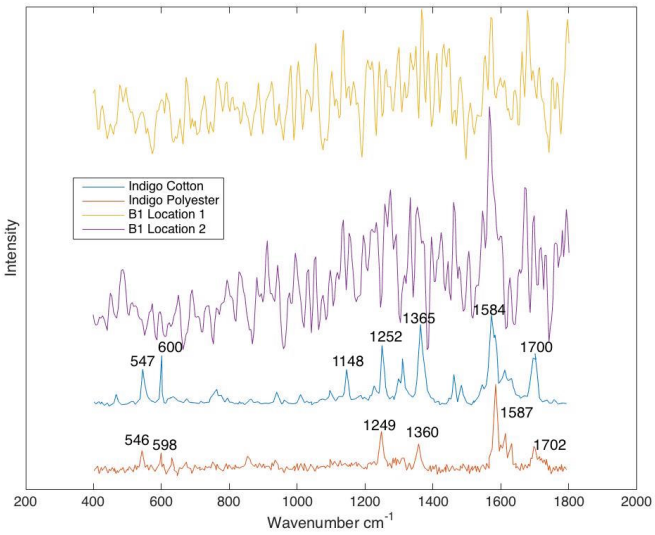

Figure 32: Raman spectra of the blue fiber B1 at two different locations as well as indigo on a cotton fiber from blue jeans, and blue portions of polyester fibers resulting from melting the fiber with indigo grains (Vat Blue 1). Source for reference spectrum: [3]

Figure 33 shows the combined plots of figure 31 and 32 for convenient comparison.

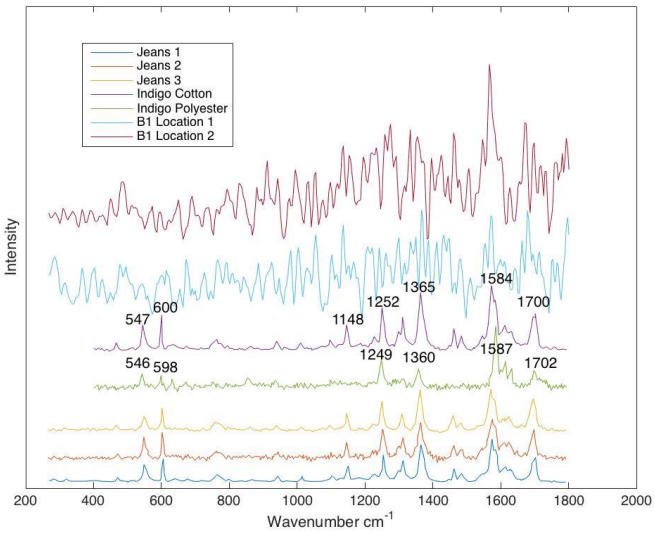

Figure 33: Raman spectra of figure 31 and 32 combined and compared to spectra of fiber B1

6.2.3 Ocher Colored Polyester Fibers

The spectrum of fiber O1 at location 2 has been compared with a reference spectrum of a polyester fiber taken from [3] which was digitized in *Datalab*. Both spectra show a very dominant peak at 1616cm^{-1} as well as at 1728cm^{-1} and 1293cm^{-1}, as shown in figure 34. The two spectra resemble each other overall very well.

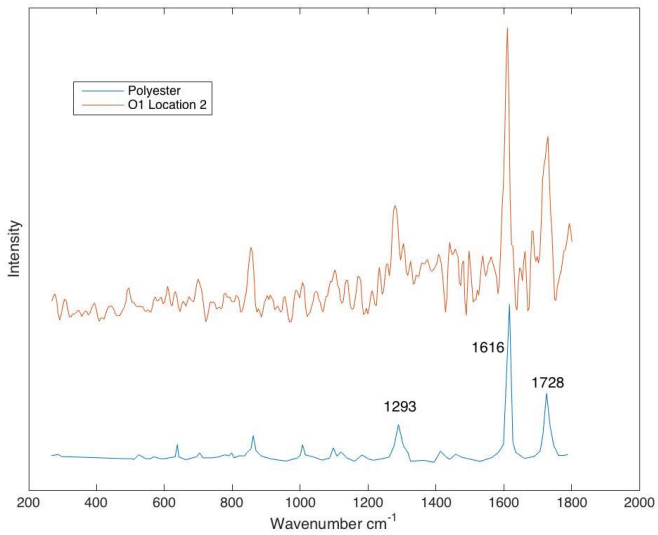

Figure 34: Raman spectra of the ocher colored fiber O1 as well as a polyester fiber. Source for reference spectrum: [3]

In figure 34 the spectrum of O1 resembled the spectrum of polyester in [3] very well. However when all spectra obtained from the ocher colored fibers O1 and O2 are compared only O1 at location 2 and sample O2 at location 1 give a clear signal comparable to the one of polyester, see figure 35. The signal can still be seen in sample O2 at the second location, but it is of poorer quality than the first two samples. The sample O2 at location 3 has been taken with 10mW whereas all the other samples were obtained by using 45mW which explains the weak signal. Sample O1 at location 2 was destructed, and so was sample O2 at location 2. Integration time for O1 location 1 was double the integration time of the others. Surprisingly this measurement gives the worst signal though no destruction on the fiber was visible. This can be explained by the fact that the fiber was not perfectly aligned in the focal plane. It demonstrates another problem occurring in automating the procedure of scanning the adhesive tapes by the Raman microscope. Even if the fiber can be located by the image processing algorithm presented earlier, and the sample stage can be moved accordingly, it is unclear how to automatically find a suitable focal plane to obtain a usable spectrum as of now.

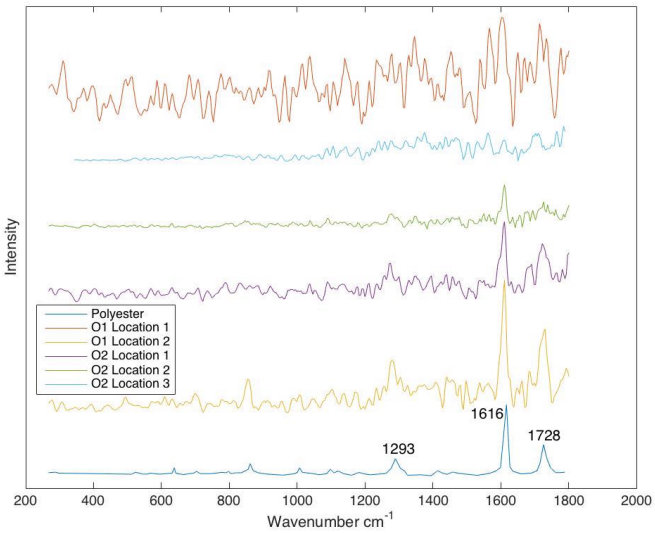

Figure 35: Raman spectra of the ocher colored fibers O1 and O2 on multiple locations as well as a polyester fiber. Source for reference spectrum: [3]

6.2.4 White Cotton Fibers

A cotton spectrum from [3] was taken for comparison of the averaged spectra obtained in sample W1, see figure 36. The two spectra resemble each other very well, both showing significant peaks at 380cm^{-1}, 436cm^{-1}, 1095cm^{-1} and 1379cm^{-1}.

Figure 37 shows the spectrum of W2 at location 2, as well as the spectrum of sample W1 and the reference from [3]. The signal is not nearly as good and as that of W1, but shows an overall tendency of the peaks present in cotton.

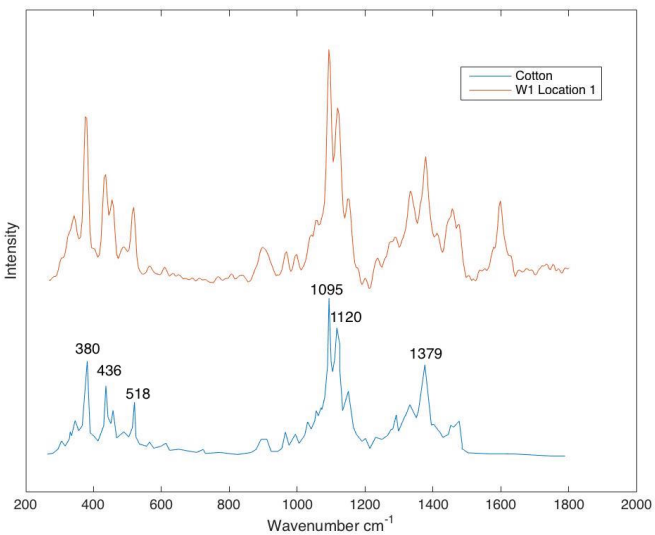

Figure 36: Raman spectra of the white fiber W1 as well as a cotton fiber. Source for reference spectrum: [3]

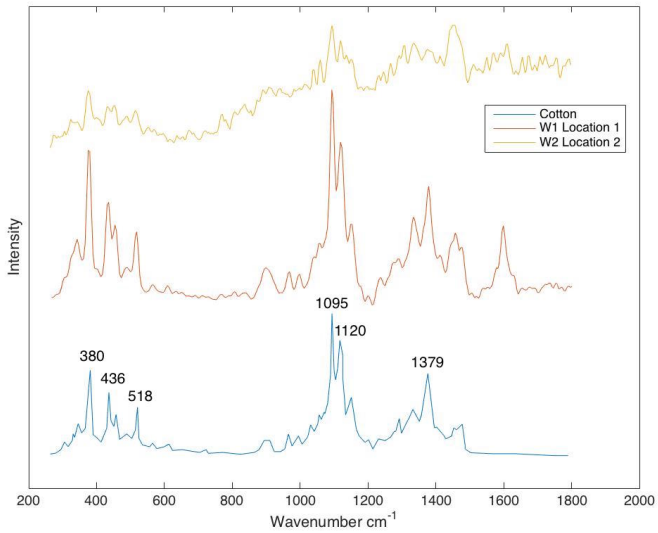

Figure 37: Raman spectra from white fibers W1 and W2 as well as a cotton fiber. Source for reference spectrum: [3]

7 Conclusions

7.1 Feasibility of the Method

Considering the general conditions of dealing with data collected at crime scenes and which is to be used as evidence in court, one must not make the mistake of being too enthusiastic about studies successfully using Raman microscopy to identify fibers by finding a way to extract spectra unique for one specific material from the Raman spectra dominated by fluorescence.

7.1.1 Complications during Experiments

The procedure of obtaining the evidence tapes in which the fibers were trapped was modified from the real handling of adhesive tape. For practical reasons during the experiments the tape has not been two-folded but stuck on a glass slide commonly used for microscopy. This framework is essential to provide reasonable outcome of the Raman measurements. However multiple noteworthy complications have been experienced:

- The microscopic glass slides are very thin to provide little interference with the measurements. In about a seventh of all cases the fragile cover slips broke, although the experiments were conducted in a closed laboratory environment with the possibility to take the samples without a rush or other complications which is often not the case in real life forensics. In another two samples dust and sand have caused so much contamination that the tape barely stuck onto the glass, which obviously discards the method in many cases as well.
- When dealing with cover slips it is necessary to wear gloves at all times. Using the conventional method it is not, because the two-folded tape can easily be cleaned with ethanol before its preparation preceding the microscopic examination.

- In some few cases the samples were highly contaminated with dust and dirt. They showed troubles with sticking on the cover slips properly, which is not acceptable in case of forensic evidence.

7.1.2 Fluorescence

Even if the complication by fluorescence can be tackled by using a higher laser wavelength and finely tuning the spectroscopy parameters, there are other factors making it impractical in forensics. Using a high laser wavelength requires the sample to be opened and the measurements to be performed on the uncovered fibers due to the weakness of the signal. In evidence handling this is considered unfeasible.

Multiple experiments have been conducted by removing the tape holding the fibers from the glass slide to use a laser wavelength of 785nm in the Raman setting in order to cope with the fluorescence. However in all these measurements the fiber was displaced as soon as it was hit by the laser, not allowing the collection of usable results. If a high excitation wavelength is used which requires opened samples, the fibers will have to be mounted and fixed in some other way.

7.1.3 Focal Plane

Another issue not addressed in this study is the fact that even though a fiber can possibly be automatically detected and the microscope stage controlled in a way such that the laser of the microscope is aligned with the fiber, it is crucial to adjust the focal plane correctly. Especially since fluorescence is expected during the measurements and the confocality is indispensable, it is essential to take the measurement in a suitable plane. In section 6.2.3 such a case is presented.

7.1.4 Image Processing

Independent of the less encouraging results during the Raman experiments, the algorithm presented in section 3 and appendix A shows promising results in image segmentation to recognize fibers in images. The possibility to provide a sample fiber and search through a set of images to look for fibers of similar color can save a lot of time and effort if introduced in a forensic laboratory. Additionally it can be used to learn about the composition of differently colored fiber types present in the sample, which might offer valuable clues to a case as well. However, it must be noted that the performance of the algorithm is limited in heavily contaminated samples. In the presence of blood in the sample the background, hence the glue of the adhesive tape, shows very different color characteristics and requires different processing.

A Algorithm Image Processing

A.1 Main Routine

The following code called `detectfibers.m` reads in an RGB image, as well as the specification which color channels should be manipulated. The red color channel is called by entering the digit 1, the blue component by 2 and the green part by 3. The algorithm performs a sequence of image processing procedures as described in section 3 and returns the an RGB image showing the detected fibers only. Note that this is a binary mask based on the subtraction of two color channels only.

```
detectfibers()

% read in RGB image by e.g.
% I=imread('s19a16_resize.tif');
% choose channel1 and channel2 such that:
% 1 corresponds to the red component
% 2 corresponds to the green component
% 3 corresponds to the blue component

function [Fiber]=detectfibers(I,channel1,channel2)
%split image into its color components
Ired=I(:,:,1);
Igreen=I(:,:,2);
Iblue=I(:,:,3);

%remove mixtures of red from blue channel

if channel1==1
    Iin=Ired;
elseif channel1==2
    Iin=Igreen;
elseif channel1==3
    Iin=Iblue;
end
```

```
if channel2==1
    Iout=Ired;
elseif channel2==2
    Iout=Igreen;
elseif channel2==3
    Iout=Iblue;
end

I1=Iin-Iout;
bw=im2bw(I1,graythresh(I1));
I2(:,:,1)=Ired.*uint8(bw);
I2(:,:,2)=Igreen.*uint8(bw);
I2(:,:,3)=Iblue.*uint8(bw);

BW2 = medfilt2(bw);              %remove noise with median filter
BW3 = bwareaopen(BW2,13);        %remove objects smaller than 13 pixels
BW4 = bwmorph(BW3,'skel',Inf);   %find skeleton of mask

branchpoints = bwmorph(BW4,'branchpoints'); %find branchpoints of skeletons
BW6=BW4-branchpoints;            %remove branchpoints
BW5= bwareaopen(BW6,13);         %remove all objects smaller than 13 pixels
endpoints = bwmorph(BW4,'endpoints'); %find endpoints of skeletons
BW7=BW5-endpoints;               %remove endpoints
BW8=bwareaopen(BW7,13);          %remove all objects smaller than 13 pixels

SE1=ones(7);                     %create structuring elements
SE2=ones(3);

%similar to closing, but using two different structuring elements
I2=imdilate(BW8,SE1);            %dilate objects
I3=imerode(I2,SE2);              %erode objects
I4=bwmorph(I3,'skel',Inf);

skel= bwmorph(I4,'skel',Inf);  %find new skeleton
branches = bwmorph(skel, 'branchpoints'); %new branchpoints
ends = bwmorph(skel, 'endpoints'); %new endpoints
[y_ends,x_ends] = find(ends);
branches_locations = find(branches);
```

```
Dmask = false(size(skel));
for k = 1:length(x_ends)
    %Geodesic distance transform of binary image
    D = bwdistgeodesic(skel,x_ends(k),y_ends(k));
    distance2branchpoint = min(D(branches_locations));
    Dmask(D < distance2branchpoint) =true;
end
%remove small branches, only keep main branches
skelD = skel - Dmask;
[y_ends,x_ends] = find(branches); %coordinates of branchpoints

% uncomment for visualization of branchpoints on mask
% figure; imshow(I4);
% hold on;
% plot(x_ends,y_ends,'ro')

CC=bwconncomp(I4);              %find connected components
S = regionprops(CC,'Centroid')  %find centers of components
centroids = cat(1, S.Centroid);

% uncomment for visualization of centroids on mask
% imshow(I4)
% hold on
% plot(centroids(:,1),centroids(:,2), 'b*')
% hold off

%for every component centroid count the number of branchpoints in their
%vicinity
count=zeros(length(centroids(:,1)),1);
for k=1:length(centroids(:,1))
   for n=1:length(x_ends)
       if sqrt((x_ends(n)-centroids(k,1))^2+(y_ends(n)-centroids(k,2))^2)<20
           count(k)=count(k)+1;
       end
   end
end

kill=count>1;           %delete all the object that have more than one
                        %branchpoint close to their center of mass
```

```
% uncomment to visualize the centroids of components to be removed
% figure; imshow(I4)
% hold on
% for indi=1:length(kill)
%     if kill(indi)
%     plot(centroids(indi,1),centroids(indi,2), 'b*')
%     end
% end

I_obj=I4;
L = bwlabel(I4);        % label components

stats2 = regionprops(CC,'Image');
% uncomment to display individual component as an image, e.g. 2nd component
%figure;imshow(stats2(2).Image);

%find pixel coordinates of connected components
stats3 = regionprops(CC,'PixelList');

for l=1:length(stats3)
pixels2(l).coordinates = cat(1, stats3(l).PixelList);
end

%put all components to background which were detected to have too many
%branchpoints
for kkk=1:length(centroids(:,1))
    if kill(kkk)
        [r, c] = find(L==kkk);
        I_obj(r,c)=0;
        clear r
        clear c
    end
end
%%%%%%%%%%%%%%%%%%%%
 Fiber(:,:,1)=Ired.*uint8(I_obj);
 Fiber(:,:,2)=Iblue.*uint8(I_obj);
 Fiber(:,:,3)=Igreen.*uint8(I_obj);
```

A.2 Considering all Color Channels

The following code named `runallcolors.m` calls the routine in A.1 for all possible variations of color channels and adds the binary masks together to get a full image segmentation. The output `FibersCombined` shows all fibers detected on the original image I by adding all binary masks obtained.

```
runallcolors()

clear all
close all

I=imread('ImageName.tif');

% obtain all combinations of channels to subtract from each other
v=[1,2,3];
channels=perms(v);

% initialize array to store masks for each channel combination
allfibers=zeros(double(length(I(:,1,1))),double(length(I(1,:,1))),...
    uint8(length(channels(:,1))));

% apply function detectfibers.m for all channel combinations and store the
% resulting masks in allfibers
for ppp=1:length(channels(:,1))
channel1=channels(ppp,1);
channel2=channels(ppp,2);
str = sprintf('%dminus%d', channel1, channel2);
[Fibers]=detectfibers(I,channel1,channel2);
allfibers(:,:,ppp)=im2bw(Fibers);
end

% newMask will be used to combine all binary masks resulting from the
% different channel combinations
newMask = im2bw(allfibers(:,:,1));   % initialize mask by first binary layer

for ooo=1:length(channels(:,1))
mask2=im2bw(allfibers(:,:,ooo));
```

```
index = (mask2 ~= 0);
newMask(index) = mask2(index);  % add the nonzero values of mask2
end

% Option Start: Uncomment until '%Option end' if skeleton branches
% shall not be removed
% Image Processing Steps to reduce redundant skeleton branches
shrinkit=bwmorph(newMask,'shrink', Inf); % morphological shrinking
K=shrinkit;
K1=newMask-K; %subtract the shrinked objects from original mask

BW1=bwareaopen(K1,60); % remove all object smaller than 60px
BW2=K1-BW1;            % BW2 now carries all branches smaller than 60px
T=newMask-BW2;         % remove these small branches
T1=imfill(T,'holes');  % fill remaining holes
T2=bwmorph(T1,'thin', Inf); % thin filled image


%remove remaining tails which are larger than 5px
Tspur=bwmorph(T2,'spur', 10);
newMask=Tspur;
% Option end

newMask2=bwmorph(newMask,'diag',3);
newMask2=bwmorph(newMask2,'thicken');

%Apply mask to original Image
FibersCombined(:,:,1)=I(:,:,1).*uint8(newMask2);
FibersCombined(:,:,2)=I(:,:,2).*uint8(newMask2);
FibersCombined(:,:,3)=I(:,:,3).*uint8(newMask2);
figure; imshow(FibersCombined)
```

A.3 Color Thresholder App

Matlab's `Color Thresholder App` enables the user to segment an image by manipulating the parameters defining various color spaces. The user can open an RGB image in RGB space or transform it into L*a*b, YCbCr or HSV space.

The user may choose a fiber and search for similar objects throughout a set of images. The steps necessary are as follows[6] :

- Click `Load Image` to load image from files or workspace
- Choose Color Space
- Use `Select Colors` tool in the tool bar to mark a section of the fiber to be searched through all images.
- Click `Find Thresholds`
- Adjust sensitivities of parameters characterizing color space
- Click `Export` → `Export Function`
- Click `New Color Space` to add additional color space and repeat all steps

The masks of the color spaces need to be saved as `createMaskYCbCr(I).m`, `createMaskHSV(I).m` and `createMaskLab(I).m` for the YCbCr, HSV and L*a*b color space respectively to run the code in A.3.

The code generated by the app determines the chosen minima and maxima for each channel of the individual color space and thresholds the image such that all pixel values smaller than the minimum or larger than the maximum are put to zero, resulting in a binary mask of the chosen parameters.

[6]Further instructions can be found at https://de.mathworks.com/help/images/image-segmentation-using-the-color-thesholder-app.html, accessed on 15-01-2017

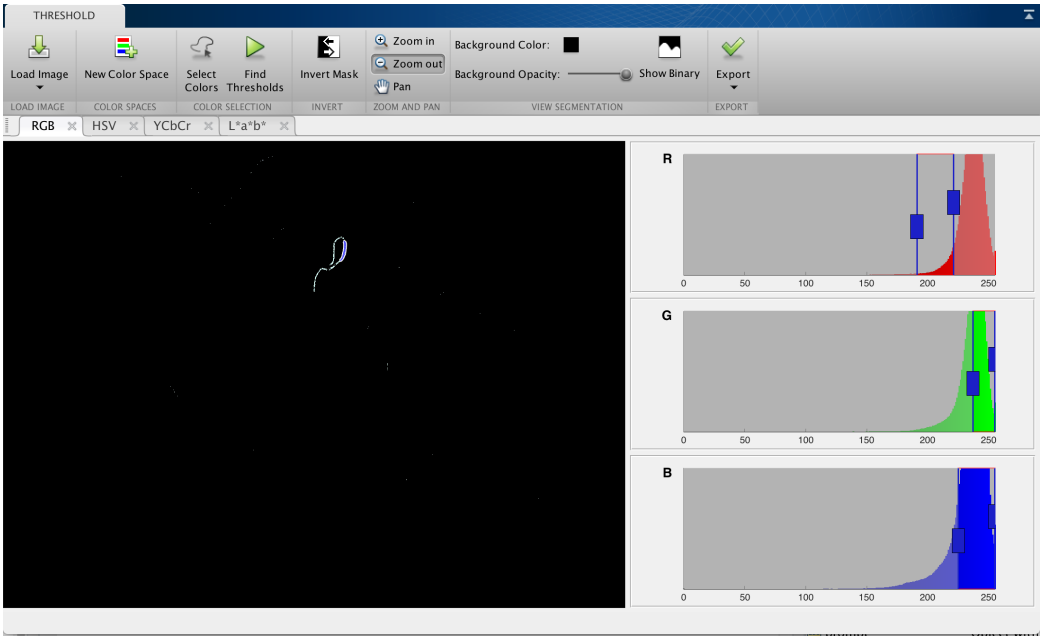

(a) RGB Space

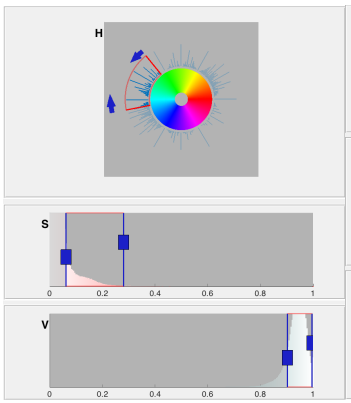

(b) HSV Space

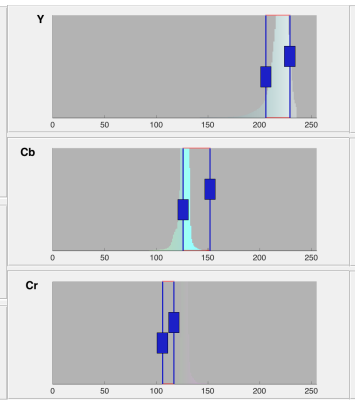

(c) YCbCr Space

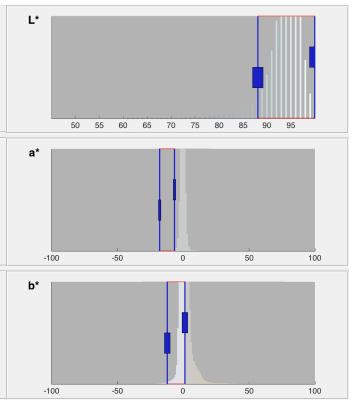

(d) L*a*b Space

Figure 38: Color Thresholder App and the tunable parameters in the various color spaces

Using the app is a convenient way to determine the parameters. However the files `createMaskYCbCr(I).m`, `createMaskHSV(I).m` and `createMaskLab(I).m` which are needed in `ApplyColorMask.m` (appendix A.3) to find fibers of a specific color in a set of images, can be created manually as follows. The code reads in an RGB image and returns a binary mask as well as the masked RGB image:

```
function [BW,maskedRGBImage] = createMaskYCbCr(RGB)
% Auto-generated by colorThresholder app on 02-Jan-2017

% Convert RGB image to chosen color space
I = rgb2ycbcr(RGB);

% Define thresholds for channel 1 based on histogram settings
channel1Min = 205.000;
channel1Max = 238.000;

% Define thresholds for channel 2 based on histogram settings
channel2Min = 127.000;
channel2Max = 132.000;

% Define thresholds for channel 3 based on histogram settings
channel3Min = 100.000;
channel3Max = 121.000;
% Create mask based on chosen histogram thresholds
BW = (I(:,:,1) >= channel1Min ) & (I(:,:,1) <= channel1Max) & ...
    (I(:,:,2) >= channel2Min ) & (I(:,:,2) <= channel2Max) & ...
    (I(:,:,3) >= channel3Min ) & (I(:,:,3) <= channel3Max);

% Initialize output masked image based on input image.
maskedRGBImage = RGB;

% Set background pixels where BW is false to zero.
maskedRGBImage(repmat(~BW,[1 1 3])) = 0;
```

`createMaskHSV(I).m` and `createMaskLab(I).m` are created accordingly, but transforming the image which is originally given in RGB space differs from the code given above. The transformation from RGB to HSV is done by `I = rgb2hsv(RGB)` while the transformation from RGB to L*a*b space is done by

```
RGB = im2double(RGB);
cform = makecform('srgb2lab', 'AdaptedWhitePoint', whitepoint('D65'));
I = applycform(RGB,cform);
```

The following code of the routine `ApplyColorMask.m` combines the binary masks returned by `createMaskYCbCr(I).m`, `createMaskHSV(I).m` and `createMaskLab(I).m` for RGB image I. In case it detects objects larger than 100px present in all binary masks resulting from the three examined color spaces

```
% ApplyColorMask.m: combines masks created in Color Thresholder App for all
% Color spaces which are stored in the following functions:
% createMaskycbcr(I).m, createMaskhsv(I).m, createMaskLab(I);
ApplyColorMask()

close all;
clear all;

num_img=77;     % choose number of images to browse for chosen fiber color
for n=1:num_img
    s1= 's19a';
    s2=num2str(n,'%02i');
    s3= '_resize.tif';
    s = strcat(s1,s2,s3);
    I=imread(s);

    % Call mask functions obtained by Color Thresholder app
    [BWYCbCr,maskedRGBImageYCbCr] = createMaskYCbCr(I);
    [BWHSV,maskedRGBImageHSV] = createMaskHSV(I);
    [BWLab,maskedRGBImageLab] = createMaskLab(I);

    % Morphological Image Processing Steps to Enhance Image Segmentation
    mask=BWYCbCr+BWHSV+BWLab;
    mask2=imdilate(mask, ones(7));
    mask3=imerode(mask2, ones(3));
    mask4=bwareaopen(mask3, 60);
    mask5=bwmorph(mask4, 'Thin', Inf);
    mask6=bwareaopen(mask5, 50);
    mask7=imclose(mask6, ones(5));

    % calculate areas of objects in binary image
    stats=regionprops(mask7);
```

```
    areas = cat(1, stats.Area);

    % Inform user if objects larger than 100px are found
    if any(areas>100)
        prompt = 'Object with similar features detected in image';
        outputstr = strcat(prompt,s);
        figure; imshowpair(I,mask7, 'montage')
    end
end
```

B Spectral Results

B.1 Experiments at 532nm

The following results are obtained by experiments conducted at a laser excitation wavelength of 532nm. 20 measurements were taken at a total of eight different fibers. Table 6 shows a list of all experiments, the chosen parameters, fiber IDs used in the subsequent part of this section and the presence or absence of any kind of destructive effect of the Raman examination. *LW* stands for laser wavelength, LP for laser power and IT for integration time. To interpret the obtained spectra literature has been consulted to find consistency with other Raman spectra of textile fibers: [1], [3], [34], [35], [36], [37], [38], [39], [4].

Table 6: Table of Results

Color	ID	Location	LW [nm]	LP [mW]	IT [s]	Damage on fiber
blue	B1	1	532	10	0.044	bleaching
blue	B1	2	532	10	0.037	bleaching
green	G1	1	532	10	0.037	no
ocher	O1	1	532	45	0.084	no
ocher	O1	2	532	45	0.044	destructed
ocher	O2	1	532	45	0.044	no
ocher	O2	2	532	45	0.044	destructed
ocher	O2	3	532	10	0.044	no
red	R1	1	532	10	0.037	no
black	S1	1	532	45	0.044	destructed
black	S1	2	532	45	0.035	destructed
black	S1	3	532	10	0.035	no
black	S1	4	532	10	0.044	no
white	W1	1	532	45	0.1337	no
white	W1	1	532	45	0.0437	no
white	W1	1	532	45	0.084	no
white	W2	1	532	40	0.0371	no
white	W2	1	532	40	0.0371	no
white	W2	1	532	40	0.0437	destructed
white	W2	2	532	40	0.1337	no

B.1.1 Sample B1

Sample B1 is a blue fiber which was measured on two locations. In both measurements bleaching of the fiber occurred. Figure 39 shows the bleaching effect on the fiber for a signal acquisition at a laser power of 10mW for an integration time of 0.044 seconds.
The average spectrum for the fiber is shown in figure 41 for the original spectrum as well as the baseline corrected one.

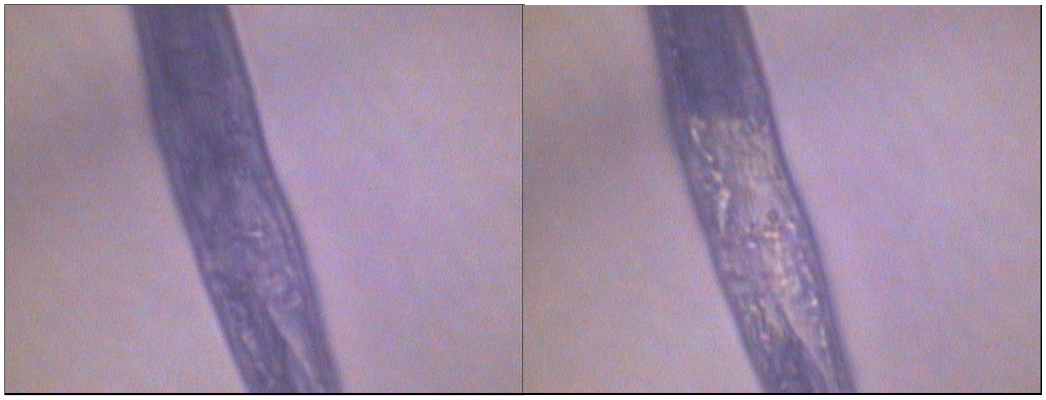

(a) Before Measurement (b) After Measurement

Figure 39: Bleaching occurs on blue fiber B1 after measurement [532nm, 10mW for 0.044s, location 1]

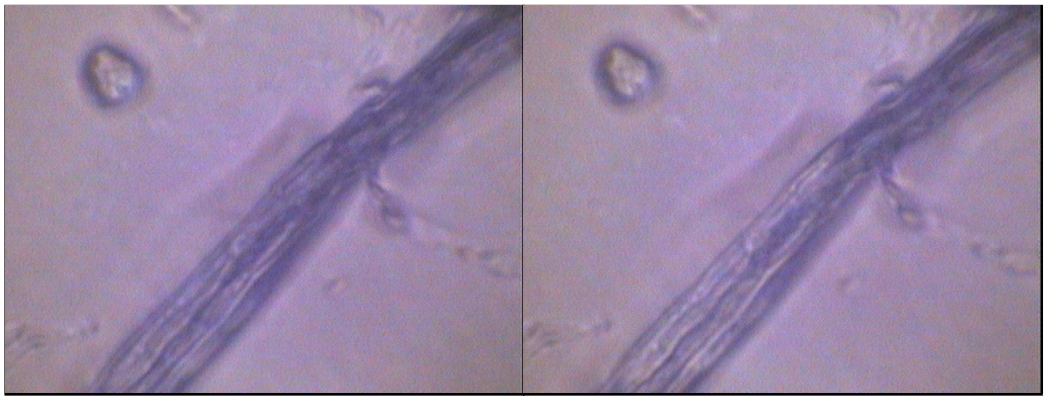

(a) Before Measurement (b) After Measurement

Figure 40: Bleaching occurs on blue fiber B1 after measurement [532nm, 10mW for 0.037s, location 2]

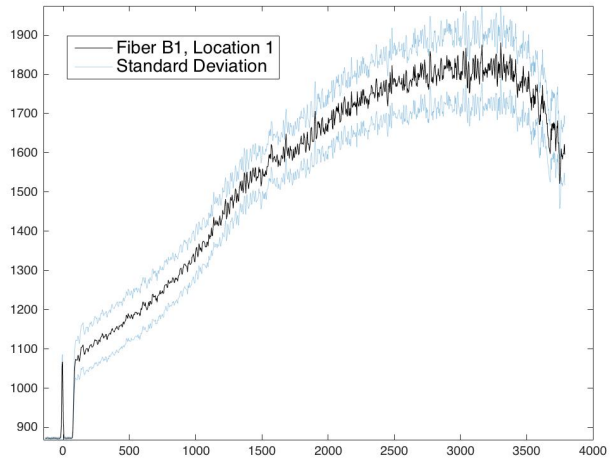

(a) Average raw data spectrum of sample B1.

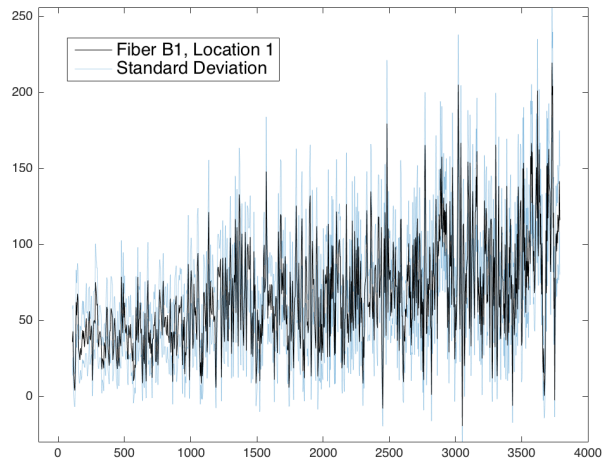

(b) Baseline corrected spectrum of sample B1 averaged and trimmed

Figure 41: Spectrum of B1 at location 1 obtained at a laser power of 10mW and 0.044s integration time.

The second measurement was taken at 10mW for 0.037 seconds and shows bleaching as well, visible in figure 40. The averaged original as well as the baseline corrected spectrum of this sample section is demonstrated in 42.

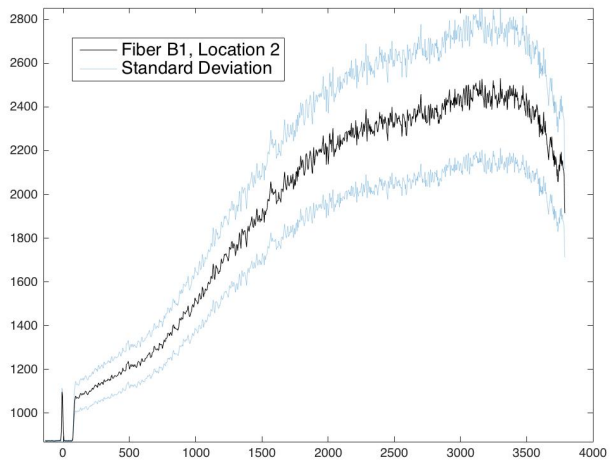

(a) Average raw data spectrum of sample B1.

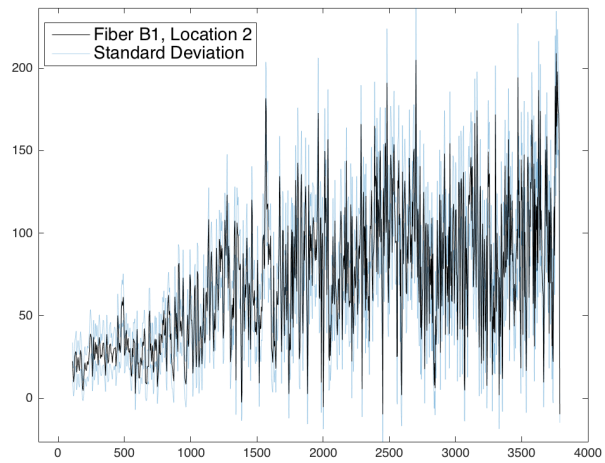

(b) Baseline corrected spectrum of sample B1 averaged and trimmed

Figure 42: Spectrum of B1 at location 2 obtained at 10mW and 0.037s.

B.1.2 Sample G1

Sample G1 originates from a green fiber. It was measured with a laser power of 10mW for 0.037 seconds. Although the fiber was not destroyed or bleached during the experiment, it was not possible to find a corresponding reference spectrum due to the prevailing fluorescence.

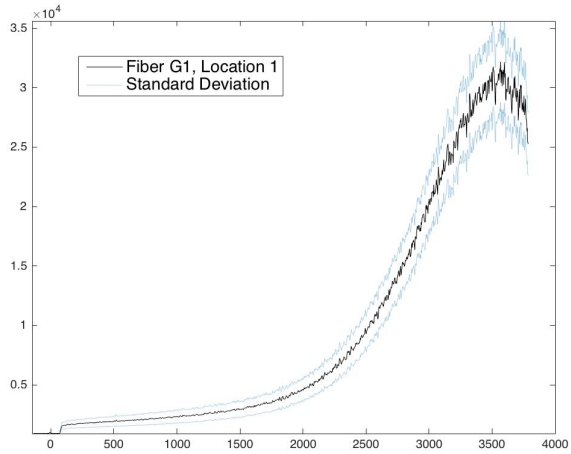

(a) Average raw data spectrum of sample G1.

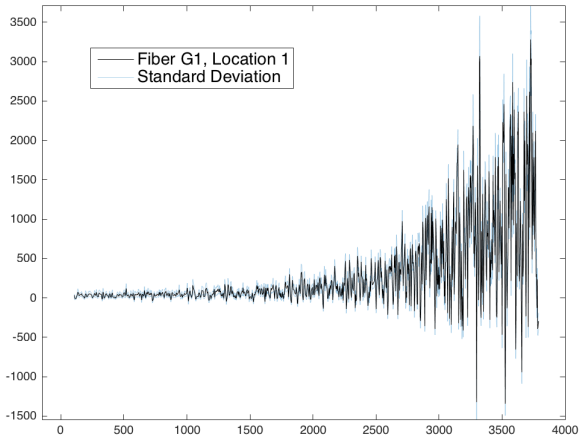

(b) Baseline corrected spectrum of sample G1 averaged and trimmed.

Figure 43: Spectrum of G1 at location 1 obtained at 10mW and 0.037s.

B.1.3 Sample O1

Sample O1 originates from an ocher colored fiber abundantly present in the adhesive tapes. It was measured at two locations, both at 45mW. For the first location the integration time was 0.084 seconds and no destruction occurred. The resulting raw data spectra as well as the baseline corrected and trimmed spectra are shown in figure 44.

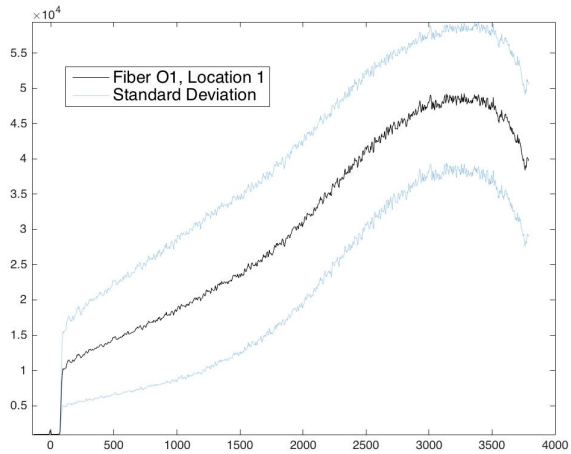

(a) Average raw data spectrum of sample O1.

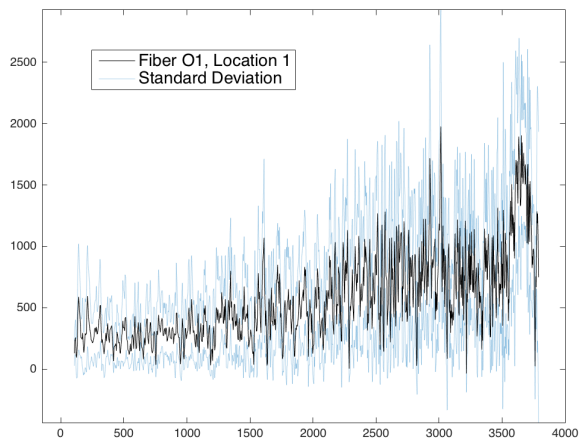

(b) Baseline corrected spectrum of sample B1 averaged and trimmed.

Figure 44: Spectrum of O1 at location 1 obtained at 45mW, 0.084s

For the second location the signal was collected for 0.044 seconds and although the integration time was shorter than at the first location, destruction occurred, as shown in figure 46. Despite the destructive results on the fiber, the spectrum of this sample in figure 45 shows less noise than O1 at the first location.

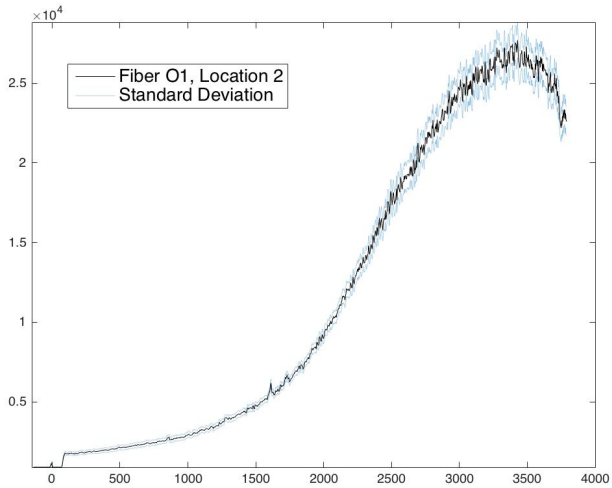

(a) Average raw data spectrum of sample O1.

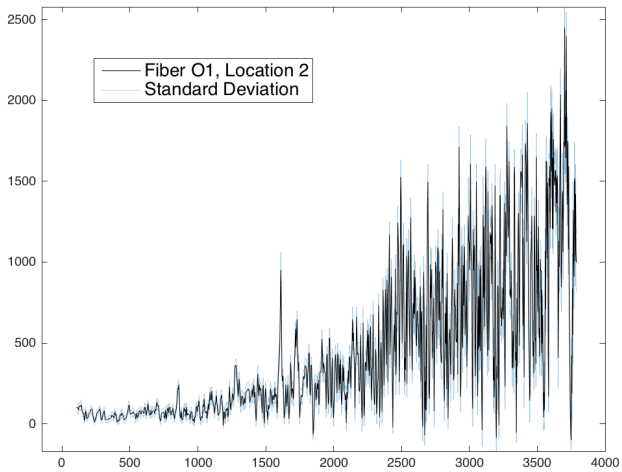

(b) Baseline corrected spectrum of sample O1 averaged and trimmed.

Figure 45: Spectrum of O1, location 2 obtained at 45mW and 0.044s.

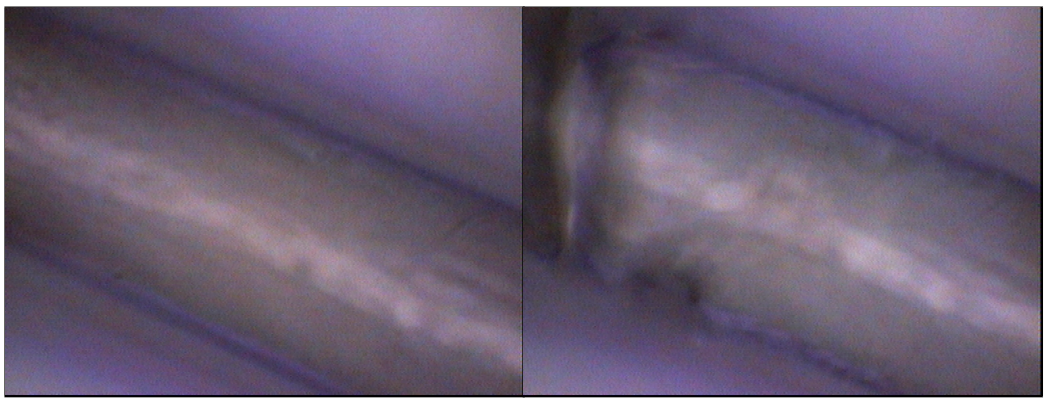

(a) Before Measurement (b) After Measurement

Figure 46: Destruction occurs on ocher fiber O1 after measurement [532nm, 45mW for 0.044s, location 2]

B.1.4 Sample O2

By examination through an optical microscope samples O1 and O2 appeared to be fibers from the same origin. Fiber O2 was scanned at three different locations. The first two experiments were conducted for 45mW, the last one at location 3 was done for 10mW. The integration time was 0.044 seconds for all three locations.

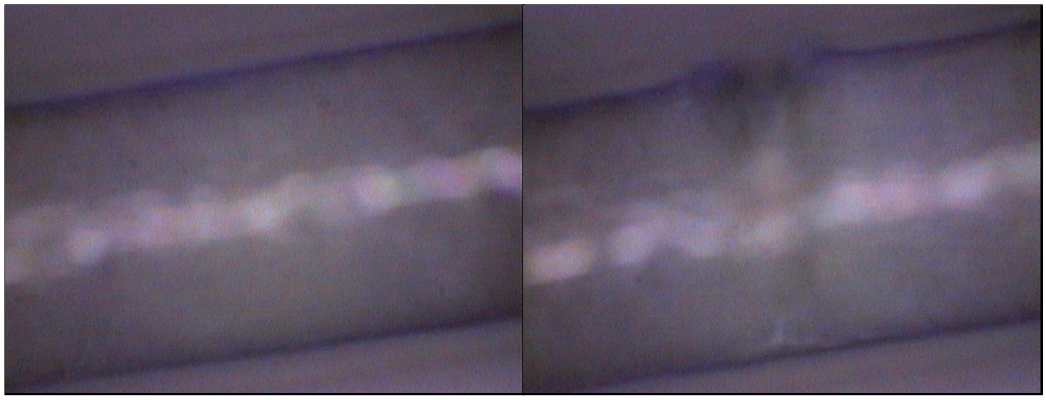

(a) Before Measurement (b) After Measurement

Figure 47: Destruction occurs on ocher fiber O2 after measurement [532nm, 45mW for 0.044s, location 2]

The spectrum of sample O2 at the first location is shown in figure 48.

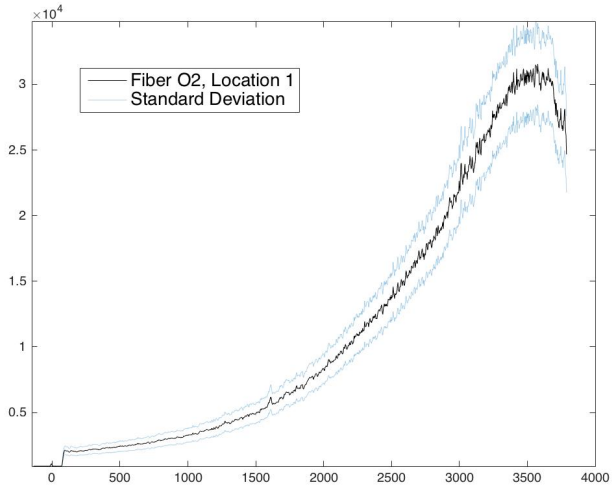

(a) Average raw data spectrum of sample O2.

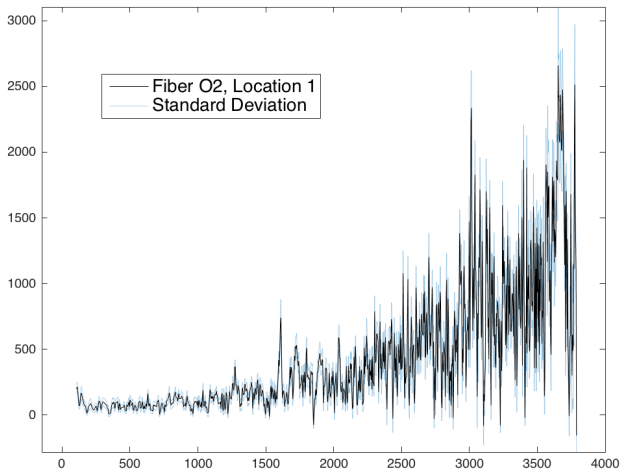

(b) Baseline corrected spectrum of sample O2 averaged and trimmed.

Figure 48: Spectrum of O2 at location 1 obtained at 45mW and 0.044s.

Fiber O2 did not show any signs of destruction at location 1, but did so at location 2, although the very same parameters for handling the Raman microscope were used. The effect is shown in figure 47. Its Raman spectrum

is depicted in figure 49 as raw data as well as baseline corrected and trimmed data.

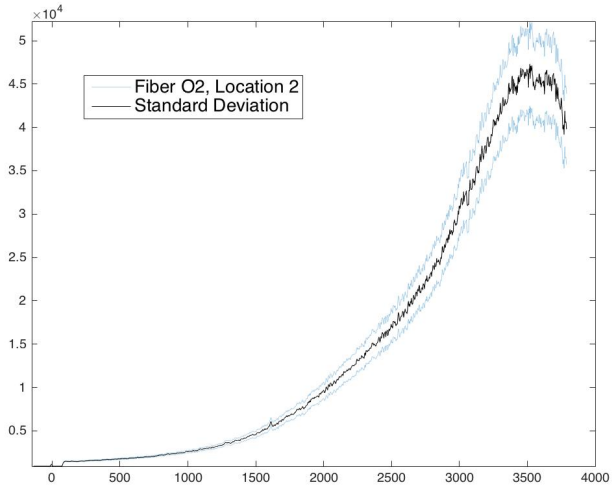

(a) Average raw data spectrum of sample O2.

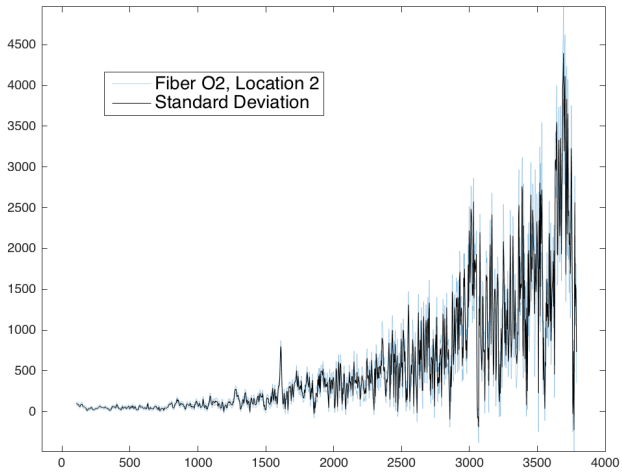

(b) Baseline corrected spectrum of sample O2 averaged and trimmed.

Figure 49: Spectrum of O2 at location 2 obtained at 10mW and 0.044s.

The same fiber was measured at a third location. The resulting spectra of the raw and preprocessed data are shown in figure 50.

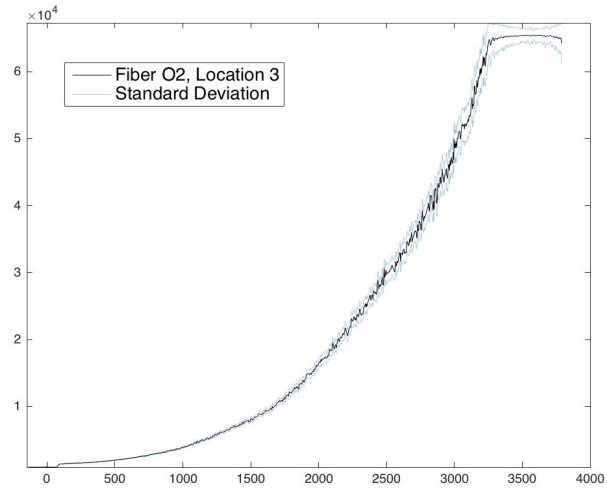

(a) Average raw data spectrum of sample O2.

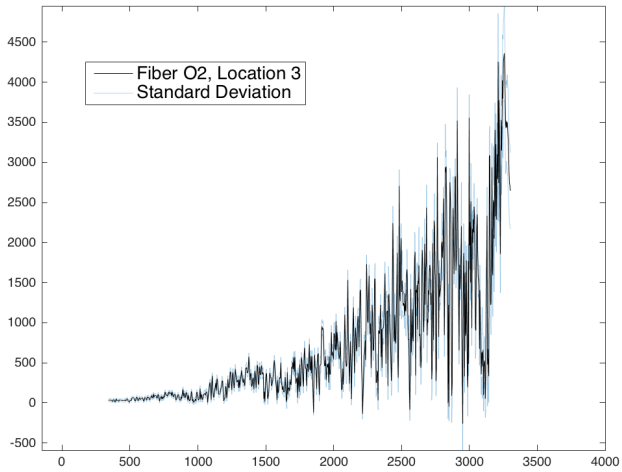

(b) Baseline corrected spectrum of sample O2 averaged and trimmed.

Figure 50: Spectrum of O2 at location 3 obtained at 10mW and 0.044s.

B.1.5 Sample R1

The red fiber sample R1 was examined at one location at 10mW for an integration time of 0.037 seconds. No destruction occurred, but the fiber shows a large standard deviation in the average spectrum, see figure 51, which leads to the conclusion that the measurements are very noisy due to the high fluorescence.

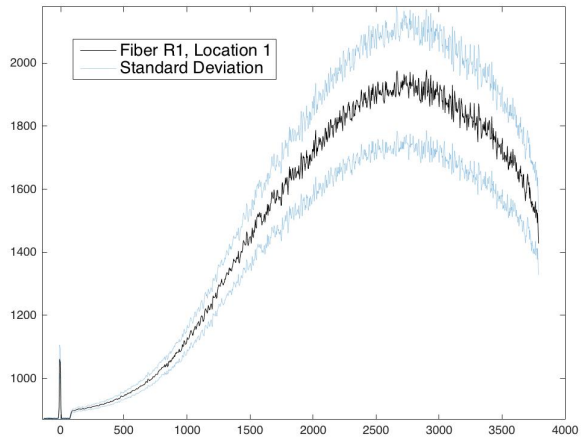

(a) Average raw data spectrum of sample R1.

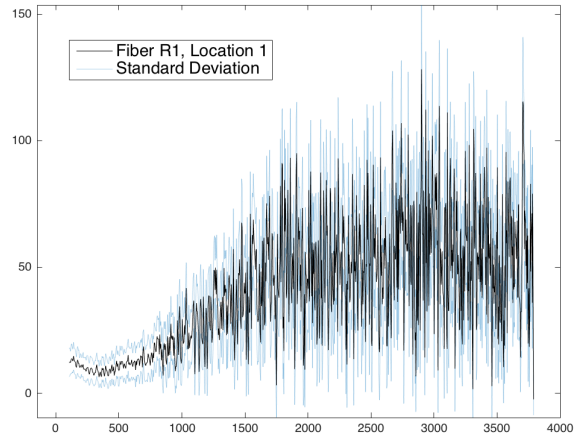

(b) Baseline corrected spectrum of sample R1 averaged and trimmed.

Figure 51: Spectrum of R1 at location 1 obtained at 10mW and 0.037s.

B.1.6 Sample S1

In total four measurements were taken from sample S1, a black fiber.
The first two were conducted with 45mW for 0.044s and 0.035s respectively. They were damaged very badly, as can be seen in figures 52 and 53. These destructions must have occurred so early during the measurements, that no reasonable spectrum was possible to be obtained at all.

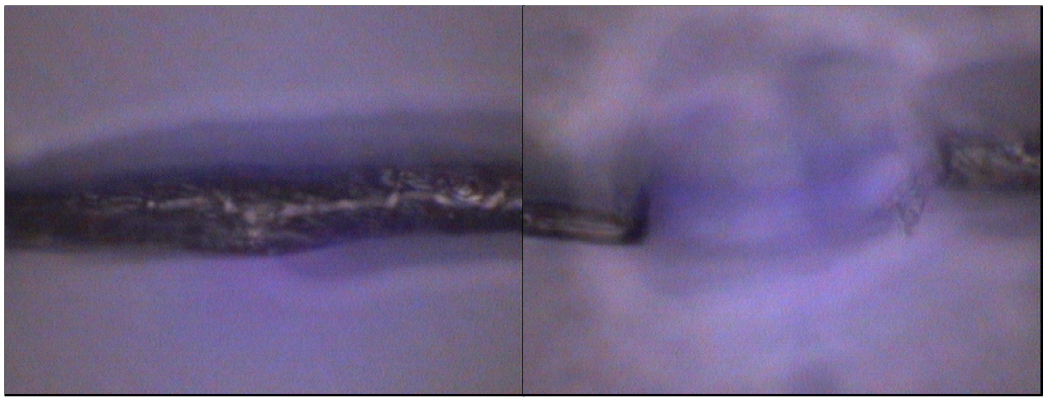

(a) Before Measurement (b) After Measurement

Figure 52: Destruction occurs on black fiber S1 after measurement [532nm, 45mW for 0.044s, location 1]

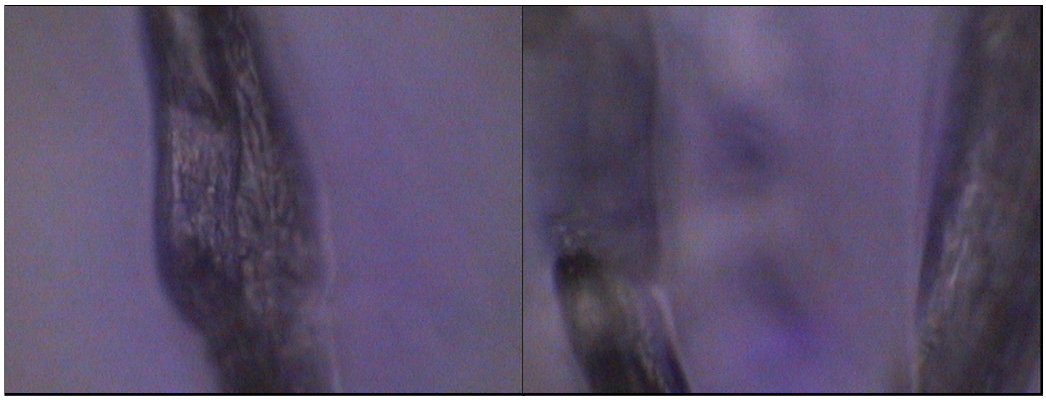

(a) Before Measurement (b) After Measurement

Figure 53: Destruction occurs on black fiber S1 after measurement [532nm, 45mW for 0.035s, location 2]

For locations 3 and 4 the laser power has been reduced from 45mW to 10mW.

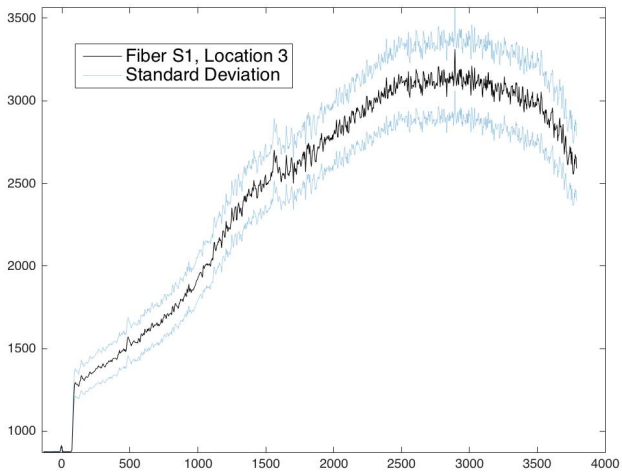

(a) Average raw data spectrum of sample S1.

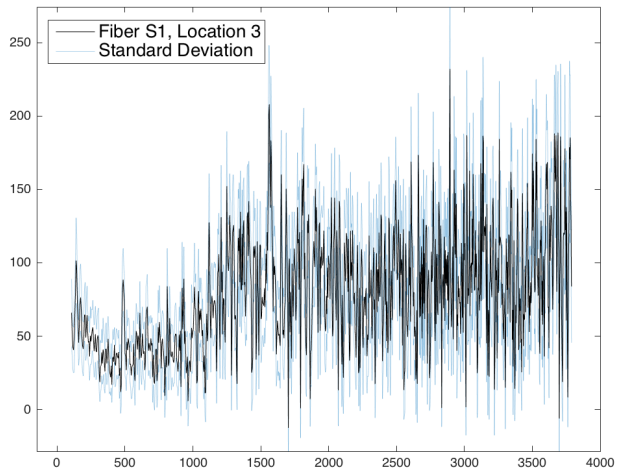

(b) Baseline corrected spectrum of sample S1 averaged and trimmed.

Figure 54: Spectrum for S1 at location 3 obtained at 10mW and 0.035s.

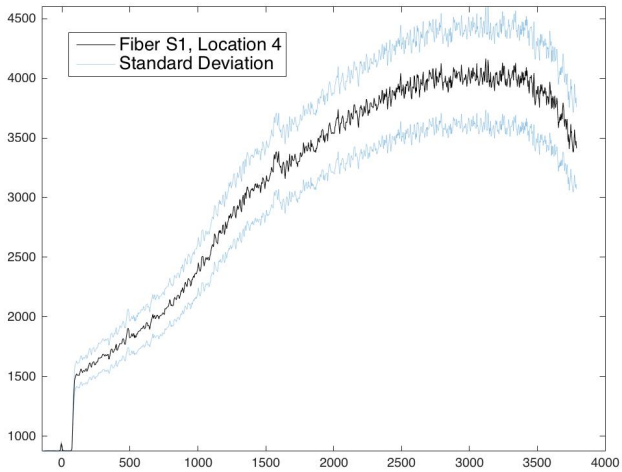

(a) Average raw data spectrum of sample S1.

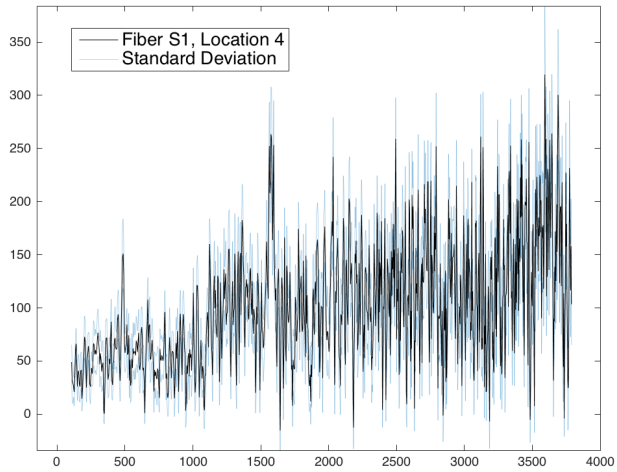

(b) Baseline corrected spectrum of sample S1 averaged and trimmed.

Figure 55: Spectrum for S1 at location 4 obtained at 10mW and 0.035s.

B.1.7 Sample W1

Sample W1 belongs to a white fiber, figure 56, and is a perfect example that it is generally possible to obtain characteristic Raman spectra of a fiber if fluorescence due to the dye of the fiber would not pose a problem in all other samples examined so far. Figure 57 shows the spectrum for an integration time of 0.1337 seconds which is one order higher than in all the other experiments. Yet, no destruction occurs and the spectrum is a lot clearer due to the prolonged integration time. For comparison figures 58 and 59 show the spectra of the same fiber at the same location but for different integration times: 0.084 and 0.0437 seconds. The characteristic peaks are still clearly visible, but the variance among the sampling points which have been averaged is higher, marked by the light green band around the blue or black average signal.

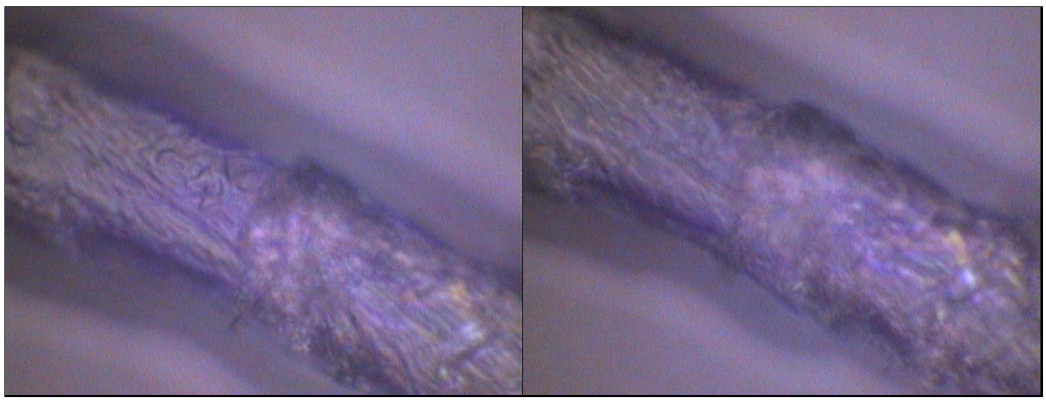

(a) Before Measurement (b) After Measurement

Figure 56: No destruction occurs on white fiber W1 after measurement [532nm, 45mW for 0.1337s, location 1]

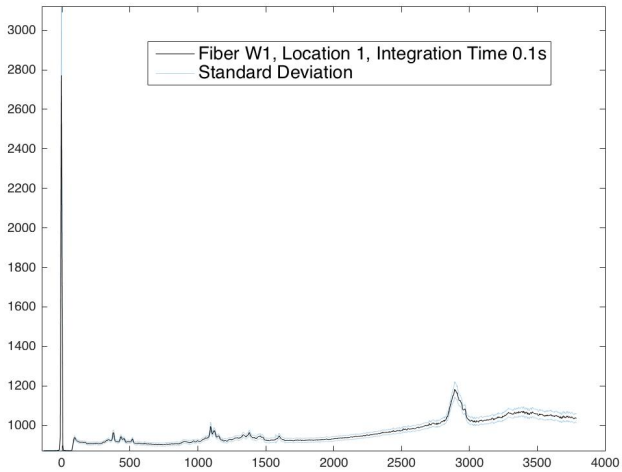

(a) Average raw data spectrum of sample W1.

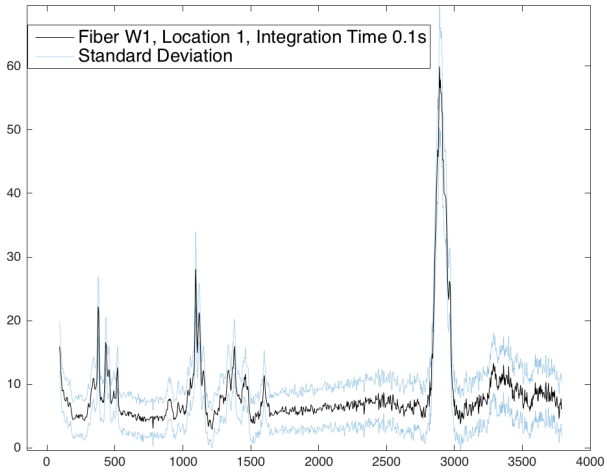

(b) Baseline corrected spectrum of sample W1 averaged and trimmed.

Figure 57: Spectrum of W1 at location 1 obtained at 45mW and 0.1337s.

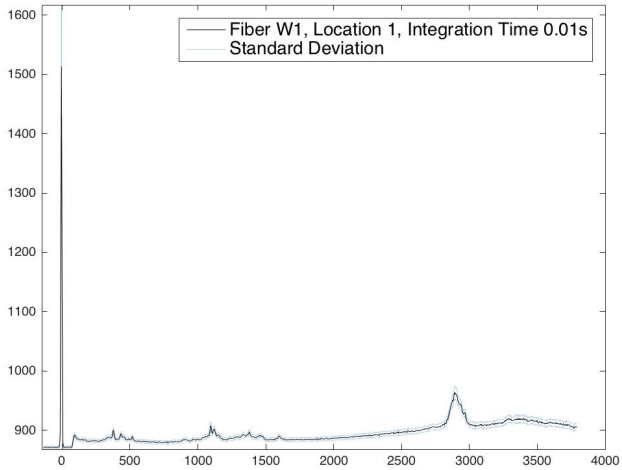

(a) Average raw data spectrum of sample W1.

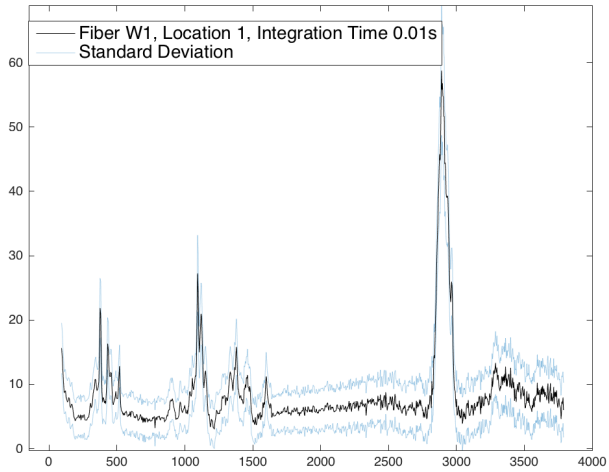

(b) Baseline corrected spectrum of sample W1 averaged and trimmed.

Figure 58: Spectrum for W1 at location 1 obtained at 45mW and 0.084s.

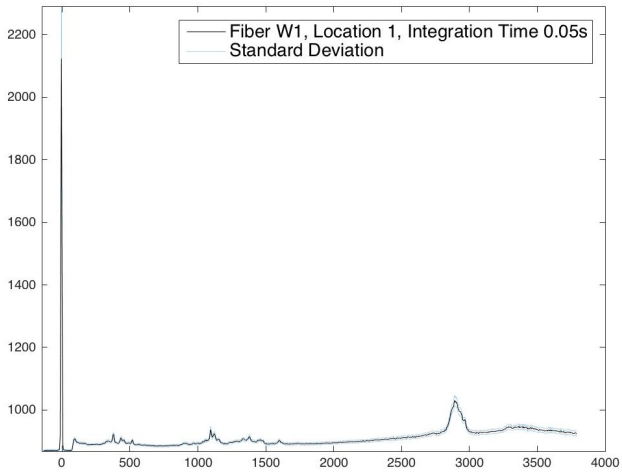

(a) Average raw data spectrum of sample W1.

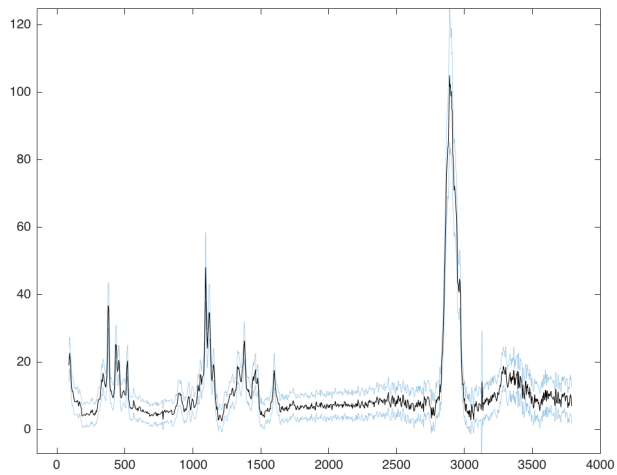

(b) Baseline corrected spectrum of sample W1 averaged and trimmed.

Figure 59: Spectrum for W1 at location 1 obtained at 45mW and 0.0437s.

B.1.8 Sample W2

Another white fiber was investigated at two different locations. At the first location the sample was measured three times in a row each time for 40mW, two times for 0.0371 seconds and once for 0.0437 seconds. Laser cutting occurred after the forth measurement and the sample was destructed as depicted in figure 60. The same fiber measured at a different location gives the signal seen in 61. The spectra obtained during these measurements have not been as clear as the ones acquired by the white fiber W1. It shows some fluorescence even though less than most of the colored fibers inspected so far. It is possible that this occurrence is the result of a previous chemical treatment of the fiber, such as bleaching or the use of a special laundry detergent. The spectrum shows similar peaks as the one obtained by sample W1, but in poorer quality due to the fact that the Raman signal is hidden in the signal caused by the fluorescence.

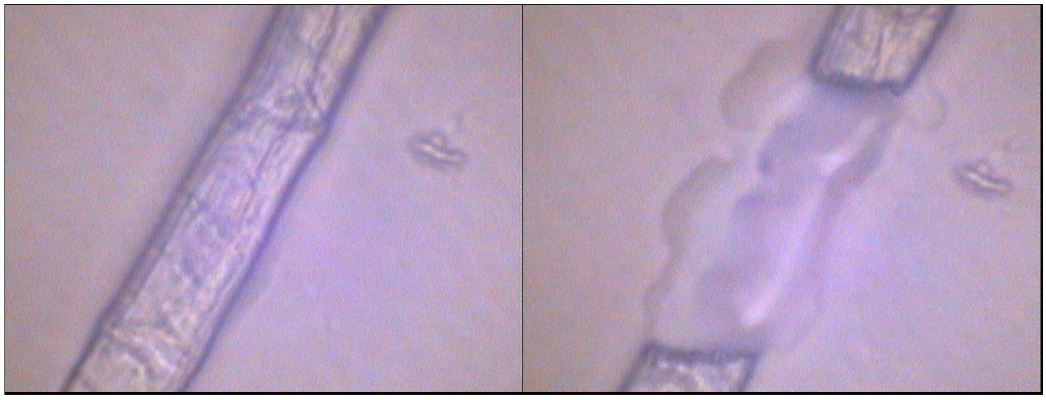

(a) Before Measurement (b) After Measurement

Figure 60: Destruction occurs on white fiber W2 after measurement [532nm, 40mW for 0.0371s, location 1]

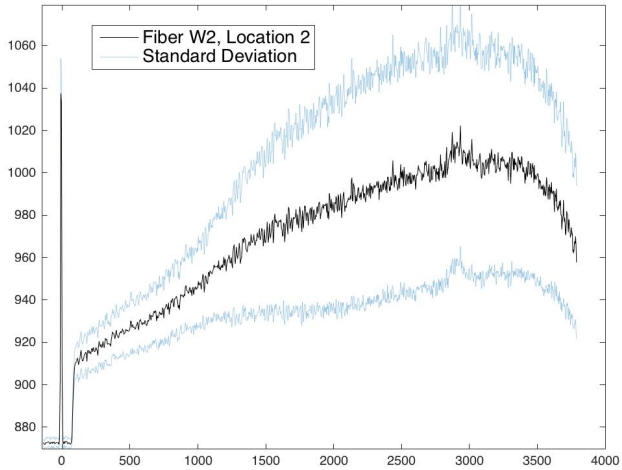

(a) Average raw data spectrum of sample W2.

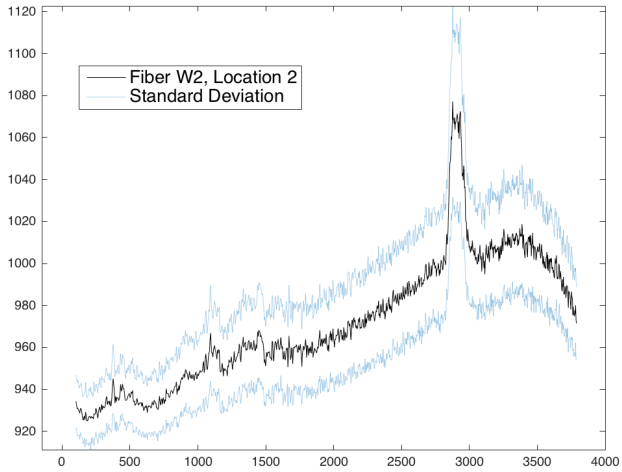

(b) Baseline corrected spectrum of sample W2 averaged and trimmed.

Figure 61: Spectrum for W2 at location 2 obtained at 40mW and 0.0371s.

List of Figures

1 Evidence Acquisition 6
2 Different Fiber Densities in Sample 7
3 Fiber Selection 8
4 RGB Color Space 15
5 HSV Color Space 17
6 La*b* Color Space 18
7 RGB and Grayscale 20
8 Histograms of Intensity Image 22
9 Effect of Structuring Elements 24
10 Thresholding by Otsu 27
12 Edge Detectors 33
13 Effects of Lossy Image Compression 35
14 RGB Color Channels 36
15 First Image Processing Steps 37
16 Second Image Processing Steps 39
17 Third Image Processing Steps 40
18 Removing Artifacts 41
19 Example of Fiber Skeleton 41
20 Skeleton Projection onto Original Image 42
21 Combination of Binary Masks 43
22 Automatic Detection of Green Fibers I 45
23 Automatic Detection of Green Fibers II 46
24 Dark Background Image Acquisition 47
25 Multiple Optical Microscope Sources 48
26 Raman Setup 50
27 Resonance Raman Spectroscopy and Fluorescence 60
28 Curse of Dimensionality 64
29 Principle of Random Forests 66
38 Color Thresholder App 87
39 Bleaching on Blue Fiber, Sample B1, Location 1 92
40 Bleaching on Blue Fiber, Sample B1, Location 2 92

41 Spectrum of Sample B1, Location 1 93
42 Spectrum of Sample B1, Location 2 94
43 Spectrum of Sample G1, Location 1 95
44 Spectrum of Sample O1, Location 1 96
45 Spectrum of Sample O1, Location 2 97
46 Destruction of Sample O1, Location 2 98
47 Destruction of Sample O2, Location 2 98
48 Spectrum of Sample O2, Location 1 99
49 Spectrum of Sample O2, Location 2 100
50 Spectrum of Sample O2, Location 3 101
51 Spectrum of Sample R1, Location 1 102
52 Destruction of Sample S1, Location 1 103
53 Destruction of Sample S1, Location 2 103
54 Spectrum of Sample S1, Location 3 104
55 Spectrum of Sample S1, Location 4 105
56 No Destruction of Sample W1, Location 1 106
57 Spectrum of Sample W1, Location 1 107
58 Spectrum of Sample W1, Location 1 108
59 Spectrum of Sample W1, Location 1 109
60 Destruction of Sample W2, Location 1 110
61 Spectrum of Sample W2, Location 2 111

List of Tables

1 Murder Attempt Rates in Austria 5
2 Fibers as Constructive Means of Evidence 5
3 Color Space Parameters for Fiber Detection 44
4 Relationship between Objective, Magnification and Numerical Aperture 53
5 Relationship between Wavelength and Pinhole Size 53
6 Table of Spectral Results 91

References

[1] Li-Ling Cho. Identification of textile fiber by raman microspectroscopy. *Forensic Science International*, 6:55–62, 2007.

[2] Jason Miller and Edward Bartick. Forensic analysis of single fibers by raman spectroscopy. *Applied Spectroscopy*, 55:1729–1732, 2001.

[3] L. Lepot, K. De Wael, F. Gason, and B. Gilbert. Application of raman spectroscopy to forensic fibre cases. *Applied Spectroscopy*, 48:109–117, 2008.

[4] Fran Adar. Raman microscopy analysis of molecular orientation in organic fibers. *Spectroscopy*, 28(2), 2013.

[5] Colin Aitken and Franco Taroni. *Statistics and the Evaluation of Evidence for Forensic Scientists*. John Wiley and Sons, Ltd, 2 edition, 2004.

[6] G. Schnegelsberg. *Handbuch der Faser: Theorie und Systematik der Faser*. Theorien und Systeme in Technik und Ökonomie. Dt. Fachverl., 1999.

[7] Douglas W. Deedrick. Hairs, fibers, crime, and evidence part 2: Fiber evidence. *Forensic Science Communications*, 2(3), 2000. Accessed: 2017-01-17.

[8] ASTM E2224 - 10 standard guide for forensic analysis of fibers by infrared spectroscopy. `http://www.astm.org/cgi-bin/resolver.cgi?E2224`. Accessed: 2016-12-22.

[9] Gonzalez R. and Woods. R. *Digital Image Processing*. Prentice Hall, 3 edition, 2007.

[10] Paul Geladi Hans Grahn. *Techniques and Applications of Hyperspectral Image Analysis*. J. Wiley, 2007.

[11] A.Goetz and B. Curtiss. Hyperspectral imaging of the earth: Remote analytical chemistry in an uncontrolled environment. *Field Analytical Chemistry and Technology*, 1(2):67–76, 1996.

[12] Chein-I Chang. *Hyperspectral Imaging: Techniques for Spectral Detection and Classification.* Springer, 1 edition, 2003.

[13] Mark D. Fairchild. *ColorAppearance Models.* Series in Imaging Science and Technology. Wiley-IS & T, 3 edition, 2013.

[14] Scott E Umbaugh. *Digital Image Processing and Analysis : Human and Computer Vision Applications with CVIPtools, Second Edition.* CRC Press, 2nd ed edition, 2010.

[15] *Image Processing Toolbox: User's Guide.*

[16] J. E. Agudo, P. J. Pardo, H. Sánchez, A. L. Pérez, and M. I. Suero. A low-cost real color picker based on arduino. *Sensors*, 14:11943–11956, 2014.

[17] Wenzhu Yang, Daoliang Li, Liang Zhu, Yuguo Kang, and Futang Li. A new approach for image processing in foreign fiber detection. *Computer and Electronics Agriculture*, 68:68–77, 2009.

[18] P.K. Sahoo, S. Soltani, and A.K.C. Wong. A survey of thresholding techniques. *Computer Vision, Graphics, and Image Processing*, 41:233–260, 1988.

[19] Otsu N. A threshold selection method from gray-level histograms. *IEEE Transactions on Systems, Man, and Cybernetics*, 9(1):62–66, 1979.

[20] R. A. Salinas, C. Richardson, M. A. Abidi, and R. C. Gonzalez. Data fusion: Color edge detection and surface reconstruction through regularization. *IEEE Trans. Indus. Elec.*, 43(3):355–363, 1996.

[21] J. Canny. A computational approach to edge detection. *IEEE Transactioans on Pattern Analysis and Machine Intelligence*, 8(6), 1986.

[22] Lim J. S. *Two-Dimensional Signal and Image Processing.* Prentice Hall, 1989.

[23] Parker J. *Algorithms for Image Processing and Computer Vision.* John Wiley and Sons, Inc., 2 edition, 2011.

[24] T. Dieing, O. Hollricher, and J. Toporski. *Confocal Raman Microscopy.* Springer Series in Optical Sciences, 2010.

[25] S. Yang and O. Akkus. Fluorescence background problem in raman spectroscopy: Is 1064 nm excitation an improvement of 785 nm? Technical report, Case Western Reserve University, 2013. Wasatch Photonics: Report.

[26] H. Lohninger and J. Ofner. Multisensor hyperspectral imaging as a versatile tool for image-based chemical structure determination. *Spectroscopy Europe*, 26(5):6–10, 2014.

[27] P. Eilers and H. Boelens. Baseline correction with asymmetric least squares smoothing. Technical report, Leiden University Medical Center, 2005.

[28] G. Schulze, A. Jirasek, M. Yu, A. Lim, R. Turner, and M. Blades. Investigation of selected baseline removal techniques as candidates for automated implementation. *Applied Spectroscopy*, 59:545–574, 2005.

[29] P. Eilers. A perfect smoother. *Analytical Chemistry*, 75:3631–3636, 2003.

[30] Friedman J., Hastie T., and Tibshirani R. *The Elements of Statistical Learning.* Springer Series in Statistics, 2009.

[31] A. Liaw and M. Wiener. Classification and regression by randomforest. *R News*, 2:18–22, 2002.

[32] Tin Kam Ho. Random decision forest, 1995.

[33] G. Machado, M.R. Mendoza, and L.G. Corbellini. What variables are important in predicting bovine viral diarrhea virus? a random forest approach. *Veterinary Research*, 46(1), 2015.

[34] P. Hendra, W. Maddams, I. Royaud, H. Willis, and V. Zichy. The application of fourier transform raman spectroscopy to the identification and characterization of polyamides - i. single number nylons. *Spectrochimica Acta*, 46A(5):747–756, 1990.

[35] Sharma Neha, Tripathi B., Shrivastava A., and Chauhan R. Laser raman studies of fibrous polymer - a review. *International Journal of Engineering and Management Sciences*, 5(2):128–139, 2014.

[36] G. Jochem. On the potential of raman microscopy for the foresnic analysis of coloured textile fibres. *Science & Justice*, 42(4):215–221, 2002.

[37] Alberto Milani. Unpolarized and polarized raman spectroscopy of nylon-6 polymorphs: A quantum chemical approach. *The Journal of Physical Chemistry*, 119:3868–3874, 2015.

[38] B. Schrader, H. Schulz, G. Andreev, H. Klump, and J. Sawatzki. Non-destructive nir-ft-raman spectroscopy of plant and animal tissues, of food and works of art. *Talanta*, 53:35–45, 2000.

[39] A. Pud, K. Fatyeyeva, J. Bardeau, S. Rogalsky, M. Tabellout, and G. Shapoval. Polyamide-12/polyaniline layered composite films: Specificity of the formation and raman spectroscopy investigation. *Journal of Macromolecular Science, Part A*, 44(2):183–192, 2007.